LA-UR -82-3446

Conf-821049--7

Los Alamos National Laboratory is operated By the University of California for the United States Department of Energy under contract W-7405-ENG-36

LA-UR--82-3446

DE83 003544

TITLE: STRAIN HARDENING OF HEAVILY COLD-WORKED METALS

AUTHOR(S) S. S. Hecker
M. G. Stout

SUBMITTED TO Presented at 1982 Materials Science Seminar "Deformation, Processing, and Structure" 23-24 October, 1982, St. Louis, Mo.

Los Alamos Los Alamos National Laboratory
Los Alamos, New Mexico 87545

STRAIN HARDENING OF HEAVILY COLD-WORKED METALS

S. S. Hecker and M. G. Stout
Materials Science and Technology Division
Los Alamos National Laboratory
Los Alamos, N. M. 87545

INTRODUCTION

The strain hardening behavior of materials is very important in structural response, metal working processes, and impact penetration problems. A precise description of strain hardening is particularly important in problems involving plastic instability. Large strains present some specific complications in testing and analysis. The large geometric changes and a variety of instabilities plague experiments. Hence, strain hardening descriptions at large strains are typically inferred from uniaxial tensile tests, which are restricted to modest strains (<0.5) by plastic instability. Such data are not only inadequate, but often misleading. The analysis of large strain problems are complicated by having to account correctly for material rotations. For large strain problems involving isotropic material behavior the use of the Jaumann stress rate tensor is adequate.[1] However, a number of investigators[2-5] have pointed out the shortcomings of this stress measure if used with anisotropic hardening criteria such as kinematic hardening.

In this paper we review large strain experiments from a variety of experimental techniques and attempt to establish proper constitutive descriptions. We are particularly interested in the role of deformation geometry (or stress state) on hardening response. We will also attempt to sort out the effects of texture, microstructure, and substructure. These effects are understood fairly well at small strains. Texture evolution plays a minor role at strains <0.3 and the variation of flow stress with material parameters such as crystal structure, grain size, and stacking fault energy is well documented. At large strains no satisfactory microstructural explanation of hardening exists. On the basis of undisturbed dislocation interactions, one expects steady state behavior and a saturation flow stress.[6,7] However, deformation inhomogeneities such as deformation bands and shear bands perturb the behavior. In addition, the roles of texture development

and twinning are important and not well understood. Consequently, hardening rather than saturation appears to be more common at large strains.

Finally, we will cite several practical consequences of large strain behavior. These are related to problems of plastic instability and sheet metal forming.

EXPERIMENTAL TECHNIQUES

The experimental difficulties associated with large strain testing are principally large geometry changes and a variety of instabilities which terminate experiments prematurely. These were reviewed previously.[8] A summary of techniques currently used is presented in Table I. Torsion of very short, thin-walled tubes is the only technique that permits a continuous determination of strain hardening to very large strains on reasonably homogeneously deformed specimens. All other tests require remachining or prestraining followed by a simple test. The limitation of having few decisive test techniques for determining large strain behavior is in large part responsible for the current lack of understanding in this area.

We will cite data generated by a large number of techniques. In our own work we have used principally the techniques of torsion on thin-walled tubes, compression with intermittant remachining, and sheet rolling followed by uniaxial tension.

MACROSCOPIC HARDENING

A number of phenomenological models used to describe hardening are summarized in Table II. The first three predict continued hardening, whereas the Voce type predict saturation at a stress σ_s. Kocks' mechanistic model also predicts saturation.[6] In fact, a plot of θ vs. σ presents a good graphical picture of the saturation stress. Kocks' model is based on dislocation interactions and predicts an early steady state saturation behavior. Figures 1 and 2 demonstrate the hardening behavior of 1100 aluminum deformed under several different modes. As shown in Fig. 2 hardening does not saturate but persists to high stresses at low rates (θ). Apparently some process intervenes at large strains (high stresses) and prevents a steady state balance. As mentioned above the reasons could be geometric (deformation mode and texture development)

or microstructural (different deformation mechanisms such as twinning, deformation or shear banding). A clear answer does not exist at present because no systematic studies have been conducted combining measurement of hardening, texture evolution and substructural evolution with analytical predictions.

DEFORMATION MODE

Torsion vs Axisymmetric Deformation Experiments

Stress-strain curves from torsion tests are compared to those obtained from axisymmetric tests (tension, compression, and wire drawing + tension) in Figs 3 to 6 for a variety of metals and alloys. These represent three fcc materials with widely different stacking fault energies and one bcc material.

Unfortunately, in most cases torsion and axisymmetric tests were not conducted on the same material (composition, texture, grain size, etc.). Nevertheless, the results indicate that on the basis of a von Mises effective stress-strain criterion the flow curve is lower for torsion and that saturation occurs at lower stress levels in torsion. The differences in flow stress levels between torsion and axisymmetric deformation are quite similar for the fcc materials. The effect is most dramatic for bcc iron. In most of the comparisons torsion was conducted on solid bars and some uncertainty in stress levels exist. However, the trends are quite clear.

Comparison of Other Deformation Modes

A careful and systematic study of the effect of stress state on hardening was conducted by the authors.[20] Thin-walled tubes of 70-30 brass were loaded in combined axial loading-internal pressure or torsion. The results were limited to moderate strain levels because of plastic instability. Stress-strain curves for a number of different stress states are shown in Fig. 7. The plane strain stress states (axial, $\varepsilon_z = 0$; hoop, $\varepsilon_\theta = 0$, and torsion) all exhibit similar hardening, less than that in uniaxial tension. The flow curve in hoop tension is the lowest. We believe this is a result of initial preferred orientation. The hardening rate for balanced biaxial tension is slightly lower

than uniaxial tension. However, continuation of the flow curve to larger strains is necessary for a definitive answer. The lower hardening rate in plane strain agrees with earlier experiments of a more indirect nature by Ghosh[21] and Wagoner.[22] Unfortunately, little large strain data exists. The available literature data shown in Fig. 8 in conjunction with our data presented in Fig. 5 demonstrate that hardening for plane-strain deformation is less than for axisymmetric deformation.

Razavi and Langford[27] compared axisymmetric wire drawing deformation to plane strain (strip drawing). Their results shown in Fig. 9 are similar to the brass results. At large strains the flow curve for strip drawing levels off whereas that for wire drawing continues to increase. The flow curve for torsion from Young and Sherby[17] is similar to that for strip drawing, albeit at lower stress levels. Similar results have been obtained on low-carbon steel. Figure 10 compares wire drawing + tension and torsion on 1007 steel. The results of Ford[28] on plane strain compression for 1008 steel are superimposed. Again, torsion and plane strain hardening levels off whereas axisymmetric hardening continues at large strains.

Changes in Deformation Mode

Most of the indirect large strain tests fall into this category. During prestraining large strains are applied in a deformation mode resistant to plastic instability. The prestrain operation is then followed by a simple stress state test (typically uniaxial tension) to determine the flow curve. A composite stress-strain curve for 1100 aluminum determined by rolling + tension is shown in Fig. 11. The resulting stress-strain curve can be represented as an effective flow curve by converting the rolling prestrain to a von Mises effective strain. The validity of such a curve depends, of course, on the independence of hardening from deformation mode, which has been demonstrated not to be the case. Hence, flow curves such as the one in Fig. 11 must be recognized as being complicated composites of two deformation modes.

In some cases the prestrain and final deformation are carried out in similar stress states. For instance, in wire drawing + tension both stress states are axisymmetric. Ford[28] compared the flow curves of low-carbon steel

determined by plane strain compression to rolling + plane strain compression (Fig. 12). Here the stress states are very similar. Yet the rolling + plane strain compression curve is different. Ford explained this difference on the basis of redundant work, explaining that the curvature of the rolls causes some redundant shearing (not contributing to thickness reduction) and extra hardening. Figure 13 shows a most dramatic effect of changing deformation mode. Sundberg et al.[29] found that rolling + tension in brass produced a rapidly rising flow curve, whereas rolling + plane strain compression showed immediate saturation. Unfortunately, he attached no scale to his plot; but the results are still most interesting. He noted that the plane strain compression tests exhibited immediate shear band formation.

Our experimental results for 70-30 brass comparing axisymmetric deformation and torsion are shown in Fig. 5. We also conducted a series of experiments prestraining in torsion followed by uniaxial tension. All specimens were thin-walled tubes. Test sections were 25.4 mm long, 12.14 mm in diameter with a 0.589 mm wall thickness. Specimens were carefully machined, annealed and electropolished before twisting. After twisting, they were unloaded, re-electropolished and strain gaged for tension testing. The resulting tensile curves are shown in Fig. 14 superimposed upon the previous torsion and compression curves. The two curves at smaller prestrains showed little uniform elongation, most of the deformation occurred in a localized neck. Hence, these flow curves are very questionable. The two curves for large prestrains definitely show that significant plastic flow in tension following a torsional prestrain takes much higher stresses than for torsion. In fact, the flow curves are very close to that observed for compression at the same von Mises strain level.

For 1100 aluminum we followed torsion with unaxial compression. Torsional prestrain was conducted on a solid round bar. The bar was then drilled out and bored to provide a thin-walled tube, 5.1 mm long, 4.8 mm in diameter with a 0.78 mm wall thickness. The thin-walled tube was then tested in compression. The resulting stress-strain curve for a von Mises prestrain of 3.9 is shown in Fig. 15. Again, the flow curve for axisymmetric flow (this time in compression) was much higher than that for torsion. The specimen buckled at a stress very close to that observed for straight compression at the same von Mises strain level.

Another most interesting experiment with changing deformation mode was conducted by Armstrong, Hockett and Sherby.[15] They compared monotonic, uniaxial compression (with interruptions for remachining) to sequential, multidirectional compression of 1100 aluminum. The multidirectional compression was conducted on a cube by compressing sequentially (by identical strain increments of 7.5 per cent) across the x y, and z faces of the cube. The flow stress was measured and plotted as a function of cumulative plastic strain. This composite flow curve is compared to the monotonic curve in Fig. 16. Initial hardening behavior is identical, but the multidirectional curve soon deviates and saturates at low stress levels. This behavior is similar to saturation observed in tension-compression fatigue where there is complete stress reversal.[30] Figure 16 also shows that when the loading is changed from monotonic to multidirectional or vice versa, the flow curves tend towards the current mode of loading. The transition from one type of hardening to the other is very gradual.

The results shown in this section demonstrate that significant changes in hardening occur with changes in deformation mode. This has important consequences in many practical applications. Some of the microstructural causes of the hardening effects will be discussed below.

CRYSTALLOGRAPHIC ANALYSIS AND TEXTURE EFFECTS

Analysis and Predictions

The most obvious effect of deformation geometry on hardening is the development of crystallographic texture. Because of the crystallographic nature of slip and the general validity of Schmid's law, one expects that at large deformations differences in hardening may arise from purely geometric considerations; that is, the mean inclination of the active slip planes and directions will change differently for different deformation modes. The quantitative prediction of this geometric effect has been the goal of many theoretical studies dating back to Sachs[31] in 1924 and Taylor[32] in 1938. Several excellent recent reviews have been written on this topic.[26,33,34] Jonas et al.[35] have recently examined the crystallographic considerations necessary for comparing hardening for different deformation modes. They correctly point out that even at small strains (before significant texture

development) crystallographic predictions of yield and flow differ from the macroscopic von Mises condition. For a randomly oriented fcc polycrystal one can relate the macroscopic stress (σ) to the critically resolved shear stress for slip (τ_c) and the macroscopic strain (ε) to the accumulated shear strain on all activated slip systems (γ_c) through the average Taylor factor $\bar{M}$. Specifically,

$$\sigma = \bar{M}\,\tau_c \tag{1}$$

$$d\varepsilon = \Sigma d\gamma_c/\bar{M} \tag{2}$$

$$\varepsilon = \int_0^{\gamma} \Sigma d\gamma_c/\bar{M}. \tag{3}$$

The Taylor factor varies with deformation mode. Bishop and Hill[36] showed that for tension $\bar{M}_t$ is 3.06 and for torsion $\bar{M}_\tau$ is 1.65.

One can now define a crystallographic effective stress and strain criterion if one assumes that microscopically the strain hardening law does not depend on deformation mode. A specific comparison of torsion and tension yields:[35]

$$\text{In torsion} \quad \tau = \tau_c \cdot \bar{M}_\tau \tag{4}$$

$$d\gamma = d\gamma_c/\bar{M}_\tau \tag{5}$$

Effective stress-strain definition gives

$$\bar{\sigma} = \bar{M}_t \cdot \tau_c = (\bar{M}_t/\bar{M}_\tau)\cdot\tau \tag{6}$$

$$d\bar{\varepsilon} = d\gamma_c/\bar{M}_t = (\bar{M}_\tau/\bar{M}_t)\cdot d\gamma \tag{7}$$

For the Bishop and Hill values of $\bar{M}_t$ and $\bar{M}_\tau$ these relations become $\bar{\sigma} = 1.85\ \tau$ and $d\bar{\varepsilon} = d\gamma/1.85$. This compares with the von Mises criterion or $\bar{\sigma}_{vm} = 1.732\ \tau$ and $d\bar{\varepsilon}_{vm} = d\gamma/1.732$. Therefore, the crystallographic yield and flow criterion predicts stress levels $\sim$ 7 per cent higher than the von Mises criterion as long as the Taylor factor remains constant. It should also be noted here that the Taylor-type analysis represents an upper bound crystallographic solution because it assumes that each grain undergoes identical

deformation. Lower bound solutions based on Sachs' assumption of equal stress on each grain also exist. Most experimental results favor the Taylor hypothesis, especially where the deformation is constrained.

At strains greater than ~0.3, crystallographic textures develop and do so differently for different deformation modes. Hence, the Taylor factors evolve differently. Predictions of Taylor factors for different deformation modes have been made by numerous authors. Most notable are the efforts of Chin and colleagues[34,37,38] and Gil Sevillano, Van Houtte and Aernoudt.[26,39] Most of the predictions use the Bishop and Hill formalism and the resulting evolution of Taylor factors with deformation (taken from Reference 26) is shown in Fig. 17. For axisymmetric deformation the Taylor factor increases substantially; more so for tension than for compression. For torsion the Taylor factor decreases. One can again develop a crystallographic effective flow criterion by using these Taylor factors in eqs. (6) and (7). Equation (7) now must be integrated because the ratio $(\bar{M}_\tau/\bar{M}_t)$ is no longer constant.

All of the crystallographic analyses mentioned above assume random initial orientations and do not take account of changing grain shapes during deformation. The effect of changing grain shapes on crystallographic slip has recently been examined by Kocks and coworkers.[40-42] They have found that in some deformation modes elongated grain shapes can relax some of the constraints on slip and decrease the number of necessary slip systems. Canova, Kocks, and Jonas[42] conducted a complete crystallographic analysis of torsion and predict the evolution of $\bar{M}_\tau$. Their results are cited in abbreviated form by Jonas et al.[35] The major difference between their method (called method of relaxed constraints) and that of Gil Sevillano et al.[26,39] (Bishop and Hill type shown in Fig. 17) is that Canova et al. predict $\bar{M}_\tau$ to rise after strains in excess of $\bar{\varepsilon} = 2$. For instance, at an effective strain of ~ 4 they predict $M_\tau = 1.68$ compared to ~ 1.5 for Gil Sevillano et al. Similar calculations for axisymmetric deformation are not yet available.

All of the above predictions are made for high stacking fault energy (SFE) fcc metals; copper and higher. For low SFE metals and alloys deformation by twinning becomes a complicating factor. Chin et al.[43] and van Houtte.[44] have developed calculational methods to incorporate twinning into the prediction of Taylor factors. These methods are reviewed in Reference 26 and will not be discussed here.

Texture Experiments

A very large body of literature exists on texture measurements of metals and alloys. Those measurements relevant to current discussions have been reviewed by Gil Sevillano et al.[26] In high SFE metals (copper, nickel, aluminum) and for axisymmetric extension it is generally found that a strong <111> fiber texture plus a weaker <100> texture develops. In compression, grain rotation is in the opposite direction resulting in a strong <110> texture. These textures are generally consistent with the Bishop and Hill predictions and the changes in Taylor factor shown in Fig. 17.

In low SFE metals and alloys the emergence of twinning as a deformation mode has the effect of increasing the <100> component of the axisymmetric extension texture. A low SFE introduces additional complications of changes in latent hardening and deformation faulting (see Chin et al.[43] and van Houtte[44]). Experimentally for 70-30 brass the <100> fiber texture becomes much stronger than the <111> fiber component.[45] In compression lower SFE results in a relatively weak <111> component in addition to the strong <110> texture. This compares to high SFE metals which develop a <100> secondary component.

Gil Sevillano et al [39] used a Bishop and Hill analysis to predict shear textures. For high SFE metals they predict an S1 copper-type of two partial fiber textures; (uvw) [$1\bar{1}0$] and (111) [hkl]. For low SFE metals the S3 brass type is similar but with different density distributions. Shear experiments on copper[46,47,48] and aluminum[47,48,49] generally confirm the partial fiber textures. Regenet and Stüwe[48] also found that a (100) [011] is actually the strongest component. This is predicted by the method of relaxed constraints but not by the Bishop and Hill method. For 70-30 brass Backofen and Hundy[50] approximated the shear texture by three ideal orientations, ($11\bar{1}$) [112], (112) [$11\bar{1}$], and (110) [001]. Williams[47] found similar results except for some of the symmetry assumed by Backofen and Hundy.

Texture Correction to Flow Curves

The torsion flow curves for copper (Fig. 3) are converted to crystallographic effective stress-strain curves in Fig. 18. The original shear stress-shear strain curves were converted to the crystallographic effective stress and strain by using eqs. (6) and (7) and the average Taylor factors

as a function of strain shown in Fig. 17. Figures 18a and 18b also show the crystallographic correction for torsion using the method of relaxed constraints.[42] It is quite clear that the crystallographic criterion yields better agreement than the von Mises criterion at small to moderate strains, but overcorrects at large strains. The method of relaxed constraints gives better agreement at large strains, but the shape of the flow curve is inconsistent with experiment. Similar corrections are made for aluminum and brass in Figs. 19 and 20. The correction for brass is only approximate because we used the Taylor factors of Fig. 17 which were developed for high SFE metals. These comparisons show that the texture corrections are of the right magnitude. Unfortunately, they are not conclusive because in most experiments tension tests (or other axisymmetric deformation modes) were not conducted on the same material (composition, texture, grain size, etc.) as torsion tests. Also data reduction in torsion is often questionable. The problems associated with torsion of solid bars are discussed in detail by Canova et al.[51] An additional complication is that most of the materials tested possessed an initial texture and were not randomly oriented polycrystals as assumed in the Taylor analysis.

The influence of initial texture is demonstrated in Fig. 7 where the axial and hoop tension flow curves differ substantially. The curves are in qualitative agreement with the initial textures.[20] The plane strain and torsion curves are in general agreement with evolving Taylor factors. The balanced biaxial tension curve also agrees qualitatively. The lower hardening rate at larger strains is consistent with the expected change in Taylor factors (Fig. 17) because balanced biaxial tension should be equivalent to through-thickness compression.

Figure 6 shows the flow curve comparison for bcc iron. Texture predictions for {110} <111> slip in bcc metals is similar to fcc metals, except axisymmetric tension in bcc metals is equivalent to compression in fcc metals. Therefore, the predominant texture for wire drawings in iron is {110} <100>. The shear texture in Armco iron has been reported by Backofen and Hundy[50] to be principally (112) [1$\bar{1}$0] and (110) [1$\bar{1}$2]. Both of these orientations place a [111] slip direction along the transverse direction of maximum shear. The evolution of Taylor factors is not as well developed for bcc metals. However, several authors[27,52,53] explain the bcc results in Figs. 6 and 9 by texture development. Gil Sevillano and Aernoudt[52,53] claim that most deformation modes lead to hardening and that torsion represents the unusual case. They maintain that the torsion

texture permits the slip distance to remain unchanged at moderate strains and actually increase at large strains because of dynamic recovery. Razavi and Langford[27] relate the continued hardening during wire drawing to redundant strain (curling of grains) necessary to maintain grain compatibility. In strip drawing and torsion, deformation may be accommodated by cooperative rearrangements such as shear bonding, leading to a lower hardening rate. Young et al.[19,54] and Weertman and Hecker[55] have proposed explanations based on substructure as explained below.

The path change experiments (Figs. 13 to 16) provide another comparison for texture-based hardening predictions. We have determined a partial pole figure for the brass tube in Fig. 14 prestrained in torsion by $\gamma = 2.4$ ($\varepsilon_{vM} = 1.39$). Figure 21 shows the partial (111) pole figure on the brass tube along with the results of Backofen and Hundy on brass rod for $\gamma = 3.2$. These pole figures show that the shear deformation aligns {111} planes in (or close to) the axial direction. The Taylor factor for an ideal {111} orientation is the highest possible and, hence, one would expect the stress required for plastic flow in axial tension following torsion to be high. Qualitatively this is what is observed at large prestrains. As mentioned below the tensile data subsequent to smaller torsional prestrains is questionable. Williams[47] showed that the torsion textures are well developed at strains >0.5. Therefore, we would expect a "stiff" response following all torsional prestrains >0.5. It is also of interest to note that Williams found that the same torsional textures developed irrespective of original texture. The manifestation of this on flow behavior has not been investigated.

Compression following torsion in 1100 aluminum is shown in Fig. 15. Witzel[49] found that the end texture in torsion for aluminum could be described completely by two ideal orientations (112) $[1\bar{1}0]$ and (112) $[\bar{1}10]$. Such a texture again makes the axial direction "stiff" and one should expect the flow stress in compression to be greater than that for continued torsion. We have yet to determine the textures developed in our specimens.

The results of Sundberg et al.[29] (Fig. 13) are very sketchy. For the rolling texture determined by Hu et al.[56] we would not expect such a dramatic difference in response for tension compared to plane strain compression following rolling. It is quite likely that deformation mechanisms such as twinning and shear banding may control flow and, hence, not agree with a Taylor-type analysis.

Let us now consider the rolling + tension results on 1100 aluminum shown in Fig. 11. Tensile specimens in the rolling and transverse directions were tested following various rolling prestrains. A plot of the ultimate tensile strengths as a function of rolling prestrain is shown in Fig. 22. The transverse and rolling direction results are nearly identical, with the transverse specimens being slightly stronger. A look at rolling textures (Fig. 23 for two reductions on our material by O'Rourke[57] and Fig. 24 for the literature result from Hu et al.[56]) indicates the transverse direction should be stronger. However, the pole figures suggest that the 45° direction should be much weaker than either. We have recently repeated the experiments of Fig. 22 with a different lot of material and tested specimens in all three directions for prestrains of 1.2 to 4.0. In all cases the response was essentially identical, with the 45° specimens never being more than 2 percent weaker than the transverse specimens.

No texture determinations were performed on the aluminum specimens deformed unidirectionally and multidirectionally in Fig. 16. We expect the unidirectional specimens to develop the standard [110] fiber texture with a weaker spread from [110] to [311]. It is not clear what kind of (if any) texture the multidirectional loading will develop. The substructural investigations conducted for these experiments will be discussed below.

The comparisons of texture predictions and experiments presented in this section show that texture can predict many of the observed macroscopic hardening responses at large strains in a qualitative manner. However, we are far from a complete quantitative understanding of texture effects on hardening. Much more effort is required to conduct good systematic experiments for different deformation modes where textures are measured as a function of deformation and represented quantitatively by crystallite orientation distribution functions.[58-61] At the same time more detailed predictions (of the type of Canova, Kocks, and Jonas[42]) of texture evolution and its effect on the flow curve are needed for a variety of deformation modes.

MICROSTRUCTURAL AND SUBSTRUCTURAL EFFECTS

We expect that in a complete description of strain hardening texture is only one of several important factors. Other microstructural and substructural features often play an important role. These may include

solute atoms, precipitates, second phases or particles, twins, and dislocation structures such as cells, subgrains or microbands. The relationship between the flow stress and these microstructural features has been studied extensively at small strains. At large strains there have been few systematic studies. The recent literature is reviewed by GVA.[26] In this section we will concentrate on the effects of solutes and dislocation substructures in fcc metals and alloys.

Effect of Purity (Solutes) on Hardening

A careful review of the large strain literature shows the important effect of purity or solute hardening.[6] Figure 25 shows a collection of flow curves for aluminum with different purities and dilute alloying additions. The results clearly show that high-purity aluminum tends to saturate at low stress levels (note that the torsion curve of Luthy et al.[65] is for -20°C). Low-purity or alloyed aluminum exhibits continued hardening to large strains. The results for copper shown in Fig. 26 are similar. Most of the literature data for fcc metals support the observation that high purity leads to saturation regardless of deformation mode. Furthermore, the effect of small amounts of solutes on the flow stress and hardening rate is substantial as shown in Figs. 25 and 26. The flow curves for a number of fcc metals of commercial purity in Fig. 27 show that continued hardening at large strains is very common. Little data are available for purity effects in alloys. We expect these effects to be less dramatic and overshadowed by the solute effects from the intentional alloying elements.

Solutes affect hardening at large strains principally by retarding dynamic recovery processes, thereby offsetting the balance between dislocation generation and annihilation required for steady state and saturation. A quantitative description of the solute-dislocation interactions at large strains has not been developed. In a qualitative sense it is easily recognized that solutes will hinder the cross slip or climb processes required for dynamic recovery. The magnitude of the large solute effects at large strains had not been previously recognized. Kocks[71] presents some new aspects of solute hardening in this volume.

The effects of solutes on texture development have not been sorted out in detail. However, there are a number of references in the literature such

as that of Backofen which indicate that small solute differences have little effect on texture development. On the other hand, Ridha and Hutchinson[72] showed that significant textural effects upon annealing can be caused by small changes in chemistry.

Alloying to form precipitates, dispersed particles, or large inclusion particles can have dramatic effects on the flow curve. These range from flow softening in some Al-Cu alloys[73] to a fiber reinforcing effect in high sulfur steels.[74]

Evolution of Substructure

At small strains the evolution of dislocation substructure depends on crystal structure and SFE in addition to the imposed parameters of temperature and strain rate. At low homologous temperatures ($T/T_m < 0.4$) fcc metals with a high SFE and bcc metals form well developed dislocation cell structures, whereas fcc metals and alloys with a low SFE tend to form planar dislocation arrangements that typically lead to higher strain hardening rates. A complete description of how substructure evolves at large strains is not yet available. Only in recent years have investigators performed multi-surface transmission electron microscopy. This is particularly important and difficult for the case of rolling and other deformation modes where one specimen dimension becomes very small at large strains. The most complete studies of deformation substructure have been carried out on pearlitic steels[75-78] and copper and it alloys.[66,69,79-83] Many of these results are reviewed by GVA.[26] Fewer studies have been conducted on high SFE metals. We will use our work on commercial purity aluminum and nickel to illustrate some of the important substructural developments.

Our experiments on 1100 aluminum involved prestraining by rolling at room temperature ($T/T_m = 0.32$) and subsequently testing in tension. (Rolled sheets were immersed in cold tap water immediately after rolling to keep the temperature rise to a minimum.) The flow curves shown in Figs. 3 and 25 show continued hardening. Specimens for transmission electron microscopy (TEM) were prepared from rolled sheet of many different prestrain levels. Most of the TEM observations to date were made through the sheet surface. Figure 28 shows a series of TEM micrographs at different strain levels. Unfortunately, to date we

have examined specimens from only two prestrain levels in the other two directions (edge-on in the rolling direction and edge-on in the transverse direction). The thinning techniques for such specimens have been described by Rohr and Hecker.[84]

We will use the through-surface observations first to explain the general substructural evolution. Figure 28a shows that by a strain of 0.11 a definite dislocation cell network has developed. With increasing deformation this cell network decreases in size and the cell boundaries sharpen up. By a strain level of 0.28 we find distinct evidence of dynamic recovery (Fig. 28b). Many of the cell boundaries have recovered into higher misorientation subgrain boundaries that exhibit a distinct boundary contrast instead of the dislocation character of cell walls. With continued deformation we find that more and more of the structure takes on a recovered appearance. However, new cells appear to be created within the newly recovered subgrains. Both cells and subgrains continue to become smaller up to strain levels of $\sim$ 2. Beyond this strain level, we find little change in the dimensions of through surface cells and subgrains. The substructural dimensions were measured statistically (many hundreds per strain level) and are shown in Fig. 29. At very large strains the substructure was predominantly of subgrain character. We also measured the average misorientation of cells and subgrains in the TEM field of view ($\sim$ 2 μm diameter) and found that the misorientation increased continuously with strain, averaging $\sim$ 10 degrees at a strain of 6.

As expected, the through-surface observations are only of limited value because they do not reflect the most important structural features. TEM micrographs of the two edge-on observations are shown in Fig. 30 and 31. At a strain of 1.0 we found a cell/subgrain structure of elongated ribbon shape with distinct evidence of microscopic shear bands (which we will call microbands). Microbands were limited to single grains and were observed only occasionally. The structure at a strain of 2.3 is well developed into a ribbon-like subgrain and cell structure as shown in the bright field/dark field micrographs of Fig. 31. We found no evidence of microbands at this strain level. The substructural dimensions are shown in Fig. 29 along with those taken from the through-surface observations. We also show an extrapolation of cell and subgrain sizes to zero strain and draw a line that represents the imposed geometrical shape change. The experimental results indicate that at small strains both cells and subgrains are reduced in size more rapidly than the

imposed shape change. This demonstrates that new cells and subgrains are being formed continuously. At large strains we have no edge-on measurements.

Similar results were obtained previously by Schuh and von Heimendahl[85] on higher purity aluminum (99.98% Al). Again no edge-on measurements are available beyond a strain level of 1.2. However, their in-plane substructure dimensions appeared to saturate at $d_l \cong 1.1$ μm and $d_t \cong 0.7$ μm (see Ref. 26). They did not try to distinguish between cells and subgrains, and hence a direct comparison to our data is not conclusive.

The ease and extent of dynamic recovery in aluminum was somewhat surprising. Therefore, we conducted similar experiments on commercially-pure nickel (Nickel 200) at room temperature.[70] This represents a much lower homologous temperature (0.16 for Ni and 0.32 for Al) while still working with a high SFE metal. The flow curve resulting from R+T experiments is shown in Fig. 27. Transmission microscopy observations were reported by Zimmer et al.[70] The general evolution of substructure is similar to that found for aluminum. However, the dislocation cell structures dominate to much larger strains. Dynamic recovery does occur with subgrains being quite distinct at a strain of 1.6. We also found evidence of microbands at intermediate strain levels ($\sim$ 1.6) and no microbands at very large strains. The results of Zimmer et al.[70] are shown in Fig. 32 along with one large strain edge-on measurement made since then.[86] The TEM micrographs for this strain level are shown in Fig. 33. The evidence for substantial dynamic recovery and subgrains is clear.

In nickel the substructural dimensions continue to decrease with strain. We also find a continued increase in flow stress (Fig. 27). We are still puzzled by the rapid increase in hardening at strains $\sim$ 4. In our previous analysis[70] we suspected the possible influence of grain size at large strains proposed by GVA.[26] Their ideas are represented in Fig. 34. They observed that the decrease in grain size dictated by the geometric shape change is more rapid than the decrease in substructural dimensions observed in the literature. Hence, at large strains it is possible that grain boundaries may again play an important role in hardening. The most recent results on nickel (Fig. 32) are not consistent with the hardening transition at a strain of 4. One must now question the generally accepted observation of a saturation in substructural dimensions at large strains. To our

knowledge, the nickel results in Fig. 32 represent the largest strains at which edge-on measurements were made and they do not show saturation.

The substructure of heavily cold rolled and low SFE copper alloys has been studied extensively.[66,69,79-83] Hatherly and Malin[82] found that microbands form at strains as low as 0.2 in copper. Microbands are long thin sheet-like features that form on {111} planes amidst a well developed cell structure (see Fig. 35). With continued deformation they cluster together and become parallel to the rolling plane. Shear bands develop at larger strains and dynamic recrystallization has been observed at very large strains.[66] In lower SFE copper alloys stacking faults and fine twins develop at low strain levels. In 70-30 brass twins cluster together to form banded regions, but by a strain of 0.4 most grains are uniformly twinned and shear bands begin to develop.[82] The first shear bands develop in the grains that are most profusely twinned. Macroscopic shear bands that cut across the full sheet thickness and are $\sim 35°$ to the rolling plane eventually develop. The exact role of microbands, twins, and shear bands in accommodating the imposed shape change and in controlling the flow stress has not yet been determined. From our work on aluminum and nickel and the work of Hatherly, Malin and coworkers[80-83] we have drawn up a summary of microstructural observations in Table III.

Relationship Between Substructure and Flow Stress

The relationship between substructural features and flow stress is not well understood. A Hall-Petch type of relation ($\sigma = \sigma_o + kd^{-m}$ where σ_o is a friction stress and k a strength constant) is generally acknowledged.[87-89] There is still much controversy over the exponent m. It appears that m = 1 is well accepted where d represents dislocation cells. However, for recovered subgrains a value of m = 1/2 is often found.[88] For the case of cold worked aluminum both cells and subgrains are present. A detailed correlation between flow stress and the substructural features shown in Fig. 29 is not yet possible because insufficient through-thickness measurements exist. However, preliminary attempts indicate that at large strains the misorientation across subgrain boundaries needs to be incorporated. Armstrong et al.[15] also found that they were able to correlate flow stresses in unidirectional vs multi-directional compression by separately including the density of dislocation tangles, cell size, and subgrain size multiplied by the square root of the

misorientation. The complex behavior of nickel (Fig. 27) has not yet been explained.

The even more complicated behavior resulting from changes in deformation mode has not been studied extensively by electron microscopy. Detailed investigations such as those performed in fatigue studies[30,90] are in order. Weertman and Hecker[55] have recently proposed a possible explanation for the difference in strain hardening at very large plastic strains for torsion compared to axisymmetric deformation. It is shown that in torsion deformation is accommodated principally by dislocation of the same Burgers vector (of opposite sign) whereas axisymmetric deformation requires dislocations from several different slip systems. In torsion this results from the evolution of a texture that has the predominant slip planes sharing the same slip direction (tangential to the specimen surface). Because the dislocations tend to clump into cell walls the torsion case leads to easier annihilation and hence on earlier approach to steady state (saturation). This behavior is particularly dramatic for iron (Fig. 6), but also appears to hold for most fcc metals and alloys.

We are convinced that a true correlation of flow stress with microstructural features will need to include both texture and substructure. As mentioned above more systematic experiments are required to sort out the texture hardening contribution. The modeling of texture evolution by the method of relaxed constraints (Canova, Kocks, and Jonas[42]) holds great promise. However, careful experiments are required in which textures are measured as a function of deformation, converted to crystallite orientation distribution functions, and related to flow stress through a Taylor-type analysis. To assess the proper role of substructure more through-thickness measurements of substructural dimensions are required. Also one must examine the objections raised by Truckner and Mikkola[67] about TEM measurements and evaluate the benefits of their X-ray line broadening measurements.

Some Properties of Heavily Cold Worked Metals

Residual Elongation after Rolling

In our work on commercially pure aluminum and nickel we found that the flow stress as determined by subsequent tensile tests increased with

increasing prestrain. One would expect the residual elongation in tension following rolling to decrease with increasing prestrain. The rolling experiments were conducted to provide specimens of identical thickness after different amounts of prestrain to avoid potential complications from thickness effects. This was accomplished by first reducing the original aluminum bar to different starting thicknesses, annealing at 343°C for one hour, followed by rolling to final thickness. (The starting grain sizes of all specimens prepared this way were similar). For the case of aluminum we produced specimens of two different final thicknesses, 0.127 mm and 0.635 mm. The results for aluminum and nickel are shown in Fig. 36 and 37.

As expected both uniform and total elongations drop rapidly with increasing prestrain. In aluminum, the total elongation increases for both thicknesses at large strains. The uniform elongation definitely increases for the 0.127 mm sheet but appears constant for the 0 635 mm sheet. However, the prestrain levels for the thicker sheets were lower. In nickel, both uniform and total elongations decrease rapidly, remain constant, and then increase at strain levels > 4. This is most intriguing since the flow stress also increases dramatically at these strain levels (Fig. 27). In fact the combinations of strength levels and total elongation for the very large prestrains (250 MPa and 4% for aluminum, and 1400 MPa and 5% for nickel) are remarkable.

The rapid decrease in tensile elongation after rolling is easily understood by referring to Fig. 38. It is well known that tensile instability will occur when $d\sigma/d\varepsilon = \sigma$. Figure 38 shows the curve for σ and $\theta = (d\sigma/d\varepsilon)$ as a function of strain. They cross at the point where tensile instability is observed in an annealed specimen ($\varepsilon \sim 0.25$). As shown, the flow stress can be increased much beyond the tensile ultimate strength by rolling prestrain. However, the intrinsic hardening rate ($d\sigma/d\varepsilon$) decreases. For the prestrain of 2.3 (90 percent rolling reduction) chosen in Fig. 38 we demonstrate how the flow stress has been increased much above the level that could be supported by the intrinsic hardening rate. Hence, a tensile specimen should go unstable immediately upon yielding and little tensile elongation is to be expected.

The actual tensile loading response is shown in Fig. 39. The prestrained tensile specimen does not exhibit completely elastic loading followed by an abrupt plastic transition to the master flow curve. Instead, the flow curve is somewhat rounded as shown in Fig. 39. This more gradual yielding results from a generalized Bauschinger effect (tension following rolling) and from

any dynamic recovery during the rolling process. As a result, the hardening rate θ is initially increased enormously and permits some uniform plastic flow before instability. However, as shown by the curve θ_t (for tension) in Fig. 39, the hardening rate decreases very rapidly towards θ_R (for the master flow curve in rolling) and very little stable flow occurs. We propose that the increase in elongation at very large prestrains results primarily from the more complete dynamic recovery at large strains. Dynamic recovery allows the tensile flow curve to bend over gradually increasing θ_t and the tensile uniform elongation. An additional factor increasing the total elongation may be an increase in strain rate sensitivity with prestrain. A few preliminary tests showed that prestrained aluminum was more rate sensitive than annealed aluminum.

Biaxial Ductility of Cold Worked Metals

Biaxial ductility or resistance to local necking can be characterized by failure (or forming) limit curves (FLCs).[91] Hecker[92] previously reported the influence of prior cold work (by rolling) on the FLCs of 1100 aluminum. The results are shown in Fig. 40 for several prestrain levels. It is quite apparent that prestrain lowers the ductility much more in tension and plane strain ($e_2 = 0$) than in biaxial tension. In fact, the local necking strains of 32 x 32 percent for 90 percent cold rolled aluminum are remarkable. We can now explain this behavior based on the large-strain results discussed above. The flow curve of Fig. 39 demonstrates unequivocally that 1100 aluminum still possesses substantial intrinsic ductility after 90 percent prestrain because of continued work hardening to strain levels of at least seven. As explained above the lack of tensile ductility following prestrain is strictly a problem of geometric instability in uniaxial tension. The plane strain behavior suffers similarly. However, in biaxial tension of sheet (either hydraulic bulging or punch stretching) there is added geometric stability (see Ghosh and Hecker[93] and Stout and Hecker[94]) and, hence, the material is able to take better advantage of its intrinsic hardening and exhibit much greater ductility.

The intrinsic hardening behavior at large strains is very important. For instance, if a material exhibits no hardening at large strains (saturation), then very little additional ductility would be expected even for biaxial deformation. The importance of the intrinsic hardening curve at large strains was

demonstrated convincingly by Bird and Duncan[95] in comparing the behavior of 1008 steel, 1100 Al and 2036-T4 Al. The FLCs for these two materials as determined by Hecker[91] are shown in Fig. 41. The strain hardening rates (n-value from $\sigma = k\varepsilon^n$) in uniaxial tension were between 0.21 and 0.26 for all three materials. The low FLC for 2036-T4 Al was explained on the basis of its negative strain rate sensitivity (m-value of -0.005 from $\sigma = k'\dot{\varepsilon}^m$). However, steel has a positive rate sensitivity of m = 0.012 whereas 1100 aluminum is rate insensitive and, hence, the FLC for steel should be higher. Bird and Duncan[95] showed that strain hardening at large strains provides the answer. Figure 4 [illegible]s the hardening rate normalized with respect to stress during bi[illegible]sion[95] (hydraulic bulging). At strains greater than the level where $\sigma \frac{d\sigma}{d\varepsilon} = 1$ (beyond uniform strain in tension), the hardening rates for the three materials differ substantially. The higher rate in 1100 Al apparently offsets the zero strain rate sensitivity in the failure limit curve behavior.

CONCLUDING REMARKS

We have shown sufficient evidence to demonstrate that strain hardening in torsion can not be correlated with axisymmetric deformation by the von Mises effective stress strain criterion. In fcc materials, the flow stress levels and strain hardening rates are typically lower in torsion and saturation, if it occurs, is observed at lower stress levels. In bcc iron, a low saturation stress is observed for torsion, whereas linear hardening is observed for axisymmetric extension. Experiments also suggest that flow stress levels and strain hardening rates are also low for other plane strain deformation modes when compared to axisymmetric deformation.

Much of the discrepancy in flow curves can be explained by texture. We demonstrated that a crystallographic effective stress-strain criterion based on evolving average Taylor factors provides the proper magnitude correction for torsional flow curves in fcc materials. However, the details of the hardening behavior are not fully explained. This is, in part, a result of inadequate systematic experimental work at large strains. The crystallographic analysis must also be extended to predict the response of initially anisotropic materials and account for grain shape changes as was done for torsion by Canova, Kocks, and Jonas.[42]

The simple crystallographic analysis presented here also does not fully explain the hardening response following deformation path changes and multi-directional loading. Moreover, the strong effects of purity and grain size (discussed in Ref. 8) suggest an important microstructural dependence of hardening in addition to the texture effect. Much remains to be learned about the evolution of substructure and the influence of cells, subgrains, and substructural features such as microbands, twins, shear bands on hardening. Additional three-surface transmission electron microscopy at very large deformations is needed.

ACKNOWLEDGEMENTS

The support of the Division of Materials Sciences, Office of Basic Energy Sciences, US DOE is gratefully acknowledged. We also thank K. A. Johnson, J. A. O'Rourke, D. L. Rohr, and K. P. Staudhammer for their experimental assistance and G. R. Canova, U. F. Kocks, and J. J. Jonas for helpful discussions.

REFERENCES

1. R. McMeeking and J. R. Rice, "Finite-element Formulations for Problems Large Elastic-Plastic Deformation," Int. J. Solids Struct., 1975, vol. 11, pp. 601-616.

2. E. H. Lee, R. L. Mallett, and T. B. Wertheimer, "Stress Analysis for Kinematic Hardening in Finite-Deformation Plasticity," Stanford University Report, SUDAM Report No. 81-11, December 1981.

3. V. A. Lubarda and E. H. Lee, "A Correct Definition of Elastic and Plastic Deformation and Its Computational Significance," Stanford University Report, SUDAM 80-1, January 1980, also to appear in J. Appl. Mech.

4. J. C. Nagtegaal and J. E. deJong, "Some Aspects of Nonisotropic Workhardening in Finite Deformation Plasticity," Proc. Workshop on "Plasticity of Metals at Finite Strains: Theory, Experiment and Computation," Stanford University June 1981, eds. E. H. Lee and R. L. Mallett.

5. E. H. Lee, "Some Comments on Elastic-Plastic Analysis," Stanford University Report, SUDAM Report No. 80-5, October, 1980

6. U. F. Kocks, "Laws for Work-Hardening and Low Temperature Creep," J. Eng. Mater. Tech. Trans. ASME, 1976 vol. 98, pp 76-85.

7. H. Mecking and A. Grinberg, "Discussion on the Development of a Stage of Steady-State Flow at Large Strains," in Proceedings of 5th International Conference on Strength of Metals and Alloys, eds. P. Haasen, V. Gerold, and G. Kostorz, Pergamon Press, 1980, pp. 289-294.

8. S. S. Hecker, M. G. Stout and D. T. Eash, "Experiments on Plastic Deformation at Finite Strains," in Proceedings of Plasticity of Metals at Finite Strain: Theory, Experiment and Computation," Stanford University June 1981, eds. E. H. Lee and R. L. Mallett.

9. J. H. Hollomon, "Tensile Deformation," Trans. AIME, 1945, vol. 162, pp. 268-290.

10. P. Ludwik, "Elemente der Technologischen Mechanik," 1909, Springer Verlag, Berlin.

11. H. Swift, "Plastic Strain in an Isotopic Strain-hardening Material," Engineering, vol. 162, p. 381.

12. E. Voce, "The Relationship Between Stress and Strain for Homogeneous Deformation," J. Inst. Metals, 1948 vol. 74, pp. 537-562.

13. E. Voce, "A Practical Strain-Hardening Function, Metallurgia, 1955, vol.51, pp. 219-226.

14. J. E. Hockett and O. D. Sherby, "Large Strain Deformation of Polycrystalline Metals at Low Homologous Temperatures," J. Mech. Phys. Solids, 1975, vol. 23, pp. 87-98.

15. P. E. Armstrong, J. E. Hockett, and O. D. Sherby, "Large Strain Multidirectional Deformation of 1100 Aluminum at 300 K," J. Mech. Phys. Solids, 1982, vol. 30, pp 37-58.

16. J. Gil-Sevillano, Ph.D. Thesis, Katholieke Universiteit Leuven, 1974.

17. O. D. Sherby and C. M. Young, "Some Factors Influencing the Strain Rate-Temperature Dependence of the Flow Stress in Polycrystalline Solids," Rate Processes in Plastic Deformation of Materials, eds. J.C.M. Li, and A. K. Mukherjee, American Society for Metals, 1975, pp. 497-541.

18. G. I. Taylor and H. Quinney, Proc. Royal Soc. London, 1, 1934, vol. 143, p. 307.

19. C. M. Young, L. J. Anderson and O. D.Sherby, "On the Steady State Flow Stress of Iron at Low Temperatures and Large Strains," Met. Trans., 1974, vol. 5, pp. 519-520.

20. M. G. Stout and S. S. Hecker, Unpublished work, Los Alamos National Laboratory.

21. A. K. Ghosh, "Plastic Flow Properties in Relation to Localized Necking in Sheets," in Mechanics of Sheet Metal Forming-Material Behavior and Deformation Analysis, eds. D. P. Koistinen and N-M. Wang, 1978, Plenum Press, pp. 287-312.

22. R. H. Wagoner, "Plastic Behavior of 70-30 Brass Sheet," Met. Trans. A., 1982, vol. 13A, pp. 1491-1500.

23. DGM, Wire Drawing Commission, "Fliesskurven verschiedener Werkstoffe," 1975.

24. P. Blanchard, D. Whitwham and J. Herenguel, Ecrouissage, Restauration, Recristallisation, Presses Universitet de France, 1963, p. 41, Paris.

25. L. E. Murr and F. I. Grace, "Residual Structure and Mechanical Properties of Alpha Brass and Stainless Steel Following Deformation by Cold Rolling and Explosive Shock Loading, " Trans. AIME, 1969, vol. 245, pp. 2225-2235.

26. J. Gil-Sevillano, P. van Houtte and E. Aernoudt, "Large Strain Work Hardening and Textures," Progress in Materials Science, 1980, vol. 25, pp. 69-412.

27. A. Razavi and G. Langford, "Strain Hardening of Iron: Axisymmetric vs. Plane Strain Elongation," in Proceedings of 5th International Conference on Strength of Metals and Alloys, eds. P. Haasen, V. Gerold, and G. Kostorz, 1980, Pergamon Press, pp. 831-836.

28. H. Ford, "The Working Properties of Metals and Their Relationship to Mechanical-Test Behavior," J. Inst. Metals, 1968, vol. 96, pp. 65-74.

29. R. Sundberg, L.-E. Olsson, and B. Thundal, "Microstructure of Heavily Deformed Brass and Nickel Silver," Jernkont. Ann., 1971, vol. 155, pp. 434-436.

30. H. Mughrabi, "The Cyclic Hardening and Saturation Behavior of Copper Single Crystals," Mat. Sci. and Engng., 1978, vol. 33, pp. 207-223.

31. G. Sachs, Z. Verein Deut. Ing., 1924, vol. 72, p [illegible].

32. G. I. Taylor, "Plastic Strain in Metals," J. Inst. Metals, 1938, vol. 62, pp. 307-324.

33. U. F. Kocks, "The Relation Between Polycrystal Deformation and Single Crystal Deformation," Met. Trans., 1970, vol. 1, pp. 1121-1143.

34. G. Y. Chin, "The Role of Preferred Orientation in Plastic Deformation," in Inhomogeneity of Plastic Deformation, ed. R. E. Reed-Hill, American Society for Metals, 1973, pp. 83-112.

35. J. J. Jonas, G. R. Canova, S. C. Shrivastava, and N. Christodoulou, "Sources of the Discrepancy between the Flow Curve Determined in Torsion and in Axisymmetric Tension and Compression Testing," Proc. of Research Workshop on "Plasticity of Metals at Finite Strain: Theory, Experiment and Computation," Stanford University, June 1981, eds. E. H. Lee and R. L. Mallett.

36. J. F. W. Bishop and R. Hill, "A Theory of the Plastic Distortion of a Polycrystalline Aggregate under Combined Stresses," Phil. Mag., 1951 vol. 42, pp. 414-427

37. G. Y. Chin and W. L. Mammel, "Computer Solutions of the Taylor Analysis for Axisymmetric Flow," Trans. AIME, 1967, vol. 239, pp. 1400-1405.

38. G. Y. Chin, W. L. Mammel and M. T. Dolan, "Taylor Analysis for {111} <110> Slip under Conditions of Axisymmetric Flow," Trans. AIME, 1969, vol. 245, pp. 383-388.

39. J. Gil-Sevillano, P. van Houtte, and E. Aernoudt, "Calculation of Shear Texture with the Taylor-Analysis," Z. Metallkunde, 1975, vol. 66, pp. 367-373.

40. U. F. Kocks and H. Chandra, "Slip Geometry in Partially Constrained Deformation," Acta Met., 1982, vol. 30, pp. 695-709.

41. U. F. Kocks and G. R. Canova, "How Many Slip Systems, and Which?" Proc. of 2nd Riso International Symposium on Metallurgy and Materials Science, Riso, Denmark, 14-18 September 1981.

42. G. R. Canova, U. F. Kocks, and J. J. Jonas, to be published.

43. G. Y. Chin, W. F. Hosford, and D. R. Mendorf, "Accommodation of Constrained Deformation in f.c.c. Metals by Slip and Twinning," Proc. Roy. Soc., 1969,vol. A309, pp. 433-456.

44. P. van Houtte, "Simulation of the Rolling and Shear Texture of Brass by the Taylor Theory Adapted for Mechanical Twinning," Acta Met., 1978, vol. 26, pp. 591-604.

45. C. S. Barrett, Structure of Metals, 1952, McGraw-Hill, New York and London.

46. W. A. Backofen, "The Torsion Texture of Copper," Trans. AIME, 1950, vol. 188, pp. 1454-1459.

47. R. O. Williams, "Shear Textures in Copper, Brass, Aluminum, Iron and Zirconium," Trans. AIME, 1962, vol. 224, pp. 129-140.

48. P. Regenet and H.-P. Stuwe, "Zur Entstehung von Oberflachentexturen beim Walzen kubisch flachen zentrierter Metalle," Z. Metallkunde, 1963 vol. 54, pp. 273-278.

49. W. Witzel, "Die Endtextur bei de. Scherverformung des Aluminums," Z. Metallkunde, 1973, vol. 64, pp. 813-817.

50. W. A. Backofen and B. B. Hundy, "Torsion Texture of 70-30 Brass and Armco Iron," Trans. AIME, 1953, vol. 197, pp. 61-62.

51. S. C. Shrivastava, J. J. Jonas, and G. R. Canova, "Equivalent Strain in Large Deformation Torsion Testing: Theoretical and Practical Considerations," J. Mech. Phys. Solids, 1982, vol. 30, pp. 75-90.

52. E. Aernoudt and J. Gil-Sevillano, "Influence of the Mode of Deformation on the Hardening of Ferritic and Pearlitic Carbon Steels at Large Stains," J. Iron and Steel Inst., 1973 vol. 211, pp. 718-725.

53. J. Gil-Sevillano and E. Aernoudt, "On the Influence of the Mode of Deformation on the Hardening of Iron at Low Temperature and Large Strains," Met. Trans., 1975, vol. 6A,pp. 2163-2164.

54. C. M. Young, L. J. Anderson, and O. D. Sherby, Reply to "On the Influence of the Mode of Deformation on the Hardening of Iron at Low Temperature and Large Strain," Met. Trans. A, 1975, vol. 6A, pp. 2164-2165.

55. J. Weertman and S. S. Hecker, "Theory for Saturation Stress Difference in Torsion vs. Other Types of Deformation at Low Temperatures," submitted to J. Mech. Mater., 1982.

56. H. Hu, P. R. Sperry, and P. A. Beck, "Rolling Textures in Face-Centered Cubic Metals," Trans. AIME, 1952, vol. 194, pp. 76-81.

57. J. O'Rourke, Los Alamos National Laboratory, Unpublished work.

58. J. S. Kallend and G. J. Davies, "The Prediction of Plastic Anisotropy in Annealed Sheets of Copper and α-Brass," J. Inst. Metals, 1970, vol. 98, pp. 242-244.

59. J. S. Kallend and G. J. Davies, "The Elastic and Plastic Anisotropy of Cold-Rolled Sheets of Copper, Gilding Metal, and α-brass," J. Inst. Metals, 1971, vol. 99, pp. 257-260.

60. H. J. Bunge and W. T. Roberts, "Orientation Distributions, Elastic and Plastic Anisotropy in Stabilized Steel Sheet," J. Appl. Cryst., 1969, vol. 2, pp. 116 .

61. I. L. Dillamore and R. E. Smallman, "The Status of Research on Textures in Metals," Met. Science, 1972, vol. 6, pp. 184-188.

62. S. K. Varma and B. G. LeFevre, "Large Wire Drawing Plastic Deformation in Aluminum and Its Dilute Alloys," Met. Trans. A, 1980, vol. 11A, pp. 935-942.

63. D. J. Lloyd and D. Kenny, "The Structure and Properties of Some Heavily Cold Worked Aluminum Alloys," Prepublication paper from Aluminum Co. of Canada, Ltd. Research Center, Kingston, Ontario, Canada.

64. D. Kalish and B. G. LeFevre, "Subgrain Strengthening of Aluminum Conductor Wires," Met. Trans. A, 1975, vol. 6A, pp. 1319-1324.

65. H. Luthy, A. K. Miller, and O. D. Sherby, "The Stress and Temperature Dependence of Steady-State Flow at Intermediate Temperatures for Pure Polycrystalline Aluminum," Acta. Met., 1980, vol. 28, pp. 169-178.

66. J. H. Cairns, J. Clough, M. A. P. Dewey, and J. Nutting, "The Structue and Mechanical Properties of Heavily Deformed Copper," J. Inst. Met., 1971. vol. 99, pp. 93-97.

67. W. G. Truckner and D. E. Mikkola, "Strengthening of Copper by Dislocation Substructures," Met. Trans. A, 1977, vol 8A, pp. 45-49.

68. F. A. Hodierne, "A Torsior Test for Use in Metalworking Studies," J. Inst. Met., 1963, vol. 91, p 267-273.

69. J. Nuttall and J. Nutting, "Structure and Properties of Heavily Cold-Worked fcc Metals and Alloys," Met. Science, 1978. vol. 12, pp. 430-437.

70. W. H. Zimmer, S. S. Hecker, L. E. Murr, and D. L. Rohr, "Large-Strain Plastic Deformation of Commercially-Pure Nickel," accepted for publication in Met. Science, 1982.

71. U. F. Kocks, "Solution Hardening and Strain Hardening at Elevated Temperatures," this volume.

72. A. A. Ridha and W. B. Hutchinson," Recrystallization Mechanisms and the Origin of Cube Texture in Copper," Acta Met., 1982, vol. 30, pp. 1929-1940.

73. S. Nourbakhsh and J. Nutting, "The High Strain Deformation of an Aluminum-4% Copper Alloy in the Supersaturated and Aged Conditions," Acta Met., 1980. vol. 28, pp. 257-365.

74. R. L. Aghan and J. Nutting, "Structure and Properties of Free-Cutting Steels After Deformation to High Strains, Mets. Tech., 1981. vol. 8, pp. 41-45.

75. J. D. Embury and R. M. Fisher," The Structure and Properties of Drawn Pearlite," Acta. Met., 1966, vol. 14, pp. 147-159.

76. G. Langford and M. Cohen, "Strain Hardening of Iron by Severe Plastic Deformation," Trans. Quarterly, ASM., 1969 vol. 62, pp. 623-638.

77. H. J. Rack and M. Cohen, "Strain Hardening of Iron-Titanium Alloys at Very Large Strains," Mat. Sci. Eng., 1970, vol. 6, pp. 320-326.

78. G. Langford," A Study of the Deformation of Patented Steel Wire," Met. Trans., 1970 vol. 1, pp. 465-477.

79. J. Nutting, Proceedings 8th International Congress on Electron Microscopy, eds. J. V. Sanders and D. J. Goodchild, 1974, vol. 1, p. 580..Canberra, Australian Academy of Science.

80. P. T. Wakufield, A. S. Malin, and M. Hatherly," The Structure and Texture of a Rolled Low Stacking Fault Energy Alloy," J. Aust. Inst. Met., 1977, vol. 22, pp. 143-151.

81. A. S. Malin and M. Hatherly, "Microstructore of Cold-Rolled Copper," Met. Science, 1979. vol. 13, pp. 463-472.

82. M. Hatherly and A. S. Malin,"Deformation of Copper and Low Stacking-Fault Energy, Copper-Base Alloys," Mets. Tech., 1979, vol. , pp. 308-319.

83. P. T. Wakefield and M. Hatherly," Microstructure and Texture of Cold-Rolled Cu-10Zn brass," Met. Science, 1981, vol. 15, pp. 109-115.

84. D. L. Rohr and S. S. Hecker," Three Surface TEM Observations of Cold Rolled 1100 Aluminum," 39th Am. Proc. Electron Microscopy Soc. Amer. Atlanta, Georgia, 1981, ed. G. W. Bailey, pp. 50-51.

85. F. Schuh and M. von Heimendahl, "Die Ausbildung der Versetzungsstruktur in Aluminum und der Beziehungen zum Verformungsverhalten," Z. Metallkunde, 1974, vol. 68, pp. 260-265.

86. K. P. Staudhammer, D. L. Rohr, K. A. Johnson, and S. S. Hecker, Los Alamos National Laboratory, Unpublished work.

87. J. J. Jonas, C. M. Sellars, and W. J. McG. Tegart, "Strength and Structure under Hot-working Conditions," Met. Rev., 1969, vol. 14, pp. 1-24.

88. R. J. McElroy and Z. C. Szkopiak, "Dislocation-Substructure-Strengthening and Mechanical-Thermal Treatment of Metals," Internat. Met. Rev., 1972, vol. 17, pp. 175-202.

89. A. W. Thompson, "Substructure Strengthening Mechanisms," Met. Trans. A, 1977, vol. 8A, pp. 833-842.

90. Z. S. Basinski, A. S. Korbel, and S. J. Basinski,"The Temperature Dependence of the Saturation Stress and Dislocation Substructure in Fatigued Copper Single Crystals," Acta Met., vol. 28, pp. 191-207.

91. S. S. Hecker, "Experimental Studies of Sheet Stretchability," in Formability: Analysis, Modeling, and Experimentation, ed. S. S. Hecker, A. K. Ghosh and H. L Gegel, The Metallurgical Society of AIME, 1978, pp. 150-182.

92. S. S. Hecker, "Sheet Stretching Experiments," in Application of Numerical Methods to Forming Processes, ed. H. Armen, American Soc. Mech. Engng., 1978, AMD-vol. 28, pp. 85-94.

93. A. K. Ghosh and S. S.Hecker, "Failure in Thin Sheets Stretched Over Rigid Punches," Met. Trans. A., 1975, vol. 6A, pp. 1065-1074.

94. M. G. Stout and S. S. Hecker," Role of Geometry in Plastic Instability and Fracture of Tubes and Sheet," submitted to Met. Trans., 1982.

95. J. E. Bird and J. L. Duncan, "Strain Hardening at High Strain in Aluminum Alloys and its Effect on Strain Localization," Met. Trans. A, 1981, vol. 12A, pp. 235-241.

96. L. E. Murr, Interfacial Phenomena in Metals and Alloys, 1975, Addison - Wesley Publishing Co., Reading, MA., pp. 145-148.

Test Technique	Strain Limits	Comments
Direct Tests		
Uniaxial Tension	<0.5	Plastic Instability
	1 to 1.5	Necking Correction
Biaxial Tension		
(Hydraulic Bulge)	<0.8	Plastic Instability
(Tube Testing)	<0.4	Plastic Instability
Compression	<0.7	Barrelling
	3 to 4	Remachining
Torsion		
Thin-walled tubes	<0.2	Buckling
	2 to 5	Very Short Tubes
Round Solid Bars	2 to 5	Limited by Ductility
Indirect Tests		
Wire Drawing + Tension	10	
Strip Drawing + Tension	4	
Rolling + Tension	7	
+ Plane Strain Compression	7	

Table 1. Large strain test techniques and their limitations.

Phenomenological Models:

Holloman (parabolic)..... $\sigma = K\varepsilon^{n}$

Ludwik ..... $\sigma = \sigma_o + K'\varepsilon^{n'}$

Swift ..... $\sigma = K_2(\varepsilon + \varepsilon_o)^{n}2$

Voce ..... $\sigma = \sigma_s-(\sigma_s-\sigma_o)\exp(-N\varepsilon)$

Modified Voce ..... $\sigma = \sigma_s-(\sigma_s-\sigma_c)\exp(-N'\varepsilon^{P})$
(Hockett-Sherby)

Kocks Model ..... $\theta = \theta_o(1 - \frac{\sigma}{\sigma_s})$

where $\theta = \frac{d\sigma}{d\varepsilon}\Big|_{\dot{\varepsilon},\ T}$

TABLE II Stress-strain relations based on empirical (phenomenological) and theoretical (Kocks) considerations. The Voce and Kocks relations predict saturation.

TABLE III. Summary of Substructural Evolution for Several fcc Metals and Alloys

Material	T/T_m	SFE[56] ($ergs/cm^2$)	Low Strains (<0.3)	Moderate Strains (<2.3)	Large Strains (>2.3)
1100 Aluminum	0.32	166	Dislocation tangles, cell network by ε=0.1, dynamic recovery and subgrains above 0.2	Cells and subgrains decrease in size, new ones form, some evidence of microbands in edge-on section	Structure looks very recovered, more subgrains than cells, misorientation between subgrains continues to increase, No edge-on substructure dimensions available. Only occasional microband at ε=2.3.
200 Nickel	0.17	128	Dislocation tangles, cell network by ε=0.1.	Cells decrease in size, definite recovery at ε>1 with distinct subgrain boundaries. Cells and subgrains continue to decrease. Structure looks ribbon like. Some evidence of microbands.	Continued recovery, cells and subgrains continue to decrease in size (edge-on). No evidence of microbands or shear bands.
Copper[82]	0.22	78	Dislocation tangles, cell network by ε=0.1, microbands evident by 0.2.	Microbands along (111), rotate towards rolling plane, new microbands form. Much of deformation appears by microband mechanism. Macro shear bands form at ε>1	Shear bands assume dominant role in deformation, dynamic recovery occurs Hutting and coworkers[66,69] found evidence of dynamic recrystallization at very large (>4) strains.
70-30 Brass[82]	0.2	14	Slip by partials, develop planar dislocation array, followed by microbands.	At strains of 0.5 to 1.3 twinning is major deformation mode observed, twins form and rotate to align with rolling plane, by ε=1.6 most of volume is twinned.	Extensive macro shear banding, especially in twinned areas, subgrains form in shear band areas and again deform by slip.

LIST OF FIGURES

Fig. 8. Comparison of stress-strain curves for 70-30 brass for different deformation modes from Refs. 23 to 26.

Fig. 9. Comparison of stress-strain curves for Fe-0.17% Ti deformed by torsion[19] (solid rod), wire drawing + tension,[27] and strip drawing + plane strain compression.

Fig. 10. Comparison of stress-strain curves for low-carbon steel; plane strain compression on 1008 steel,[28] wire drawing + tension and torsion on 1007 steel.[16,26]

Fig. 11. Construction of a flow curve from rolling prestrain followed by uniaxial tension (R + T). The rolling thickness reduction is converted to an effective von Mises strain.

Fig. 12. Comparison of stress-strain curves for monotonic plane strain compression with rolling prestrain followed by plane strain compression (1008 steel[28]).

Fig. 13. Comparison of stress-strain curves for 70-30 brass determined by rolling + tension and rolling + plane strain compression. Curves are only schematic because original reference by Sundberg et al.[29] contains no units on stress or strain.

Fig. 14. Path change experiments on 70-30 brass. COMP and TOR curves represent continuous flow curves from Fig. 5. Additional curves (a) through (d) represent axial tension on thin-walled tubes following torsional prestrain to von Mises strains indicated.

Fig. 15. Path change experiment on 1100 aluminum. COMP and TOR curves represents continuous flow curves from Fig. 3. The additional curve represents axial compression following prestrain in torsion.

Fig. 16. Stress-strain curves for 1100 aluminum in unidirectional vs multidirectional compression.[15] The dotted curve represents an extension of uniaxial compression data on the basis of a modified Hockett-

Sherby Voce equation.[14] The dashed curves represent changes in deformation mode from unidirectional to multidirectional and vice versa.

Fig. 17. Calculations of the evolution of average Taylor factors with strain using the Bishop and Hill formalism (Gil Sevillano et al.[26,39]). a) Tension and compression. b) Shear.

Fig. 18. a) Crystallographic effective stress-strain comparison for ETP copper data of Gil Sevillano.[16] Solid curves labelled WD + T and TOR are von Mises flow curves from Fig. 4a. Dashed curve labelled TOR represents the crystallographic effective stress-strain curve using the evolving Taylor factors of Fig. 17. Circles represent the Taylor-type correction using the method of relaxed constraints (Canova et al.[42]) for torsion. The Taylor factors were reported by Jonas et al.[35] for this method.

b) Crystallographic effective stress-strain comparison for OFHC copper. Torsional flow curve based on von Mises criterion is shown as curve #1. Curve #4 represents the same data based on the crystallographic Taylor-type criterion based on Taylor factors of Fig. 17. Circles again represent the predictions of the method of relaxed constraints. Curves #2 and #3 represent the compression curves shown in Fig. 4b.

Fig 19. Crystallographic effective stress-strain comparison for 1100 aluminum. Curve #1 represents the von Mises torsion curve and Curve #3 the crystallographic torsion curve (based on the Taylor factors of Fig. 17). Curve #2 represents uniaxial compression for comparison.

Fig. 20. Crystallographic effective stress-strain comparison for 70-30 brass. Curve #1 represents the von Mises torsion curve and Curve #3 the crystallographic torsion curve (based on the Taylor factors of Fig. 17). Curve #2 represents uniaxial compression for comparison.

Fig. 21. a) Partial (111) pole figures for a 70-30 brass tube prestrained to a shear strain of 2.4 (see Fig. 14 for flow curves). Ideal orientations are indicated as follows: Open triangle, (112) [11$\bar{1}$], solid triangle, (111) [11$\bar{2}$].

b) On quadrant of (111) pole figure for a 70-30 brass rod twisted to a shear strain of 3.2.[50] Ideal orientations are indicated as follows: Open triangle, (11$\bar{1}$) [112], solid triangle, (112) [11$\bar{1}$], and double triangle (110) [001].

Fig. 22. Ultimate tensile strength in tension subsequent to rolling prestrain (shown here as true thickness strain) for 1100 aluminum. Circles represent tensile specimens oriented parallel to direction of rolling and crosses transverse. The flow curve represents the best fit through all of the data.

Fig. 23. 1100 aluminum rolled at room temperature to a true thickness strain of a) 1.8 and b) 4.09. Both figures represent partial (111) pole figures. Ideal orientations are designated by open triangle, (113) [33$\bar{2}$] and closed triangle, (225) [55$\bar{4}$].

Fig. 24. (111) pole figure for 95 per cent rolled (true thickness strain of 3) 1100 aluminum from Hu et al.[56] Positions for (111) poles for ideal orientations are indicated by open triangle for (123) [1$\bar{2}$1], solid triangel for (110) [1$\bar{1}$2], and half-filled triangle for (112) [11$\bar{1}$]. Intensities are given in arbitrary units.

Fig. 25. Von Mises effective stress-strain curves for aluminum of different purities and several dilute alloys.[62-65] WD + T denotes wire drawing followed by tension; R + T, rolling plus tension; and TOR, torsion.

Fig. 26. Von Mises effective stress-strain curves for copper of different purities.[66-69] C denotes compression.

Fig. 27. Von Mises effective stress-strain curves for a number of fcc metals of commercial purity.[66,69,70] All curves are for rolling + tension.

Fig. 28. Transmission electron micrographs of cold-rolled 1100 aluminum taken through the sheet surface for different strain levels. (a) 0.11, (b) 0.28, (c) 0.71, (d) 1.49, (e) 4.07, and (f) 6.2.

Fig. 29. TEM measurements of substructure dimensions on cold-rolled 1100 aluminum. (a) Measurements for dislocation cells and (b) subgrains showing distinct boundary contrast. d_l represents the substructure dimension in the rolling direction, d_t in the transverse direction, and d_n in the through-thickness (normal) direction. $d = d_i \exp^{\varepsilon}$ represents the imposed shape change on some initial diameter, d_i.

Fig. 30. Edge-on TEM micrographs of 1100 aluminum cold rolled to a true thickness strain of 1. Micron markers are in the rolling direction for the two different magnifications shown. Note the microbands at $\sim 35°$ to the ribbon-shaped subgrains aligned in rolling direction.

Fig. 31. Edge-on TEM micrographs of 1100 aluminum cold rolled to a true thickness strain of 2.3. (a) Bright field/dark field pair edge-on along rolling direction.

(b) Bright field/dark field pair edge-on transverse to rolling direction.

Fig. 32. TEM measurements of substructure dimensions on cold-rolled 200 nickel. (a) Measurements for dislocation cells and (b) subgrains. d_l represents substructure dimension in the rolling direction, d_t in the transverse direction, and d_n in the through-thickness (normal) direction.

Fig. 33. Bright field/dark field pair of TEM micrographs on cold-rolled 200 nickel (true thickness strain of 5.14) taken edge-on. Rolling direction is in the direction of the micron marke..

Fig. 34. The potential role of grain and substructure sizes in controlling the flow stress. The dashed diagonal line represents the imposed decrease in transverse grain size by the external shape changes due to rolling. The solid curve for cells and subgrains is schematic.

Fig. 35. TEM micrograph of 18% cold rolled copper from Malin and Hatherly.[82] Beam direction approximately $[\bar{1}\bar{1}0]$; diffraction vector (g), $[1\bar{1}\bar{1}]$.

Fig. 36. Residual elongation in tension following rolling prestrain for 1100 aluminum. (a) Sheets rolled to a final thickness of 0.635 mm. RD refers to specimen in rolling direction and TD in transverse direction.
(b) Sheets rolled to a final thickness of 0.127 mm. RD and TD results are averaged.

Fig. 37. Residual elongation in tension following rolling prestrain for 200 nickel.

Fig. 38. Stress-strain curve and hardening rate (θ) for 1100 aluminum. Dashed curve labelled T represents uniaxial tension on annealed material. The curve at true thickness strain of 2.3 represents tension following a prestrain of 2.3.

Fig. 39. Enlargement of Fig. 38 near the prestrain level of 2.3. Subscript R refers to rolling curve and t to subsequent tension. The solid σ_t curve represents the engineering stress-strain curve. True stress-strain behavior is labelled True σ.

Fig. 40. Failure limit curves of 1100 aluminum for annealed and cold-rolled conditions. Failure is defined by local necking. Sheet thickness is 0.635 mm. (Reference 92).

Fig. 41. Failure limit curves of three materials from Refs. 91 and 92. Failure is defined by local necking.

Fig. 42. Hardening rate normalized by stress as a function of strain for hydraulic bulge tests from Bird and Duncan.[95]

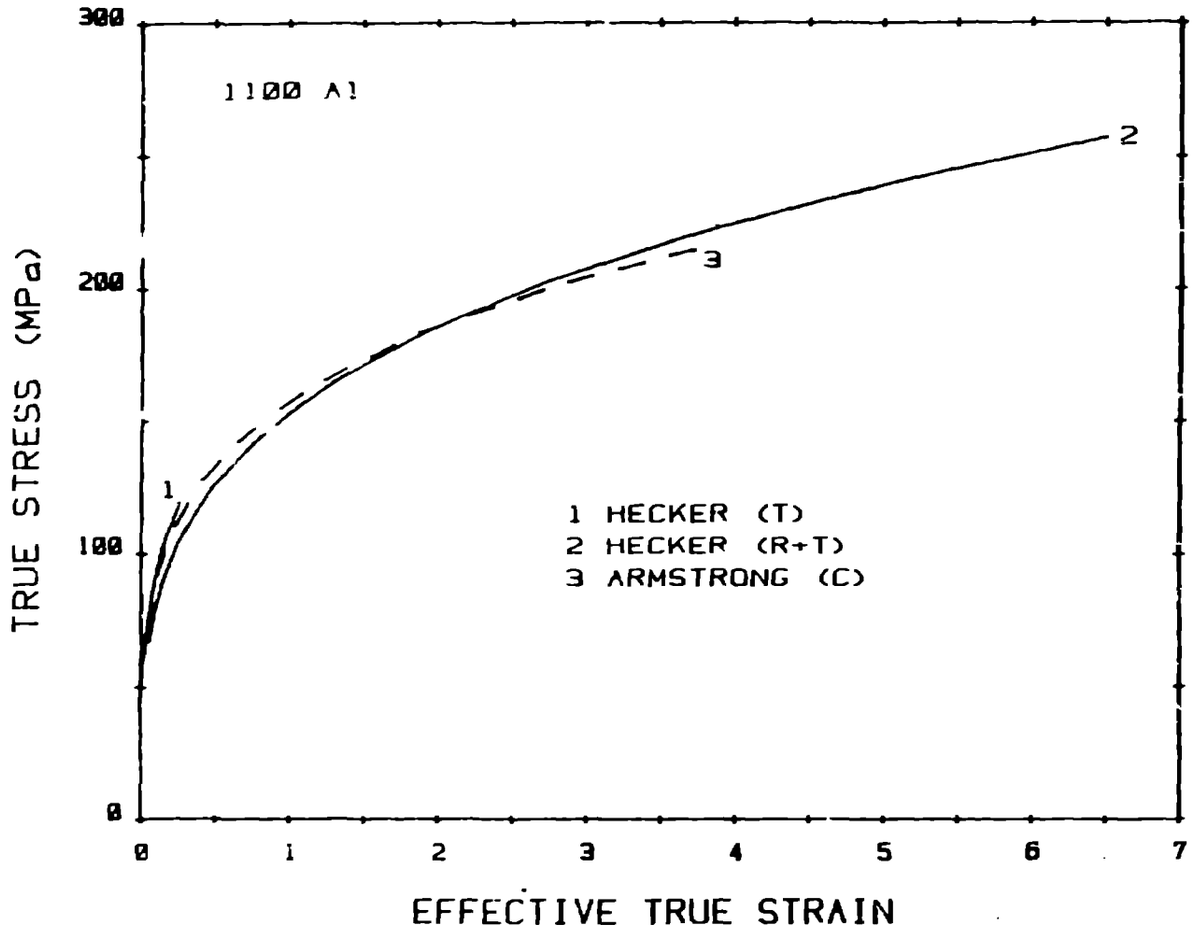
1100 Al
TRUE STRESS (MPa)
300
200
100
0
0
1
2
3
4
5
6
7
EFFECTIVE TRUE STRAIN
1 HECKER (T)
2 HECKER (R+T)
3 ARMSTRONG (C)
1
2
3

Figure 1

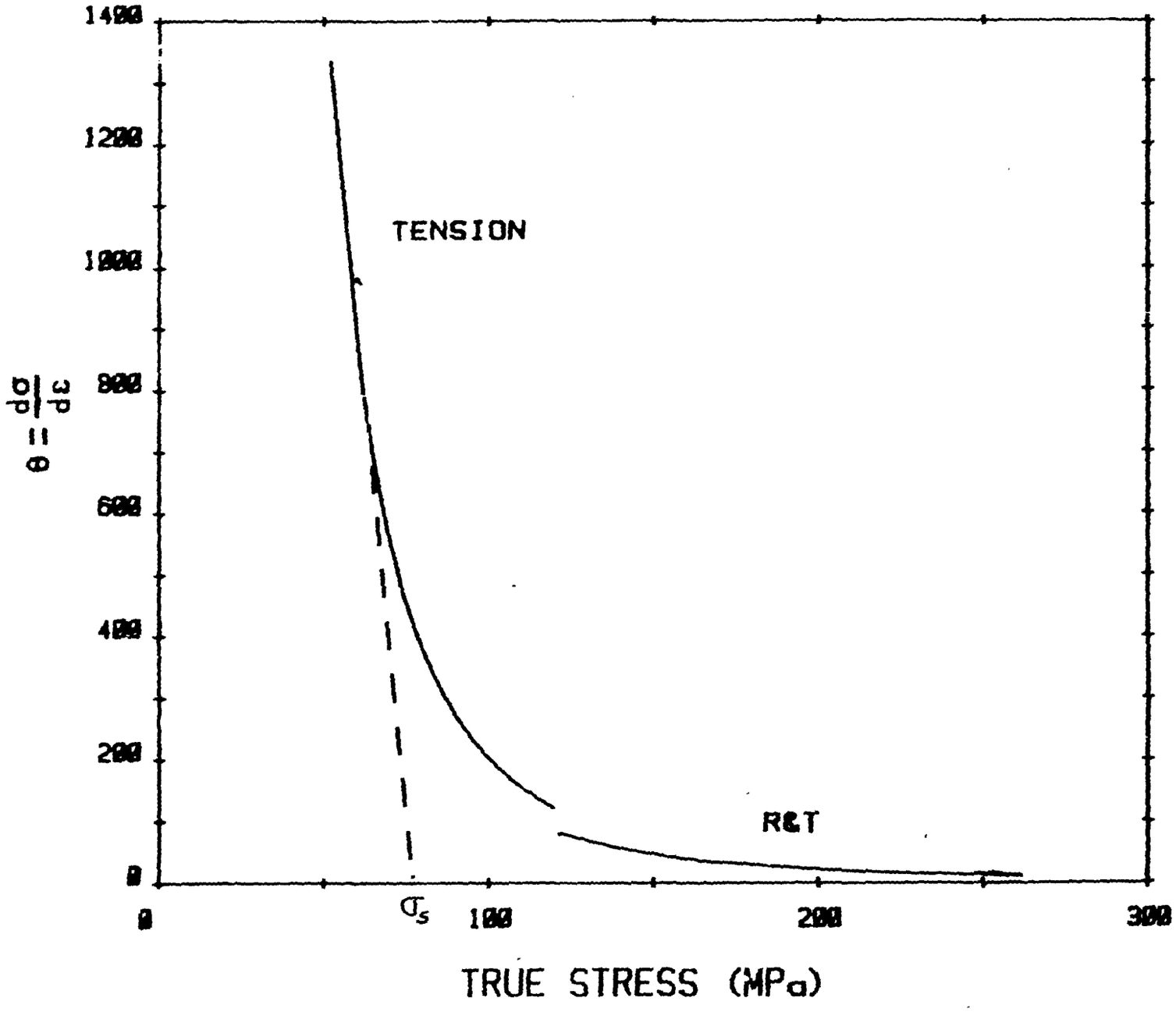
1400
1200
1000
800
600
400
200
0
$\theta = \frac{d\sigma}{d\varepsilon_p}$
TENSION
R&T
0
σ_s
100
200
300
TRUE STRESS (MPa)

Figure 2

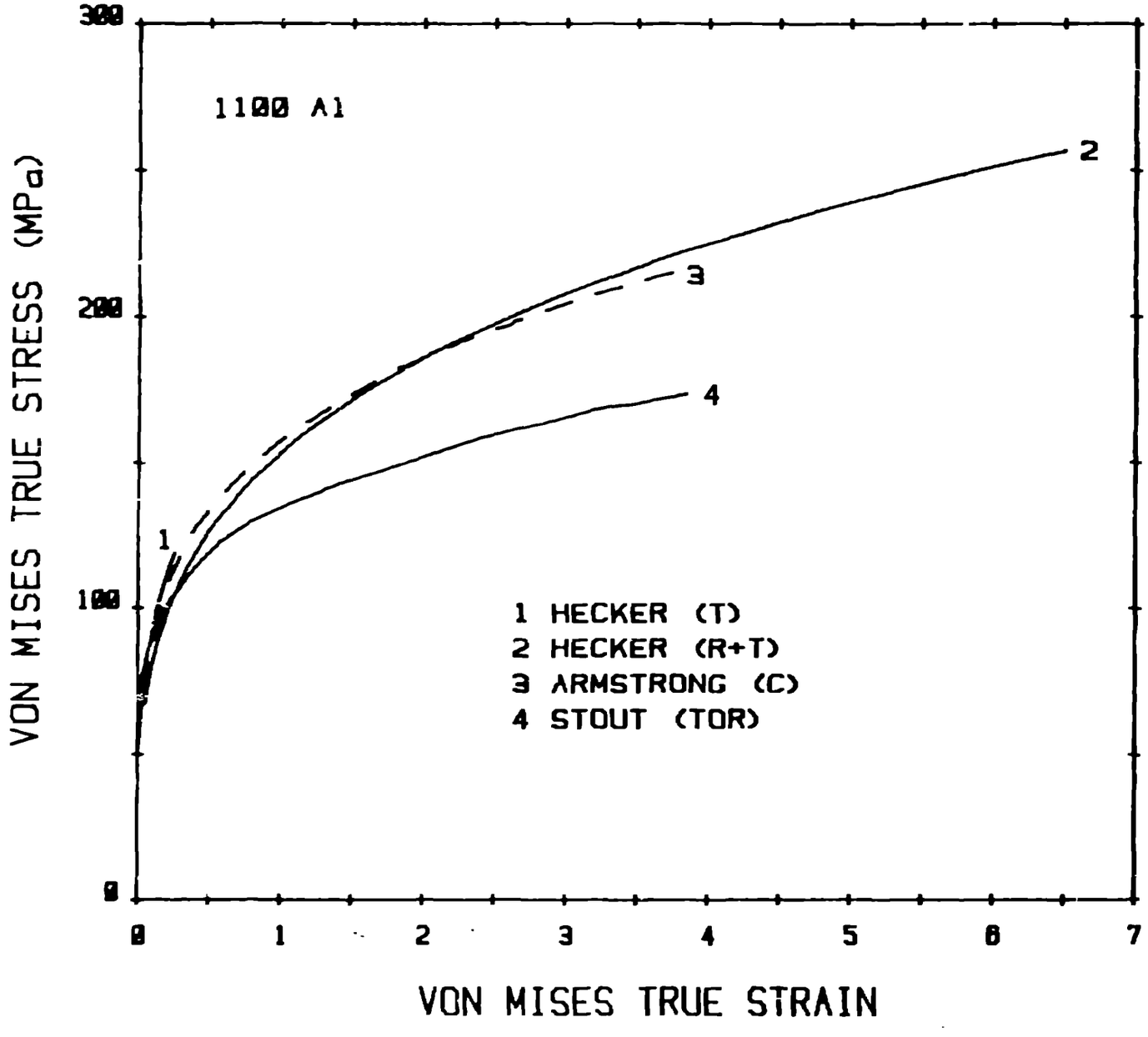
1100 A1
VON MISES TRUE STRESS (MPa)
VON MISES TRUE STRAIN
300
200
100
0
0
1
2
3
4
5
6
7
1
2
3
4
1 HECKER (T)
2 HECKER (R+T)
3 ARMSTRONG (C)
4 STOUT (TOR)

Figure 1

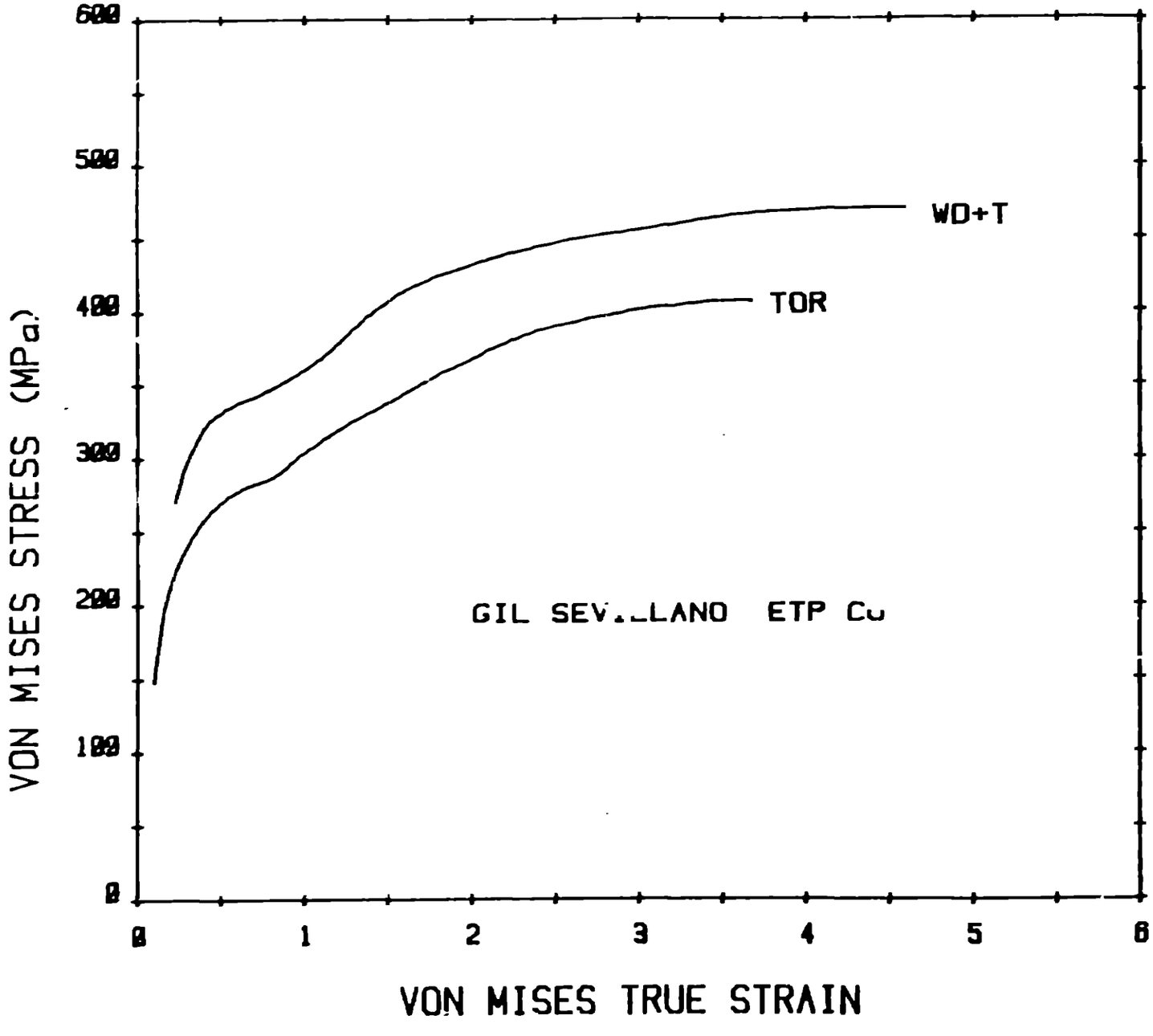
600
500
400
300
200
100
0
0
1
2
3
4
5
6
VON MISES STRESS (MPa)
VON MISES TRUE STRAIN
WD+T
TOR
GIL SEV..LAND ETP Co

Figure 4a

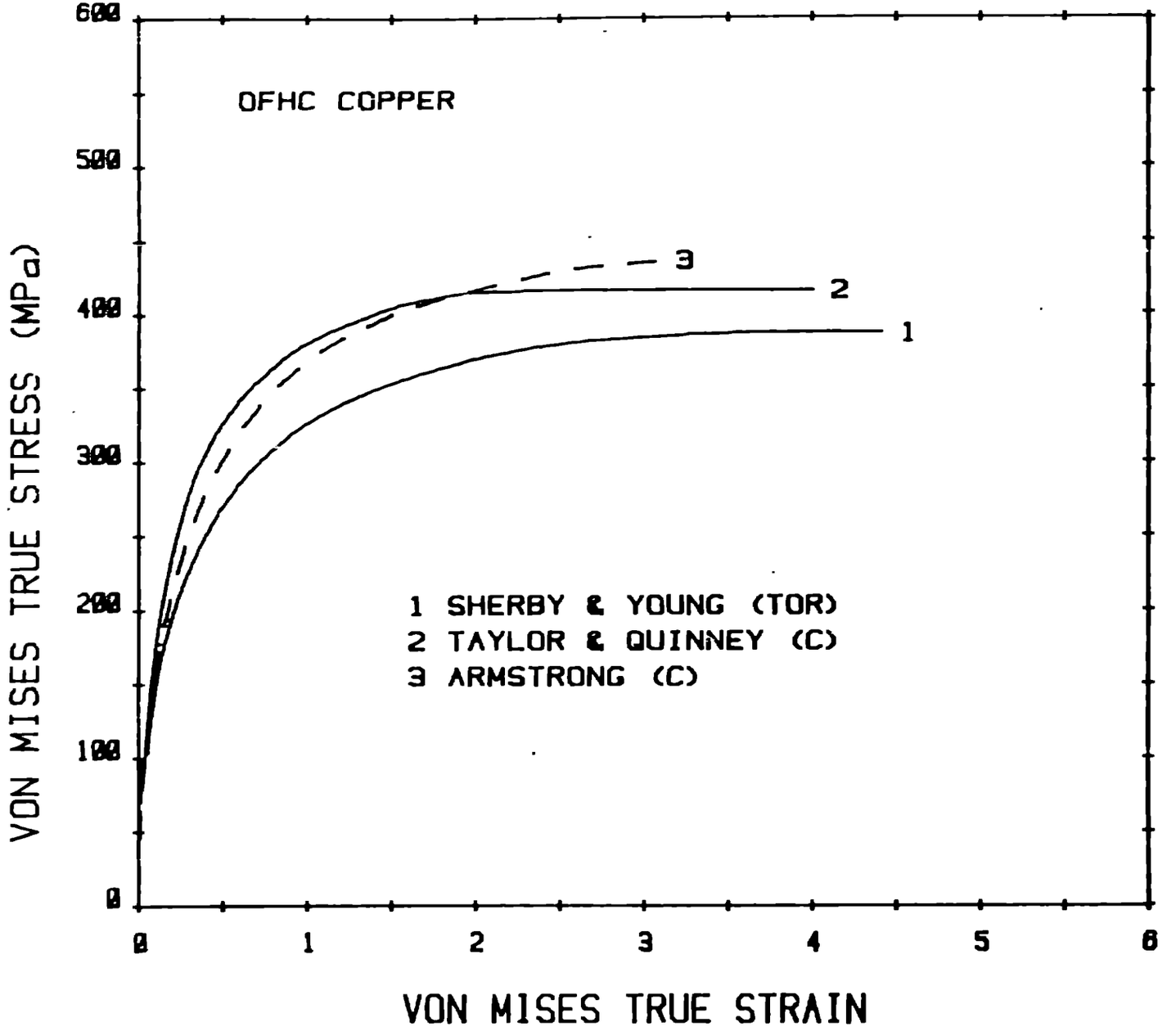
OFHC COPPER
VON MISES TRUE STRESS (MPa)
VON MISES TRUE STRAIN
600
500
400
300
200
100
0
0
1
2
3
4
5
6
1
2
3
1 SHERBY & YOUNG (TOR)
2 TAYLOR & QUINNEY (C)
3 ARMSTRONG (C)

Figure 4b

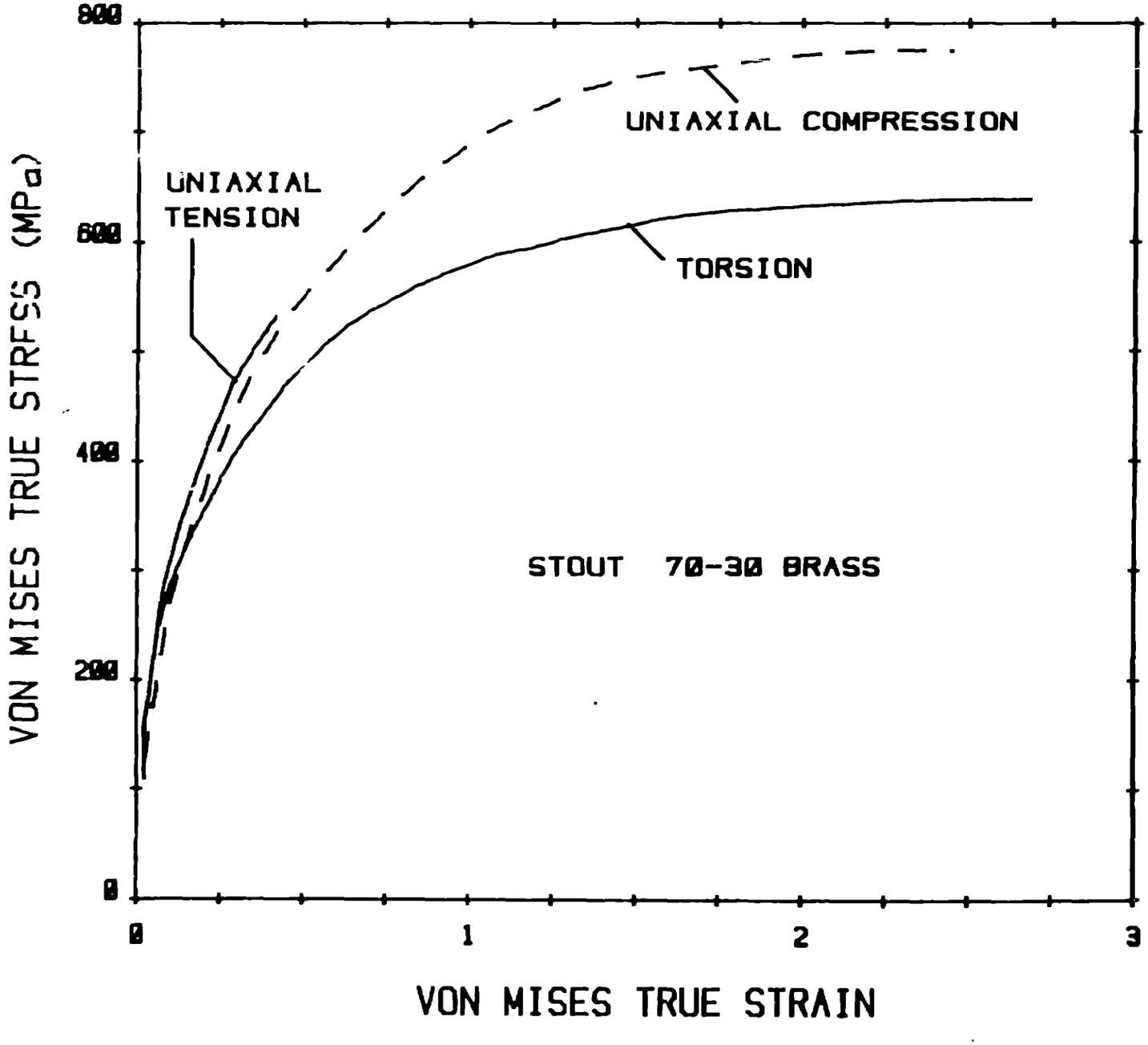
VON MISES TRUE STRESS (MPa)
800
600
400
200
0
UNIAXIAL COMPRESSION
UNIAXIAL TENSION
TORSION
STOUT 70-30 BRASS
0
1
2
3
VON MISES TRUE STRAIN

Figure 3

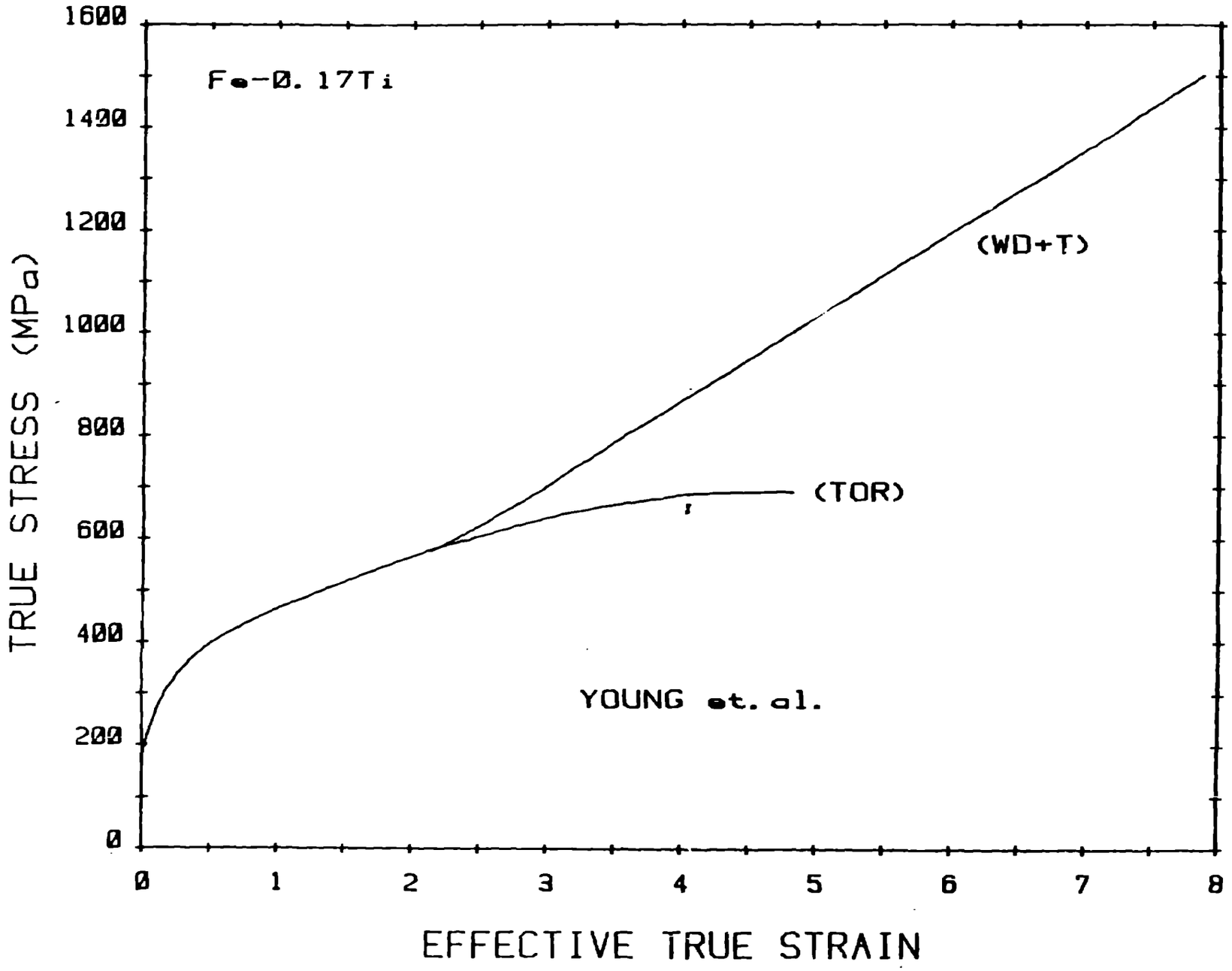
Fe-0.17Ti
(WD+T)
(TOR)
YOUNG et. al.
TRUE STRESS (MPa)
EFFECTIVE TRUE STRAIN
1600
1400
1200
1000
800
600
400
200
0
0
1
2
3
4
5
6
7
8

Figure 6

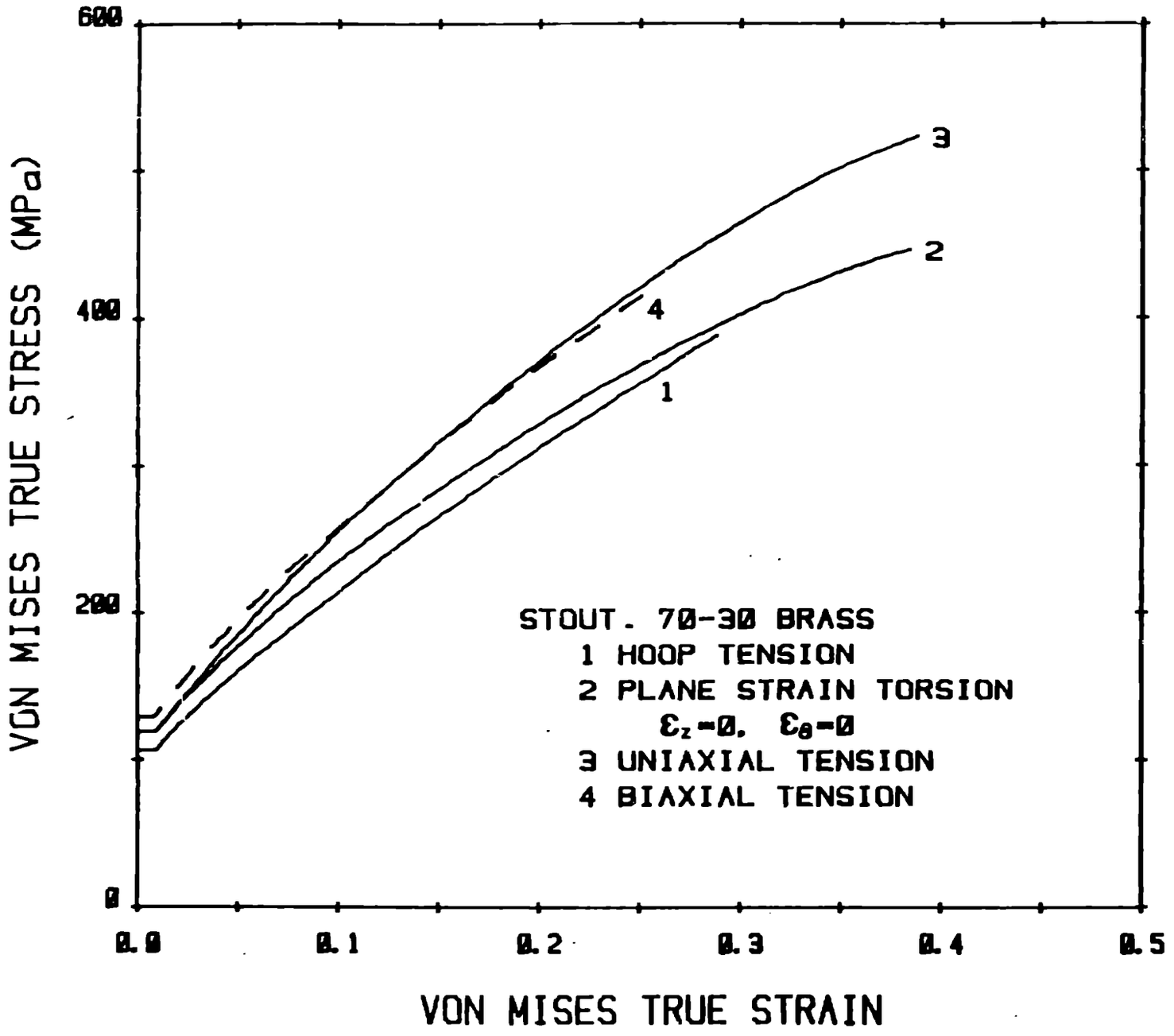
600
400
200
0
VON MISES TRUE STRESS (MPa)
0.0
0.1
0.2
0.3
0.4
0.5
VON MISES TRUE STRAIN
3
2
4
1
STOUT. 70-30 BRASS
1 HOOP TENSION
2 PLANE STRAIN TORSION
$\varepsilon_z=0$. $\varepsilon_\theta=0$
3 UNIAXIAL TENSION
4 BIAXIAL TENSION

Figure 7

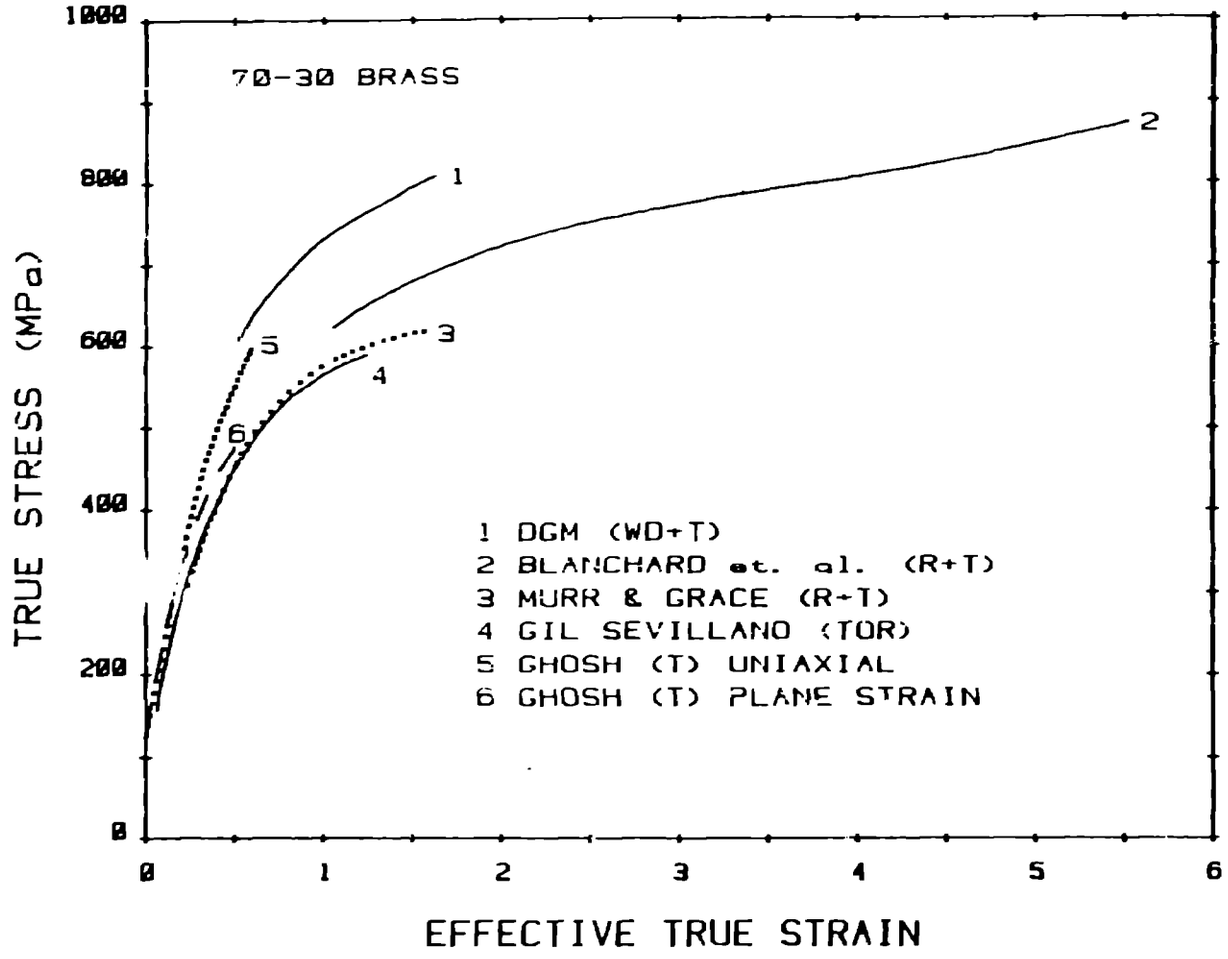
70-30 BRASS
TRUE STRESS (MPa)
EFFECTIVE TRUE STRAIN
1000
800
600
400
200
0
0
1
2
3
4
5
6
1 DGM (WD+T)
2 BLANCHARD et. al. (R+T)
3 MURR & GRACE (R+T)
4 GIL SEVILLANO (TOR)
5 GHOSH (T) UNIAXIAL
6 GHOSH (T) PLANE STRAIN

Figure 8

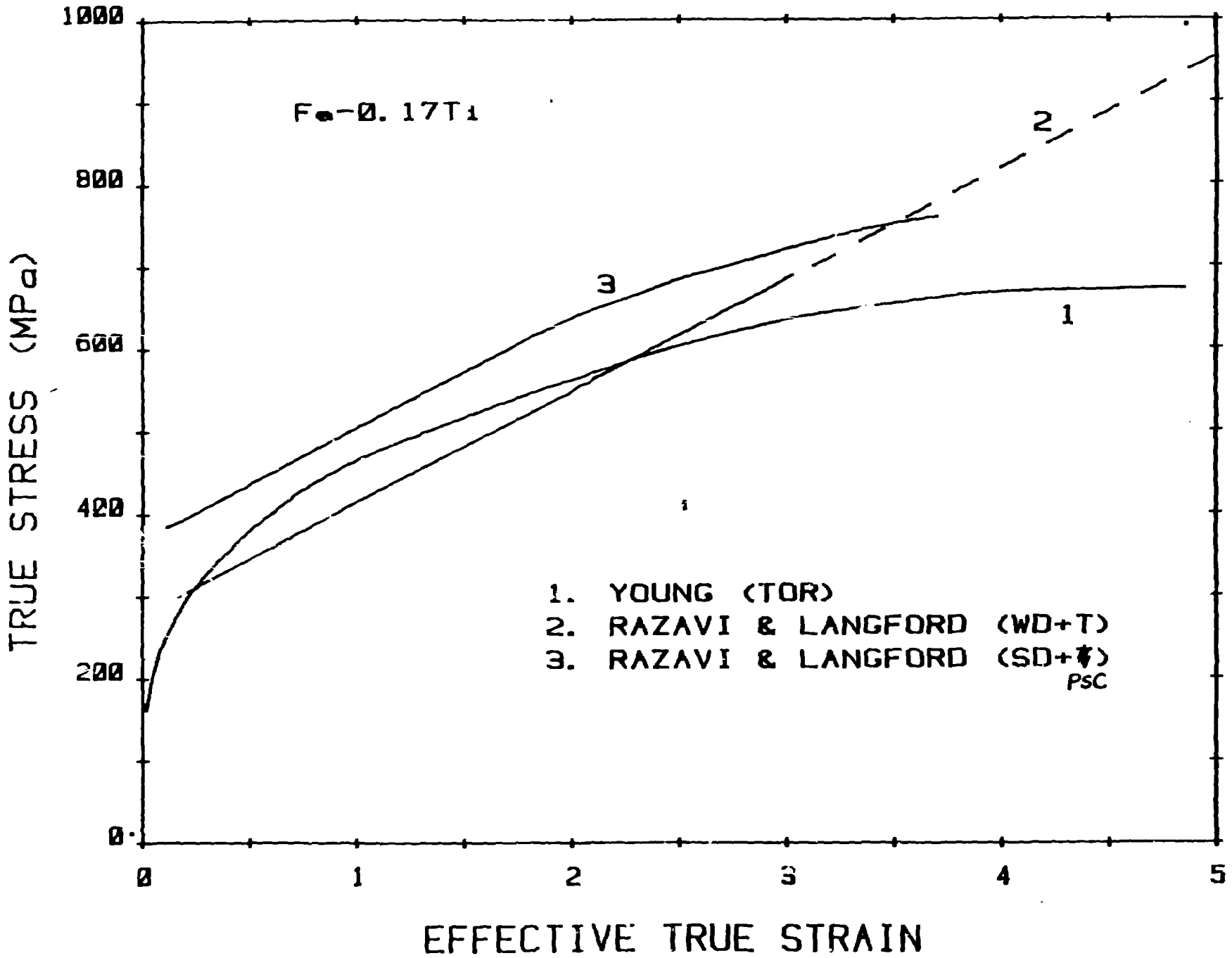
Fe-0.17Ti
1000
800
600
400
200
0
TRUE STRESS (MPa)
0
1
2
3
4
5
EFFECTIVE TRUE STRAIN
1
2
3
1. YOUNG (TOR)
2. RAZAVI & LANGFORD (WD+T)
3. RAZAVI & LANGFORD (SD+T)
PSC

Figure 3

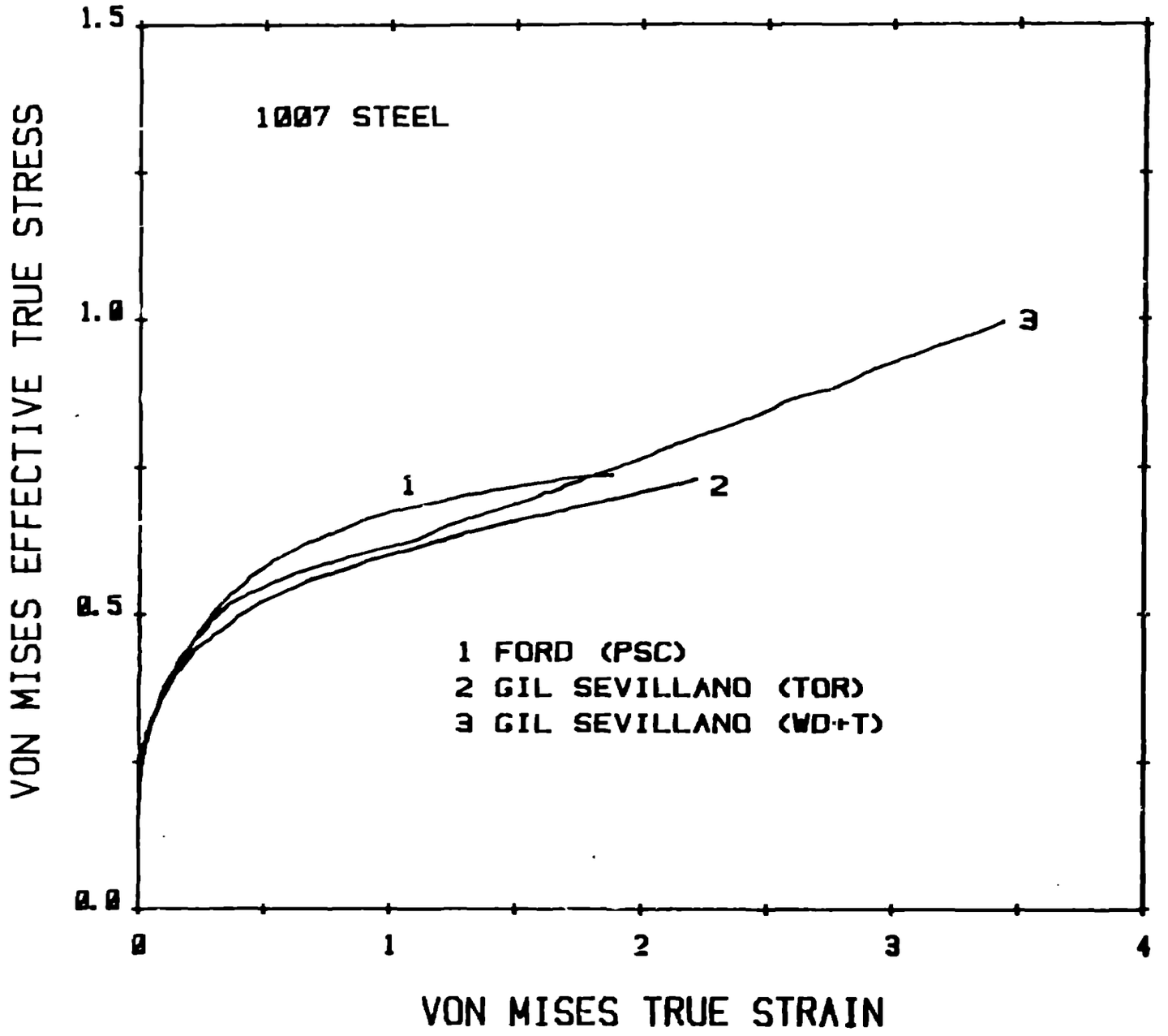
1.5
1.0
0.5
0.0
1007 STEEL
1
2
3
1 FORD (PSC)
2 GIL SEVILLANO (TOR)
3 GIL SEVILLANO (WD+T)
VON MISES EFFECTIVE TRUE STRESS
0
1
2
3
4
VON MISES TRUE STRAIN

Figure 10

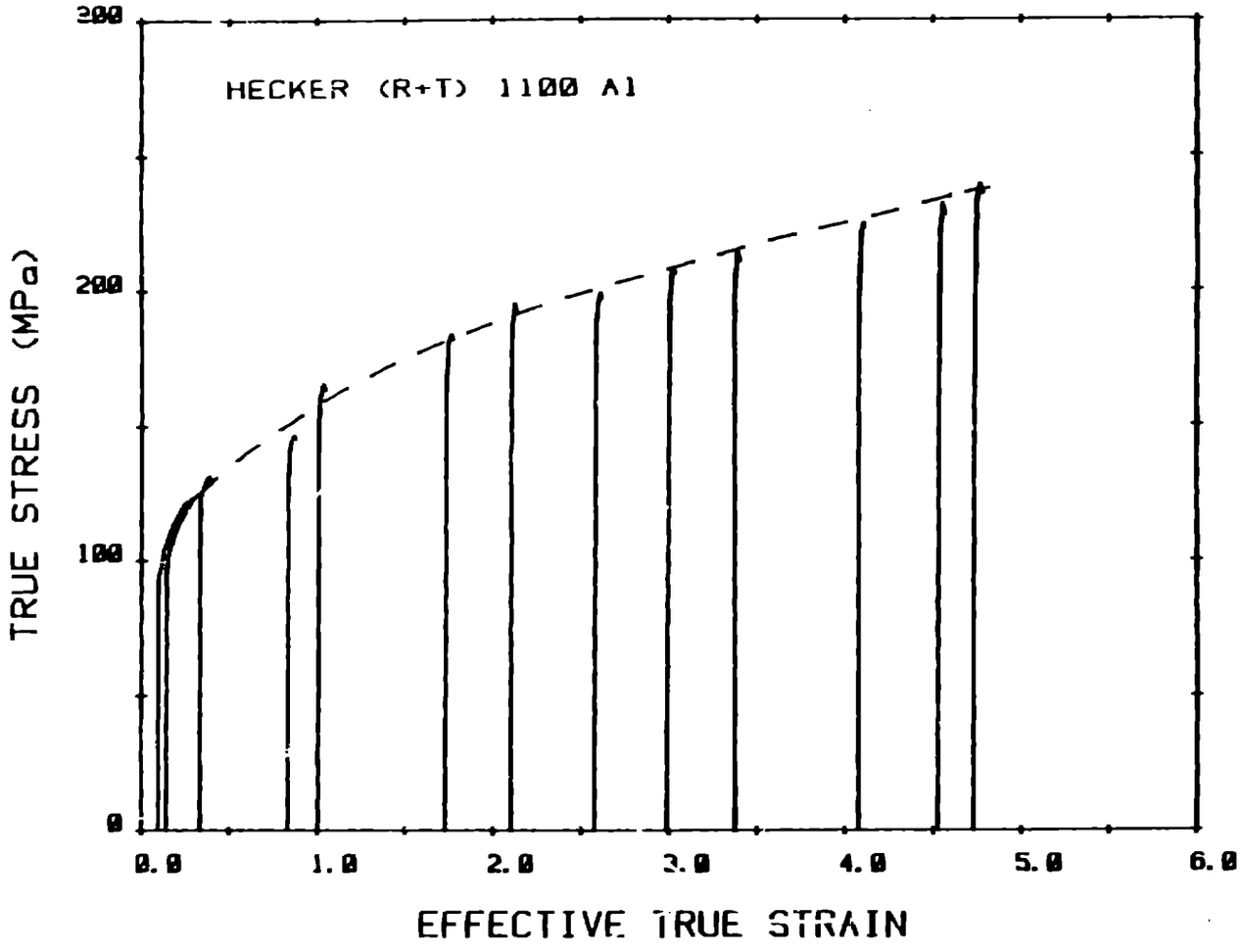
HECKER (R+T) 1100 Al
TRUE STRESS (MPa)
300
200
100
0
0.0
1.0
2.0
3.0
4.0
5.0
6.0
EFFECTIVE TRUE STRAIN

Figure 11

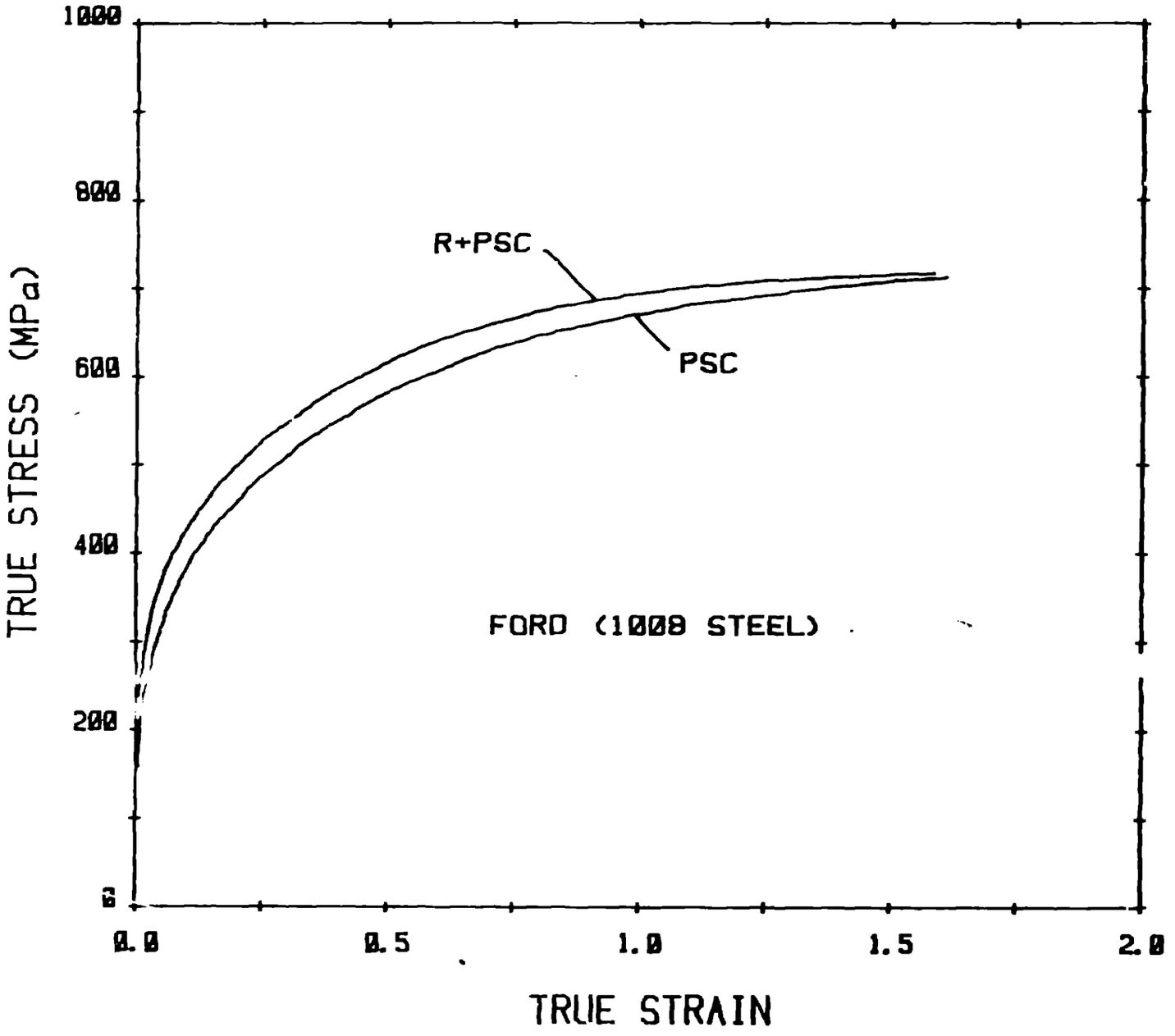
1000
800
600
400
200
0
TRUE STRESS (MPa)
R+PSC
PSC
FORD (1008 STEEL)
0.0
0.5
1.0
1.5
2.0
TRUE STRAIN

Figure 12

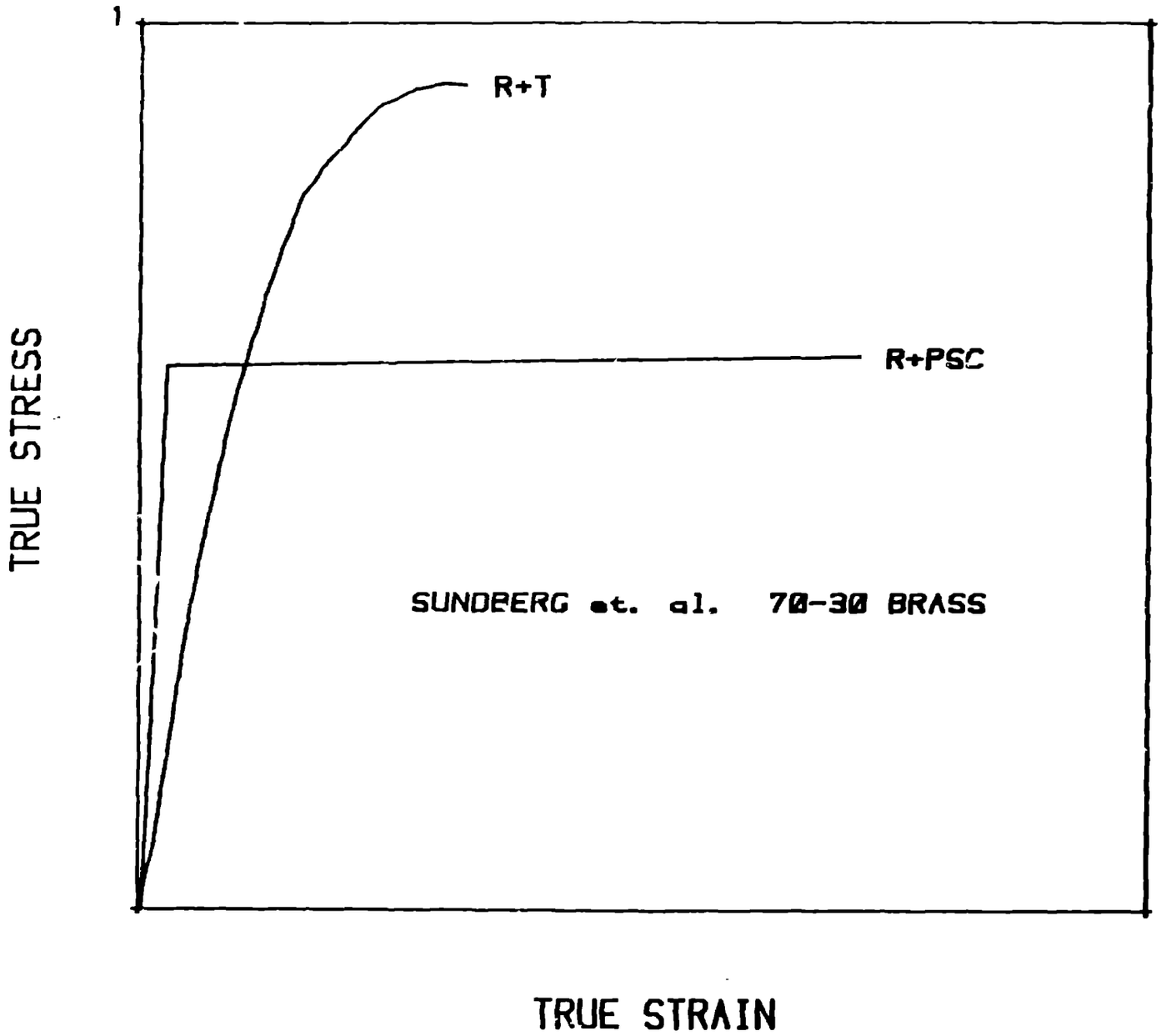

Figure 13

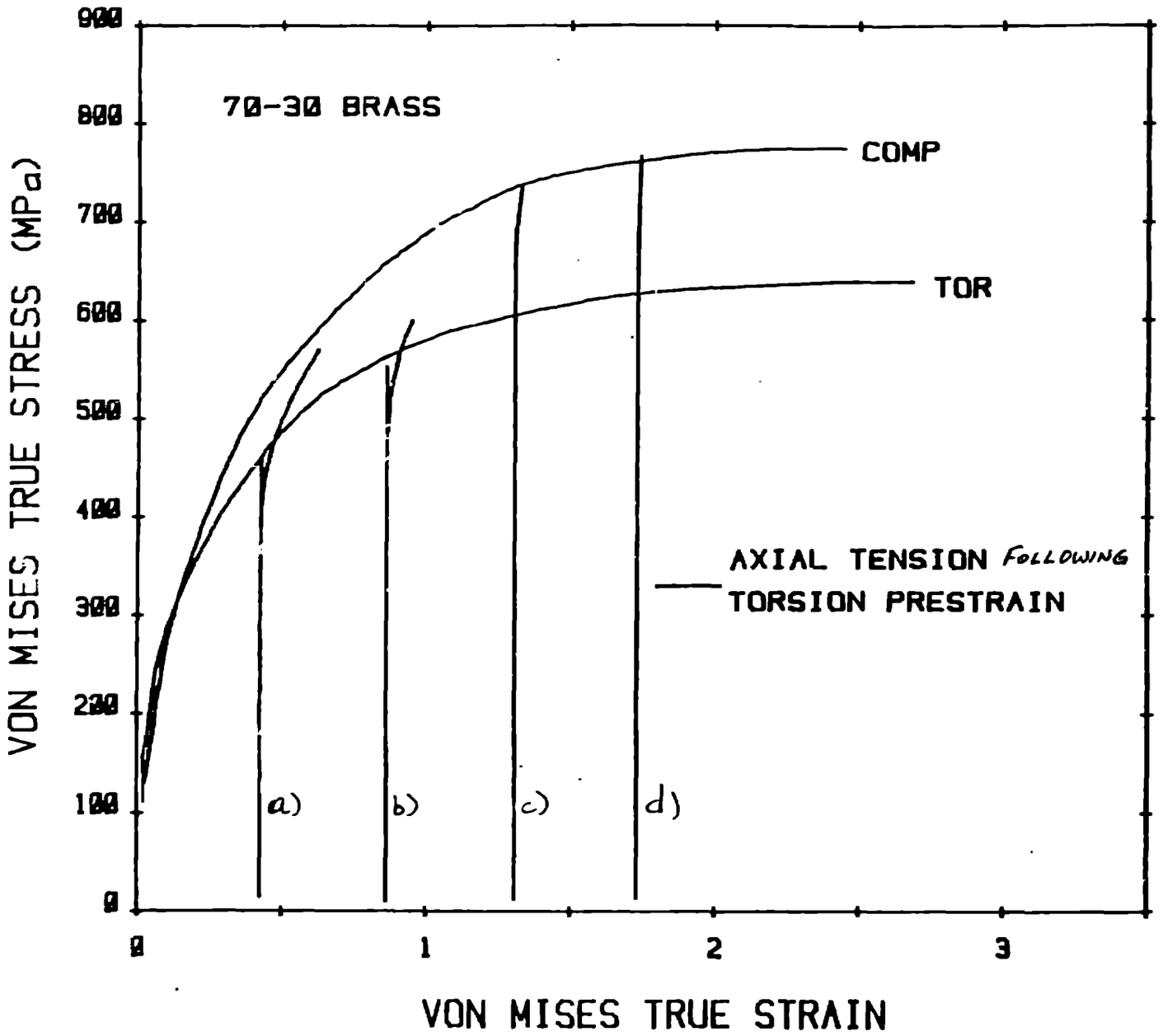
900
800
700
600
500
400
300
200
100
0
0
1
2
3
70-30 BRASS
COMP
TOR
AXIAL TENSION FOLLOWING
TORSION PRESTRAIN
a)
b)
c)
d)
VON MISES TRUE STRESS (MPa)
VON MISES TRUE STRAIN

Figure

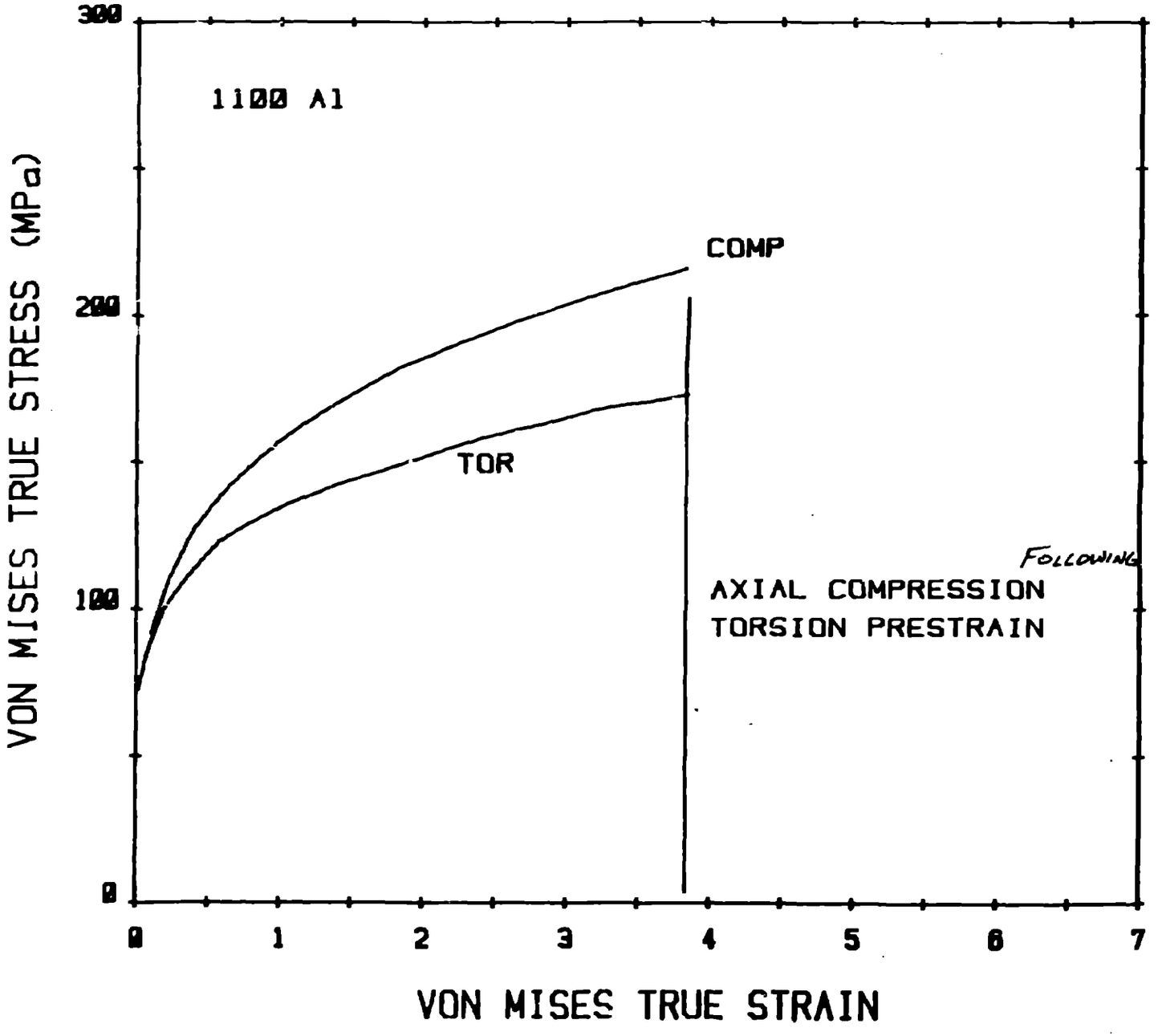
1100 A1
COMP
TOR
FOLLOWING
AXIAL COMPRESSION
TORSION PRESTRAIN
VON MISES TRUE STRESS (MPa)
VON MISES TRUE STRAIN
300
200
100
0
0
1
2
3
4
5
6
7

Figure 13

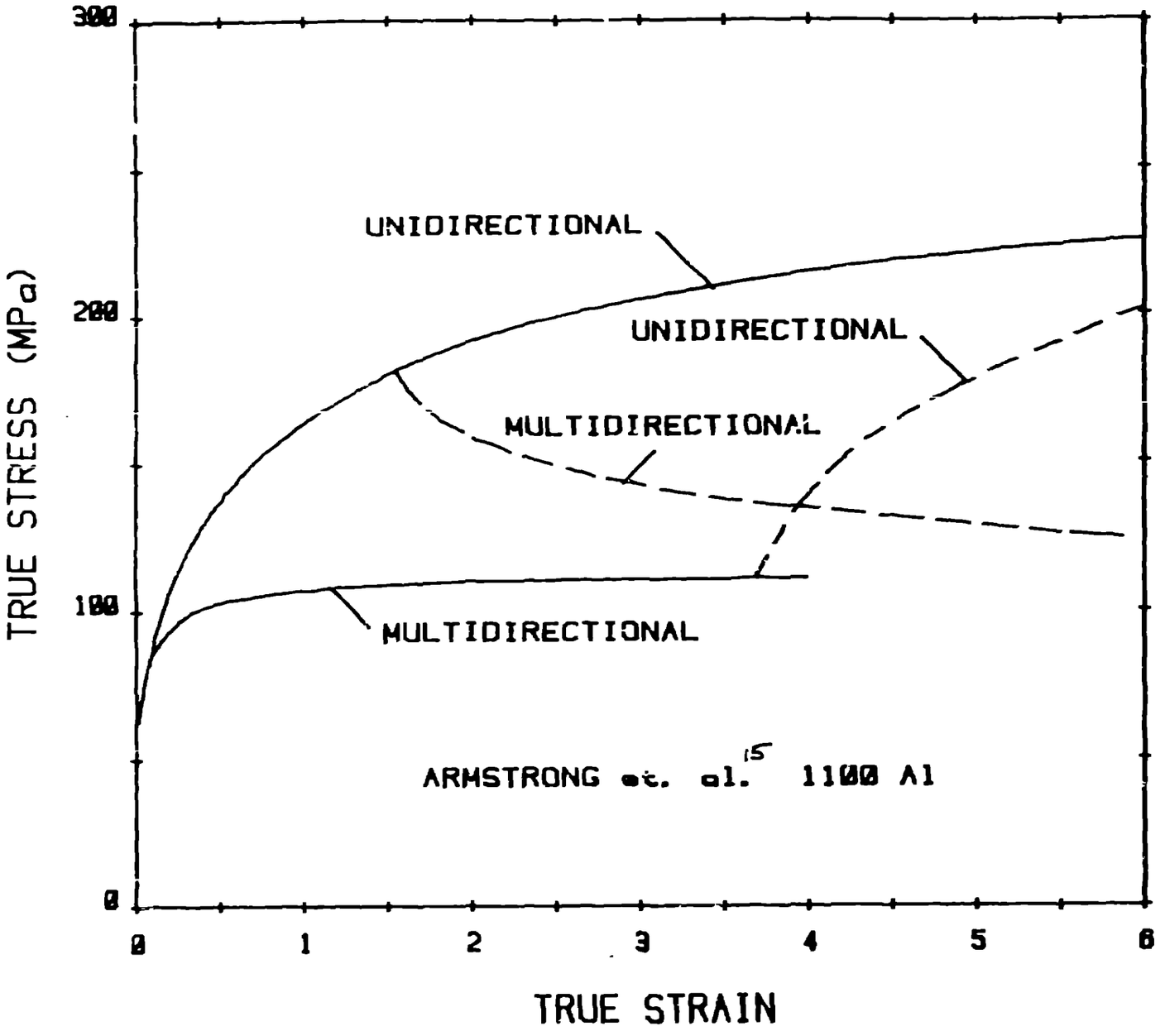
300
200
100
0
TRUE STRESS (MPa)
UNIDIRECTIONAL
UNIDIRECTIONAL
MULTIDIRECTIONAL
MULTIDIRECTIONAL
ARMSTRONG et. al.[15] 1100 Al
0
1
2
3
4
5
6
TRUE STRAIN

Figure 11

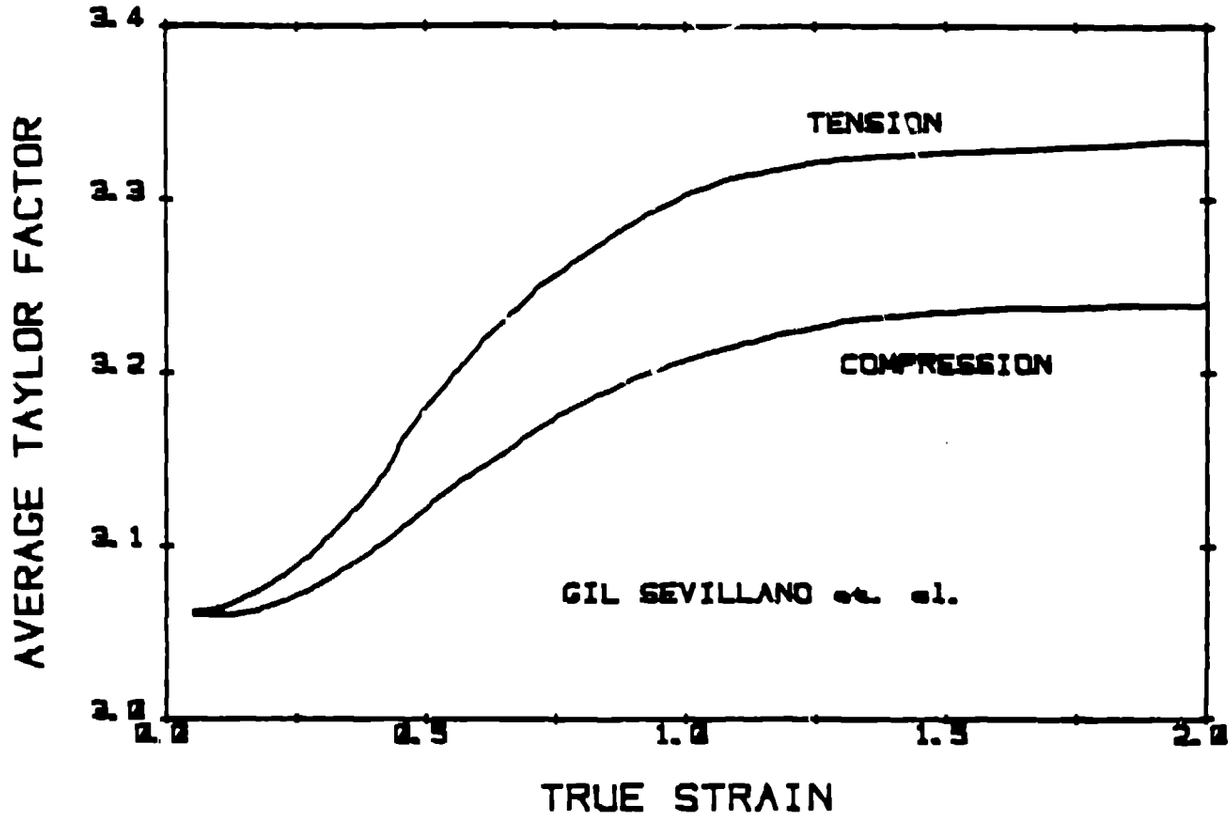
AVERAGE TAYLOR FACTOR
3.4
3.3
3.2
3.1
3.0
0.0
0.5
1.0
1.5
2.0
TENSION
COMPRESSION
GIL SEVILLANO et. al.
TRUE STRAIN

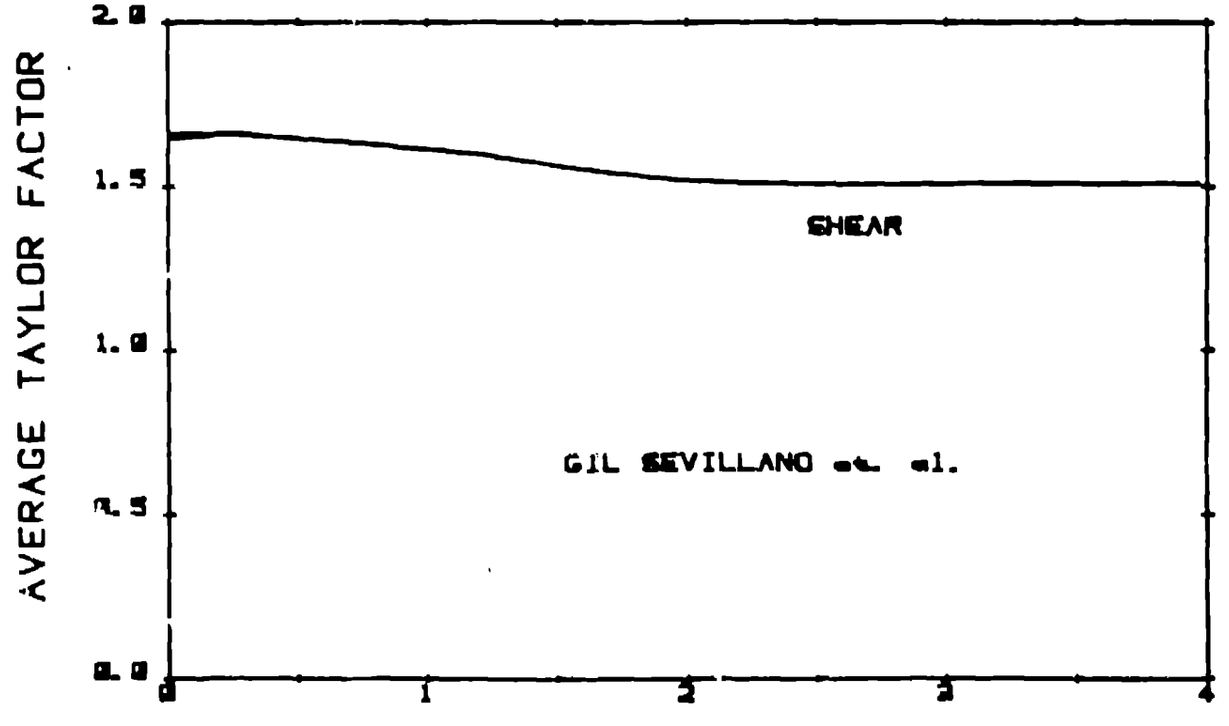
AVERAGE TAYLOR FACTOR
2.0
1.5
1.0
0.5
0.0
0
1
2
3
4
SHEAR
GIL SEVILLANO et. al.

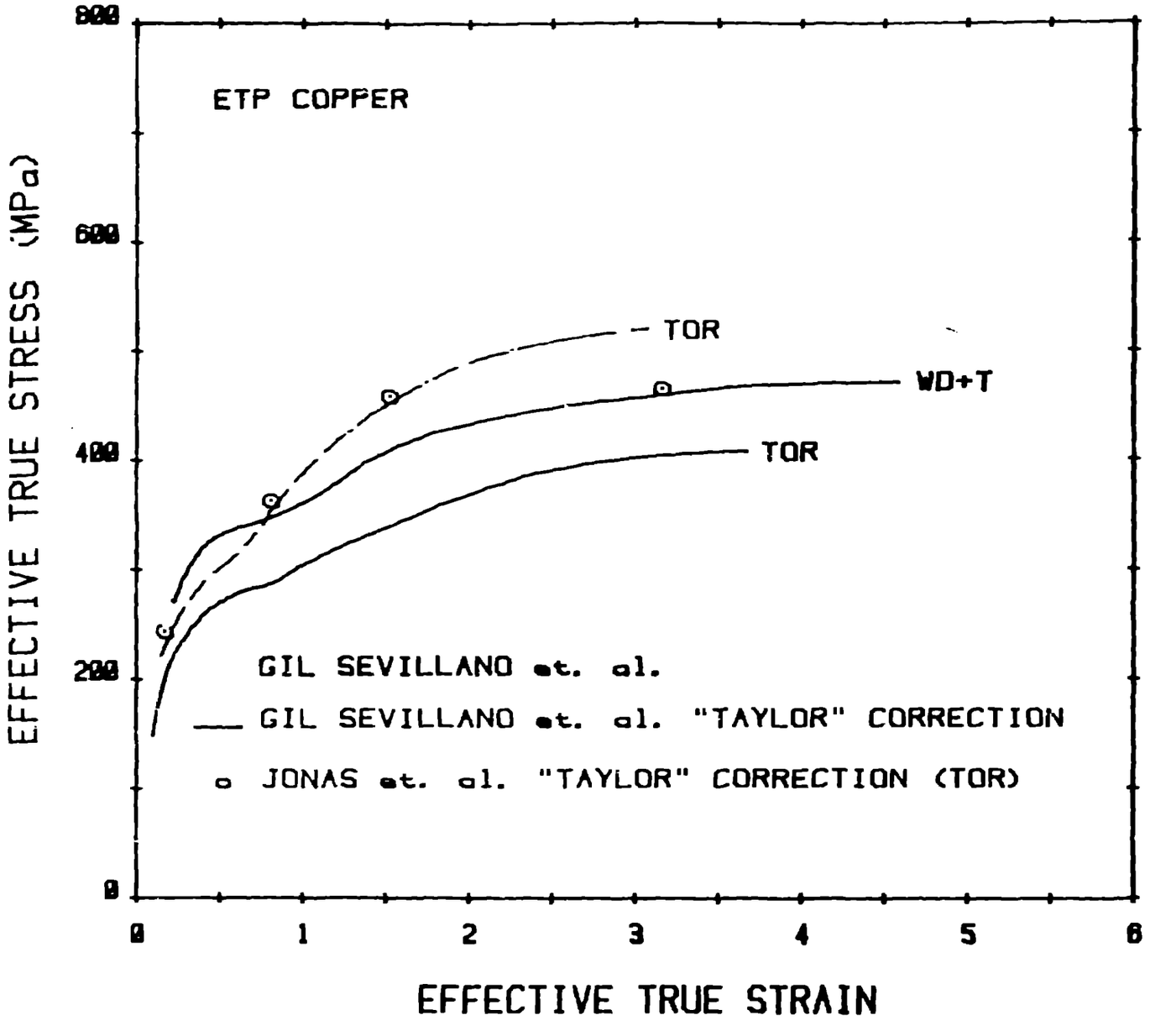
ETP COPPER
EFFECTIVE TRUE STRESS (MPa)
800
600
400
200
0
TOR
WD+T
TOR
GIL SEVILLANO et. al.
GIL SEVILLANO et. al. "TAYLOR" CORRECTION
JONAS et. al. "TAYLOR" CORRECTION (TOR)
0
1
2
3
4
5
6
EFFECTIVE TRUE STRAIN

Figure 18a

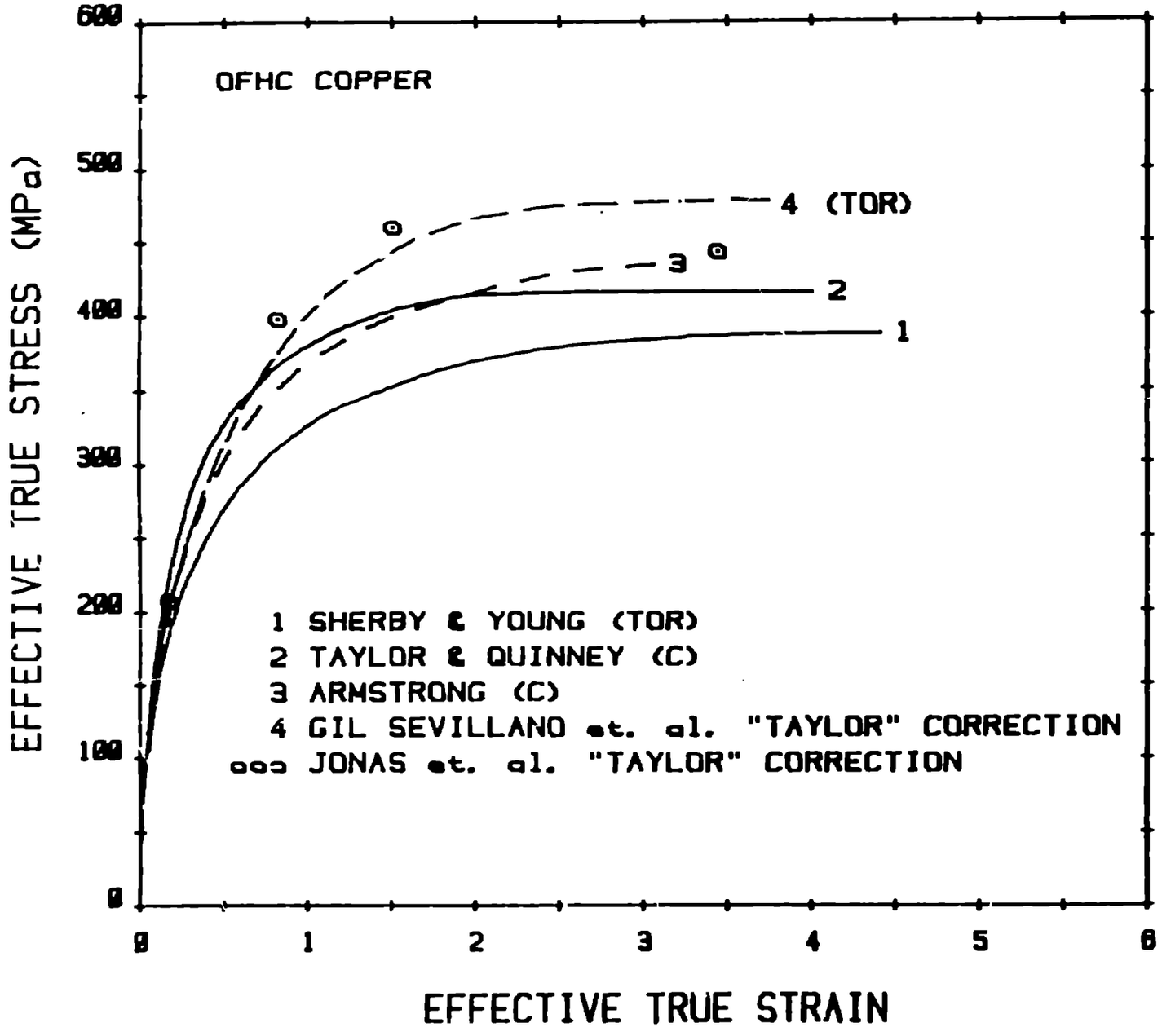
OFHC COPPER
EFFECTIVE TRUE STRESS (MPa)
EFFECTIVE TRUE STRAIN
600
500
400
300
200
100
0
0
1
2
3
4
5
6
4 (TOR)
3
2
1
1 SHERBY & YOUNG (TOR)
2 TAYLOR & QUINNEY (C)
3 ARMSTRONG (C)
4 GIL SEVILLANO et. al. "TAYLOR" CORRECTION
ooo JONAS et. al. "TAYLOR" CORRECTION

Figure 16b

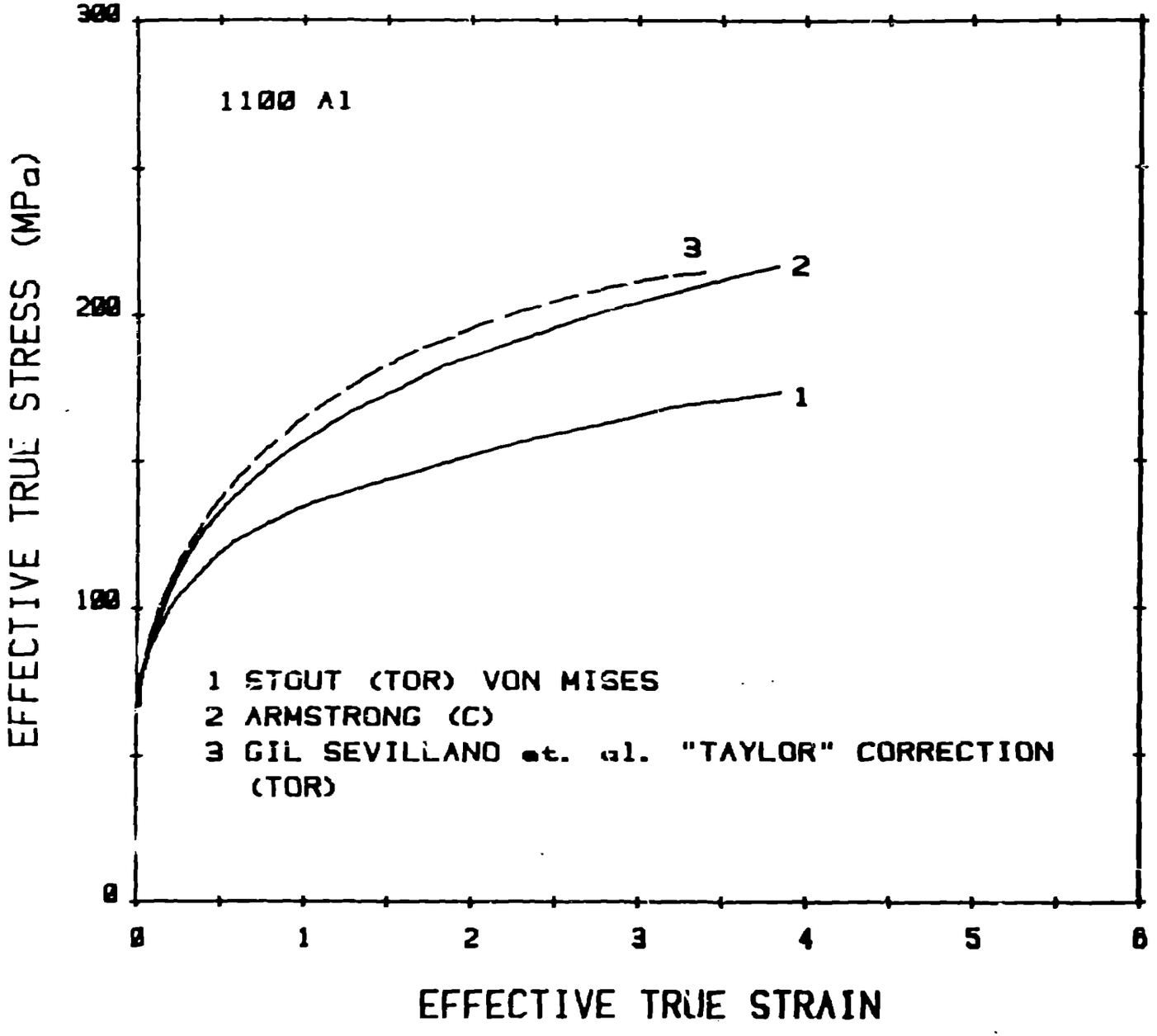
1100 Al
EFFECTIVE TRUE STRESS (MPa)
EFFECTIVE TRUE STRAIN
300
200
100
0
0
1
2
3
4
5
6
3
2
1
1 STOUT (TOR) VON MISES
2 ARMSTRONG (C)
3 GIL SEVILLANO et. al. "TAYLOR" CORRECTION
(TOR)

Figure 19

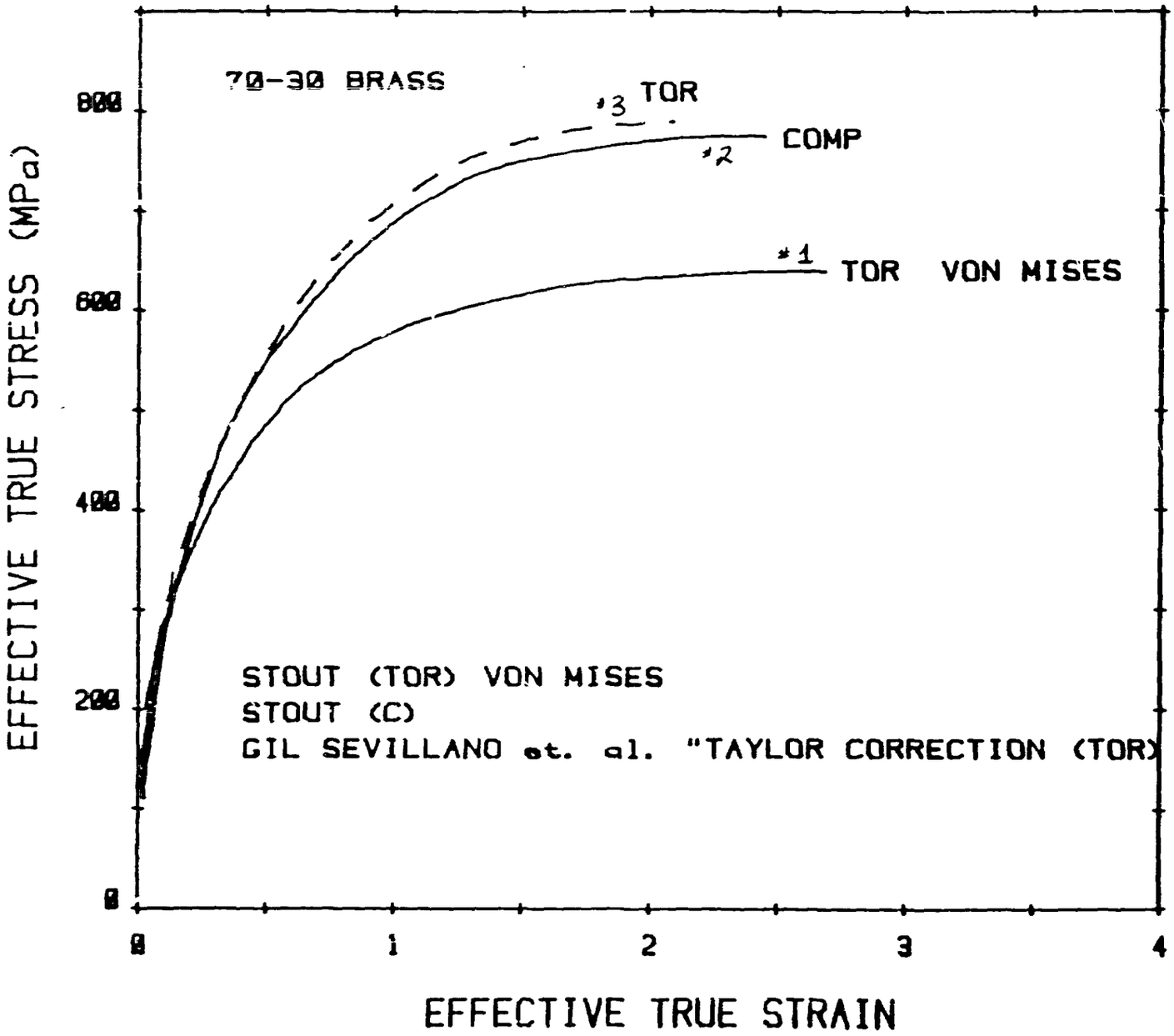
70-30 BRASS
#3 TOR
COMP
#2
#1
TOR VON MISES
STOUT (TOR) VON MISES
STOUT (C)
GIL SEVILLANO et. al. "TAYLOR CORRECTION (TOR)
EFFECTIVE TRUE STRESS (MPa)
800
600
400
200
0
0
1
2
3
4
EFFECTIVE TRUE STRAIN

Figure 20

Intensities and ideal orientations to be added

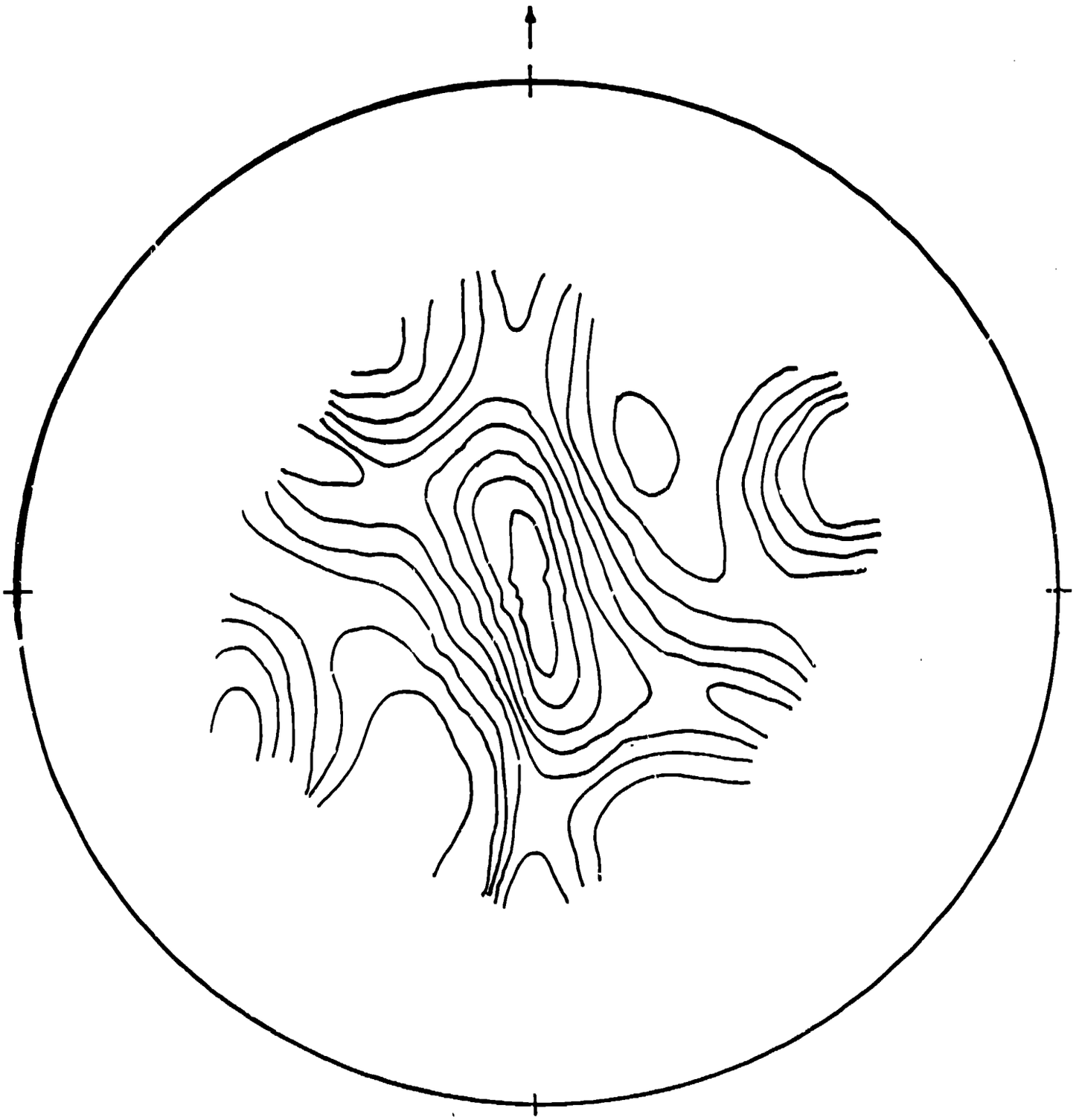

(111) POLE FIGURE
70-30 BRASS (γ = 2.4)

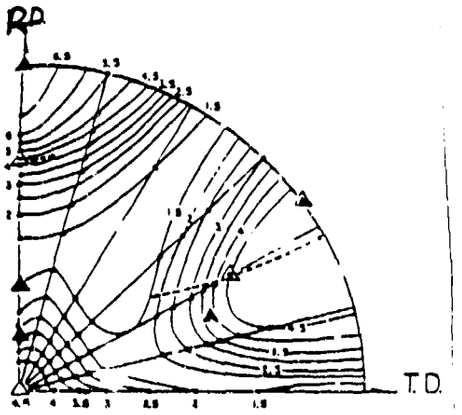

Figure 21b

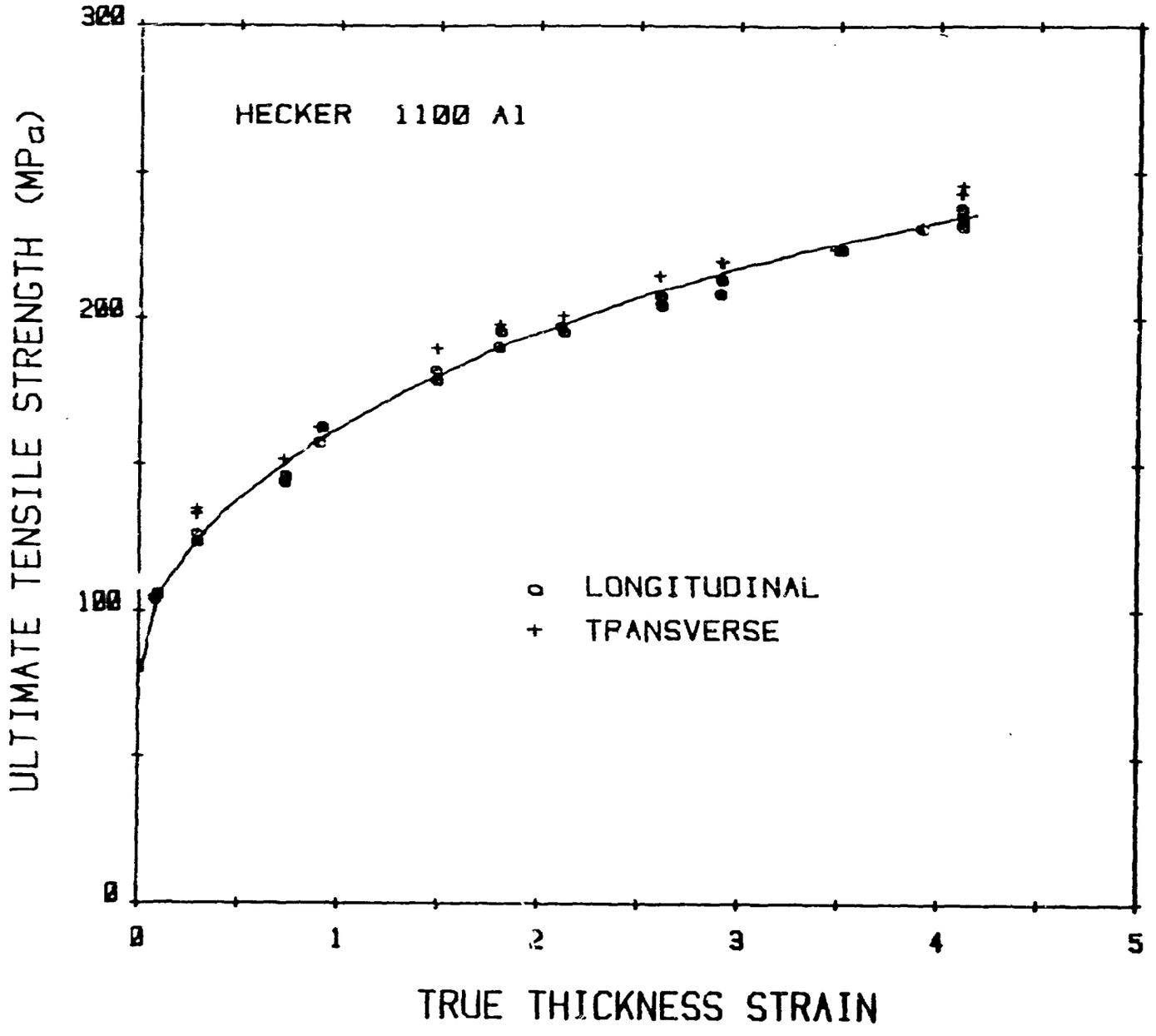
HECKER 1100 Al
ULTIMATE TENSILE STRENGTH (MPa)
300
200
100
0
0
1
2
3
4
5
TRUE THICKNESS STRAIN
o LONGITUDINAL
+ TRANSVERSE

Figure 12

orientations to be added

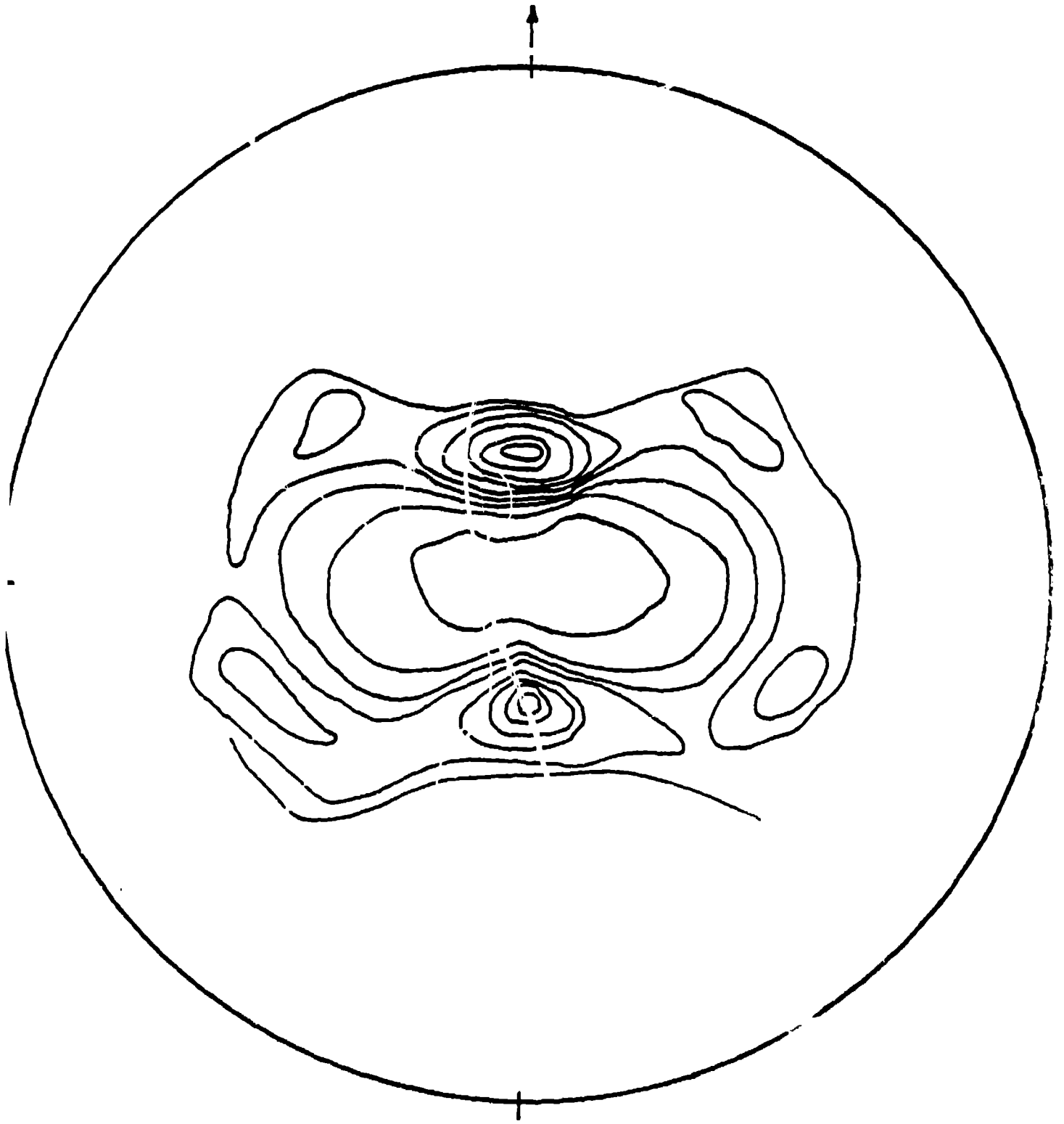

(111) POLE FIGURE
1100 AL SHEET ($\epsilon_t = 1.8$)

Figure 23b

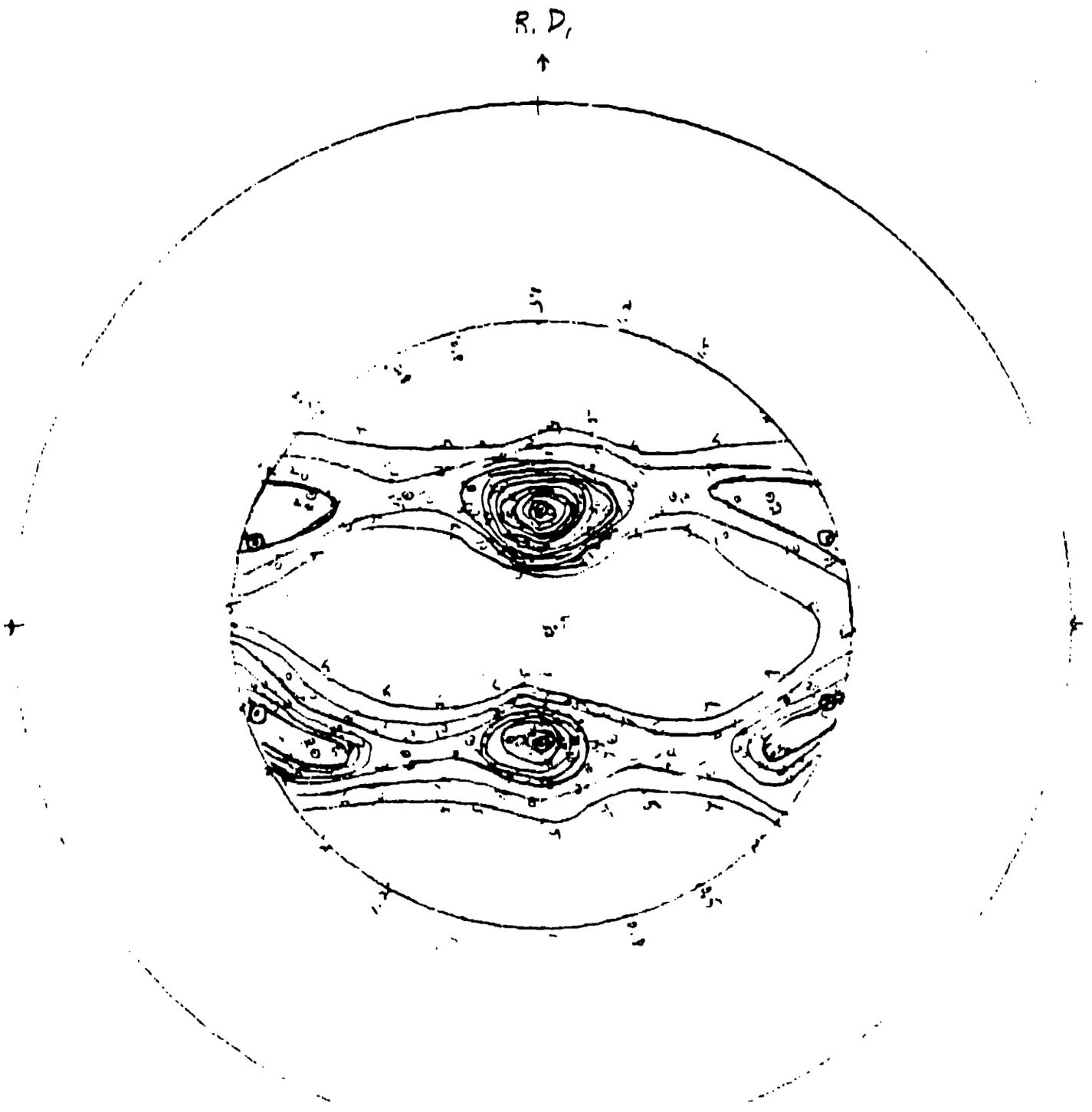

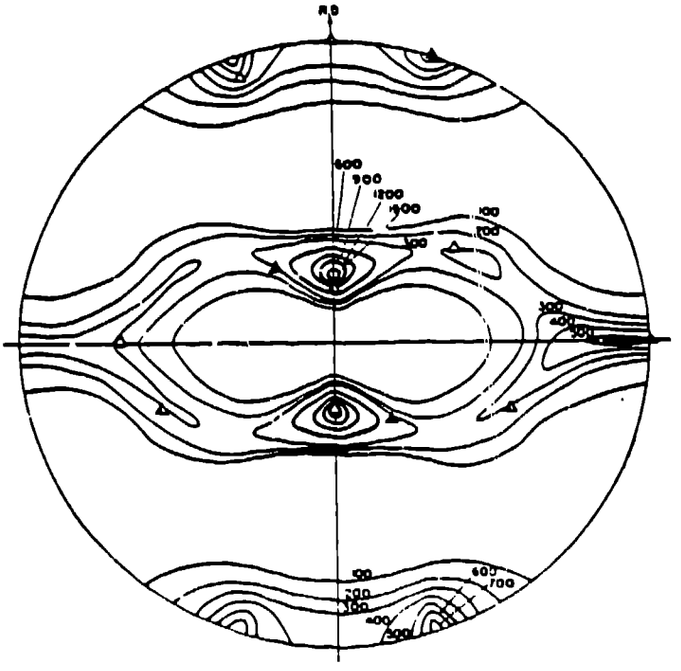
600
900
1200
900
100
100
300
300
400
500
500
600
700
700
100
400
500

Figure 24

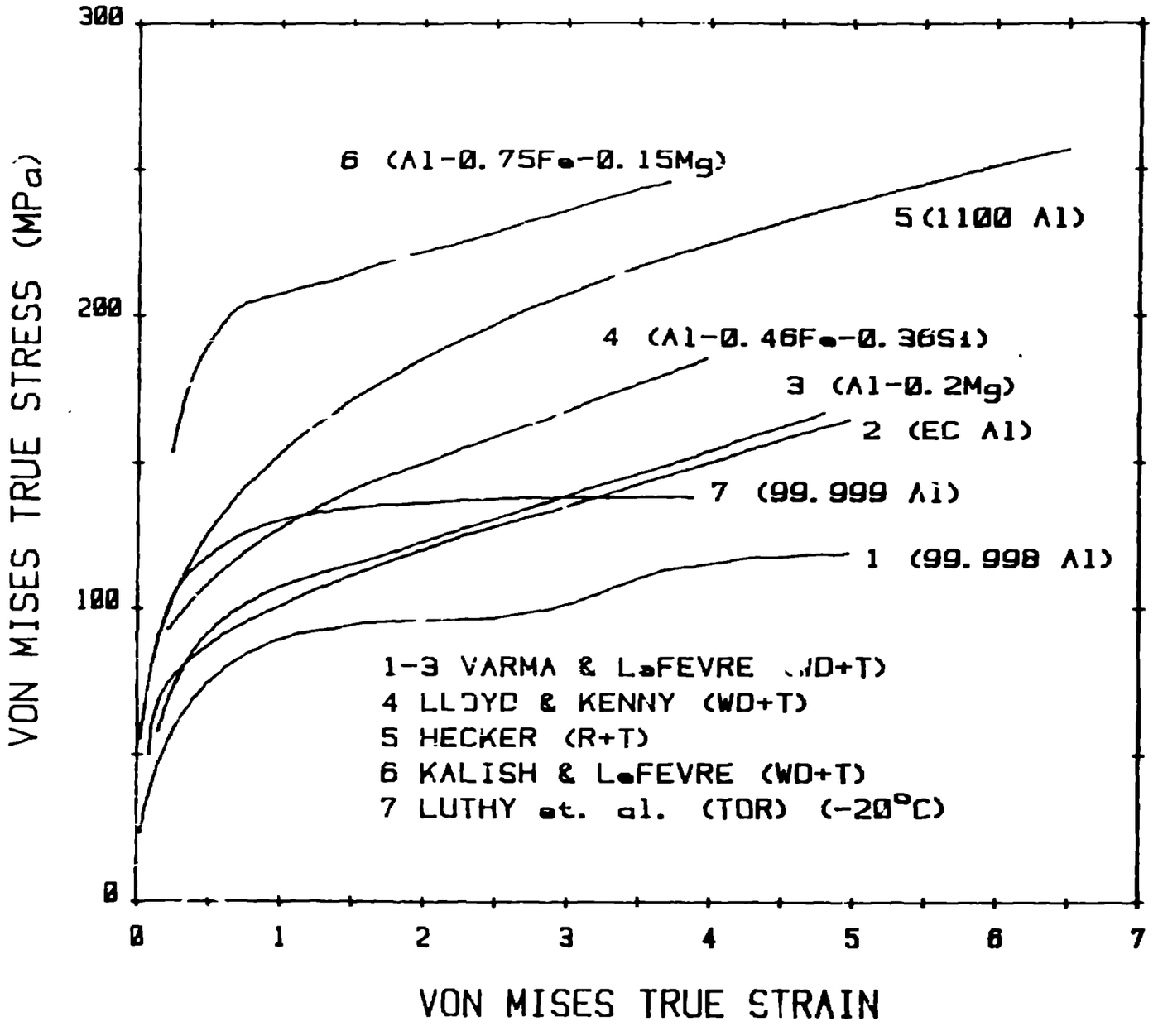
VON MISES TRUE STRESS (MPa)
300
200
100
0
0
1
2
3
4
5
6
7
VON MISES TRUE STRAIN
6 (Al-0.75Fe-0.15Mg)
5 (1100 Al)
4 (Al-0.46Fe-0.36Si)
3 (Al-0.2Mg)
2 (EC Al)
7 (99.999 Al)
1 (99.998 Al)
1-3 VARMA & LeFEVRE (WD+T)
4 LLOYD & KENNY (WD+T)
5 HECKER (R+T)
6 KALISH & LeFEVRE (WD+T)
7 LUTHY et. al. (TOR) (-20°C)

Figure 43

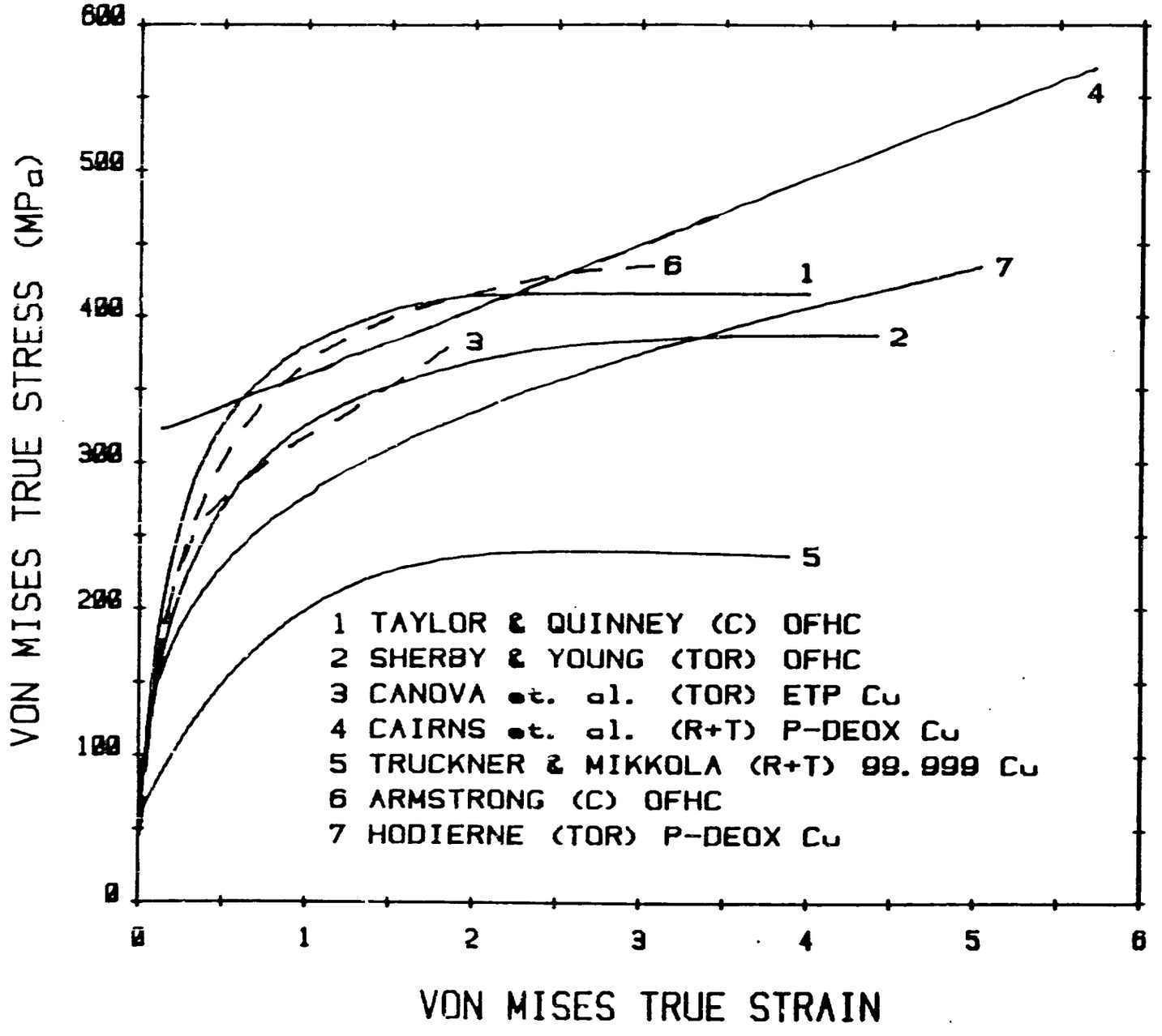
VON MISES TRUE STRESS (MPa)
600
500
400
300
200
100
0
0
1
2
3
4
5
6
VON MISES TRUE STRAIN
1 TAYLOR & QUINNEY (C) OFHC
2 SHERBY & YOUNG (TOR) OFHC
3 CANOVA et. al. (TOR) ETP Cu
4 CAIRNS et. al. (R+T) P-DEOX Cu
5 TRUCKNER & MIKKOLA (R+T) 99.999 Cu
6 ARMSTRONG (C) OFHC
7 HODIERNE (TOR) P-DEOX Cu

Figure 21

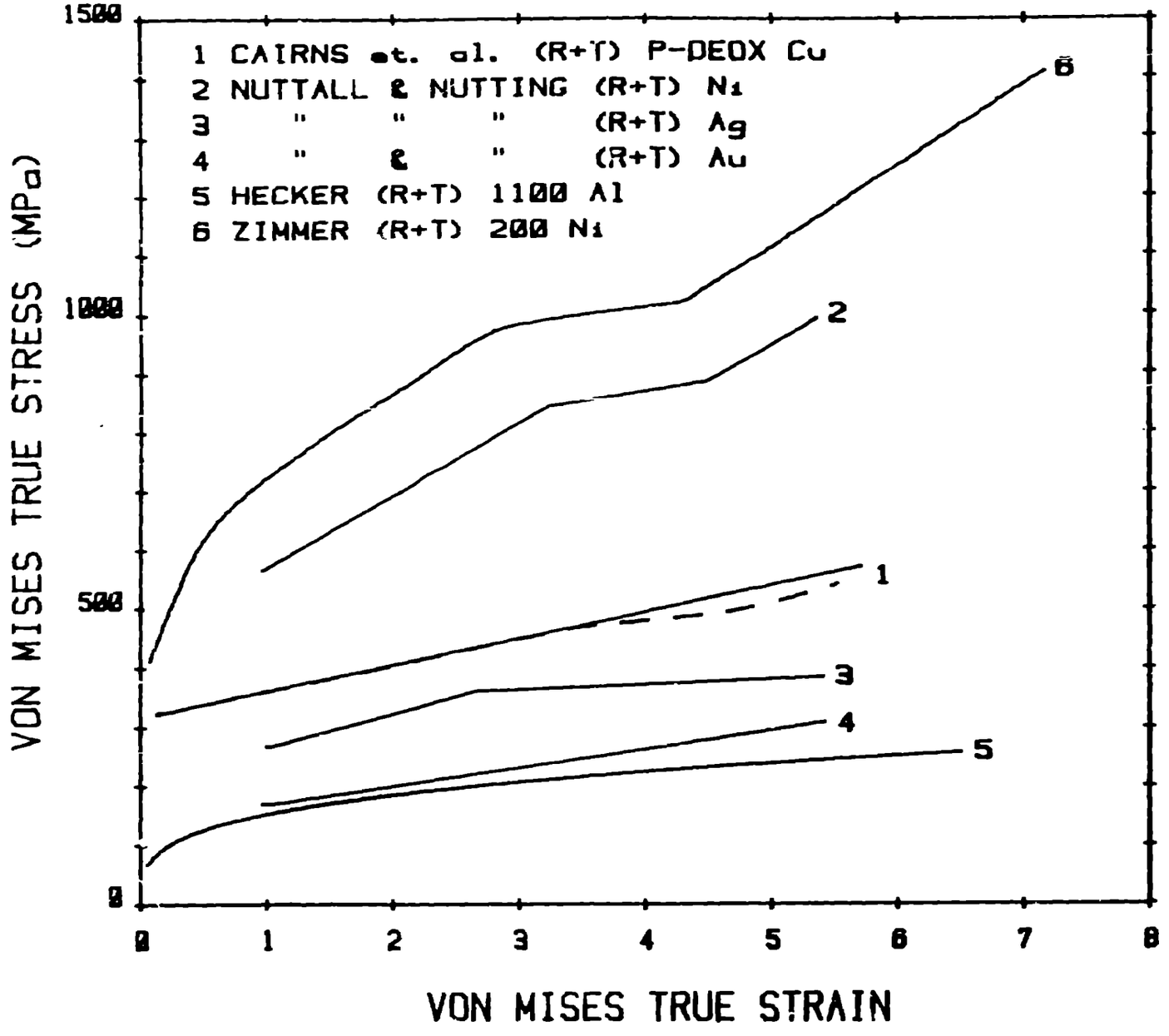
1 CAIRNS et. al. (R+T) P-DEOX Cu
2 NUTTALL & NUTTING (R+T) Ni
3 " " " (R+T) Ag
4 " & " (R+T) Au
5 HECKER (R+T) 1100 Al
6 ZIMMER (R+T) 200 Ni
1500
1000
500
0
0
1
2
3
4
5
6
7
8
VON MISES TRUE STRESS (MPa)
VON MISES TRUE STRAIN

Figure 27

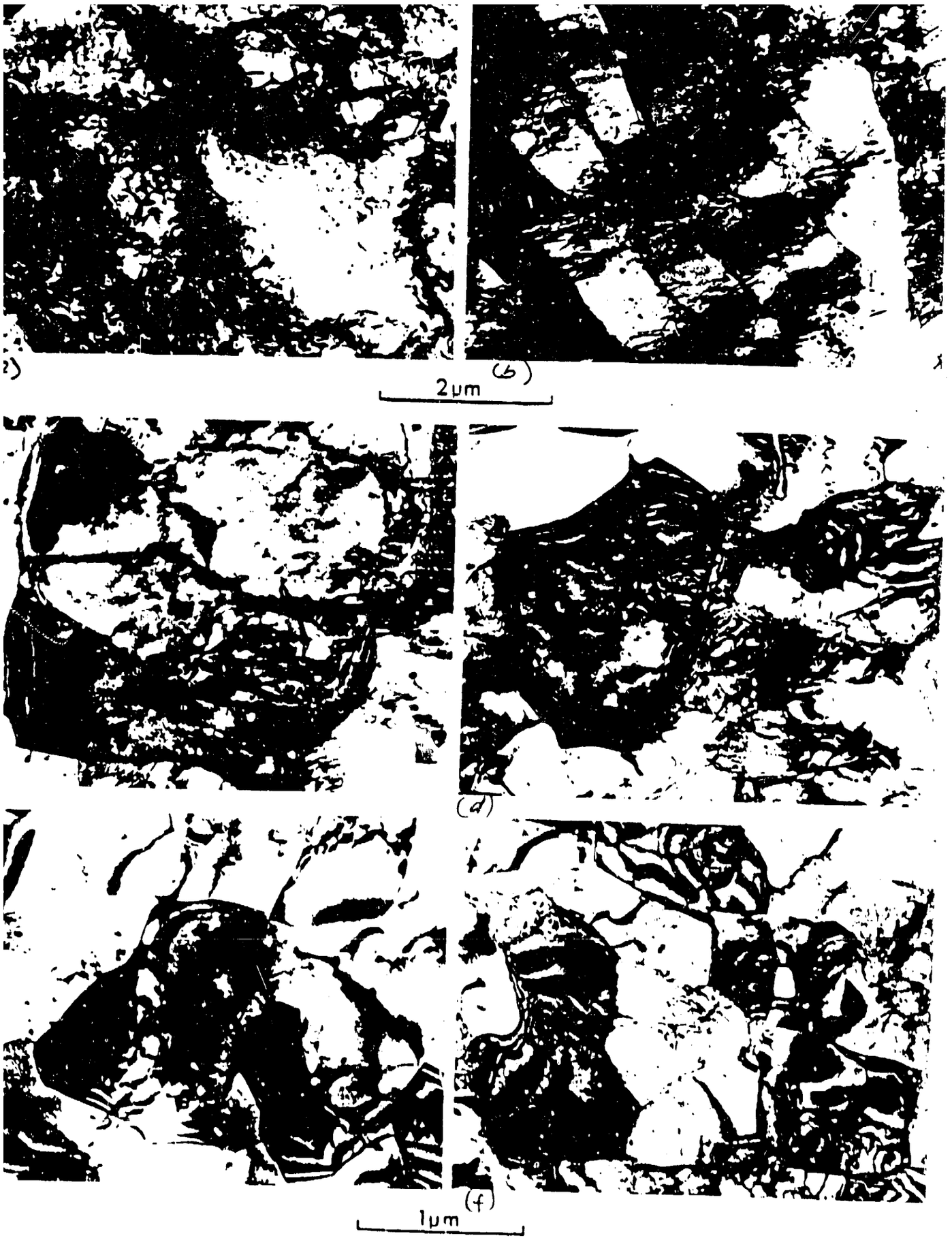

Figure 28

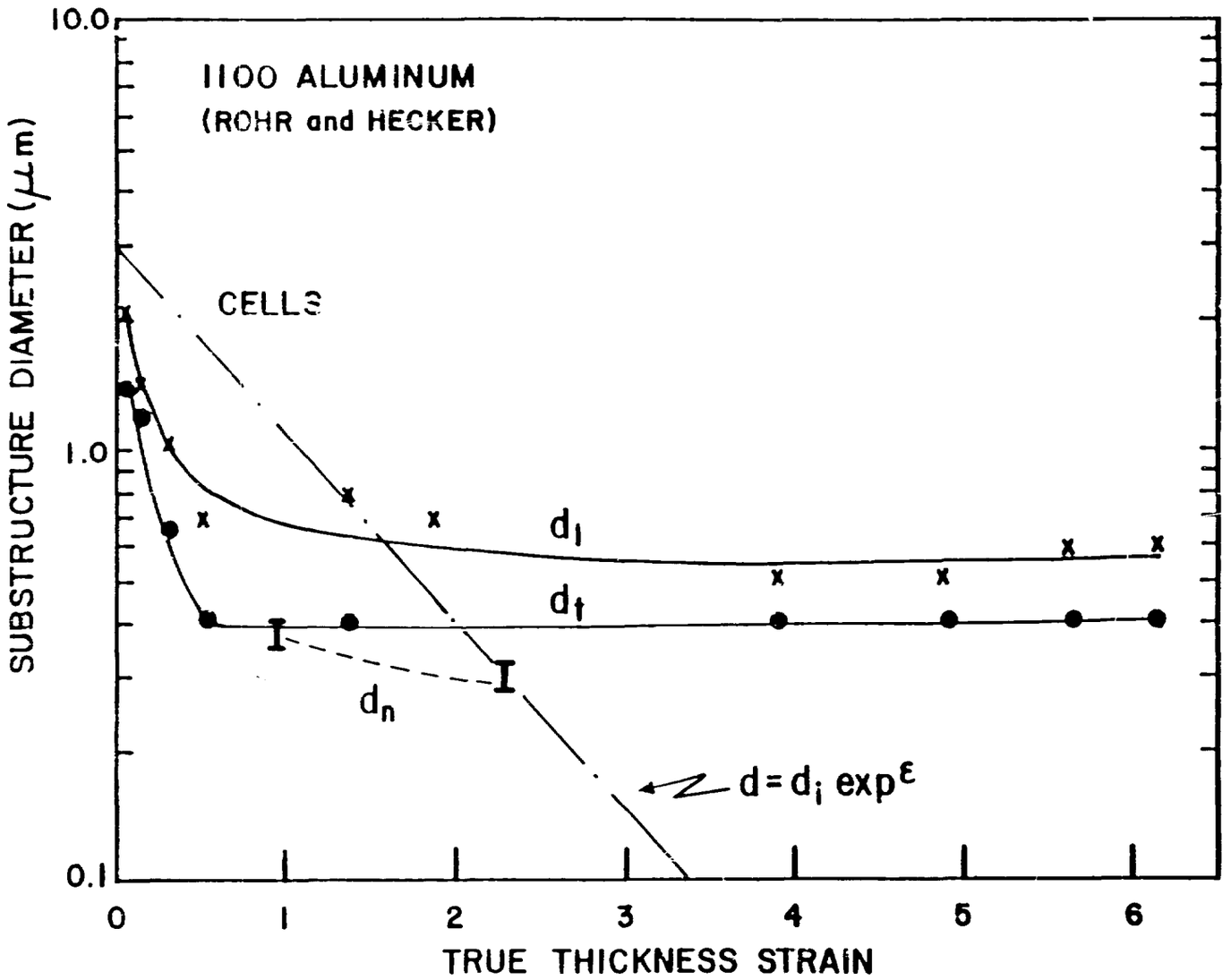
1100 ALUMINUM
(ROHR and HECKER)
CELLS
d_l
d_t
d_n
$d = d_i \exp \varepsilon$
SUBSTRUCTURE DIAMETER (μm)
10.0
1.0
0.1
0
1
2
3
4
5
6
TRUE THICKNESS STRAIN

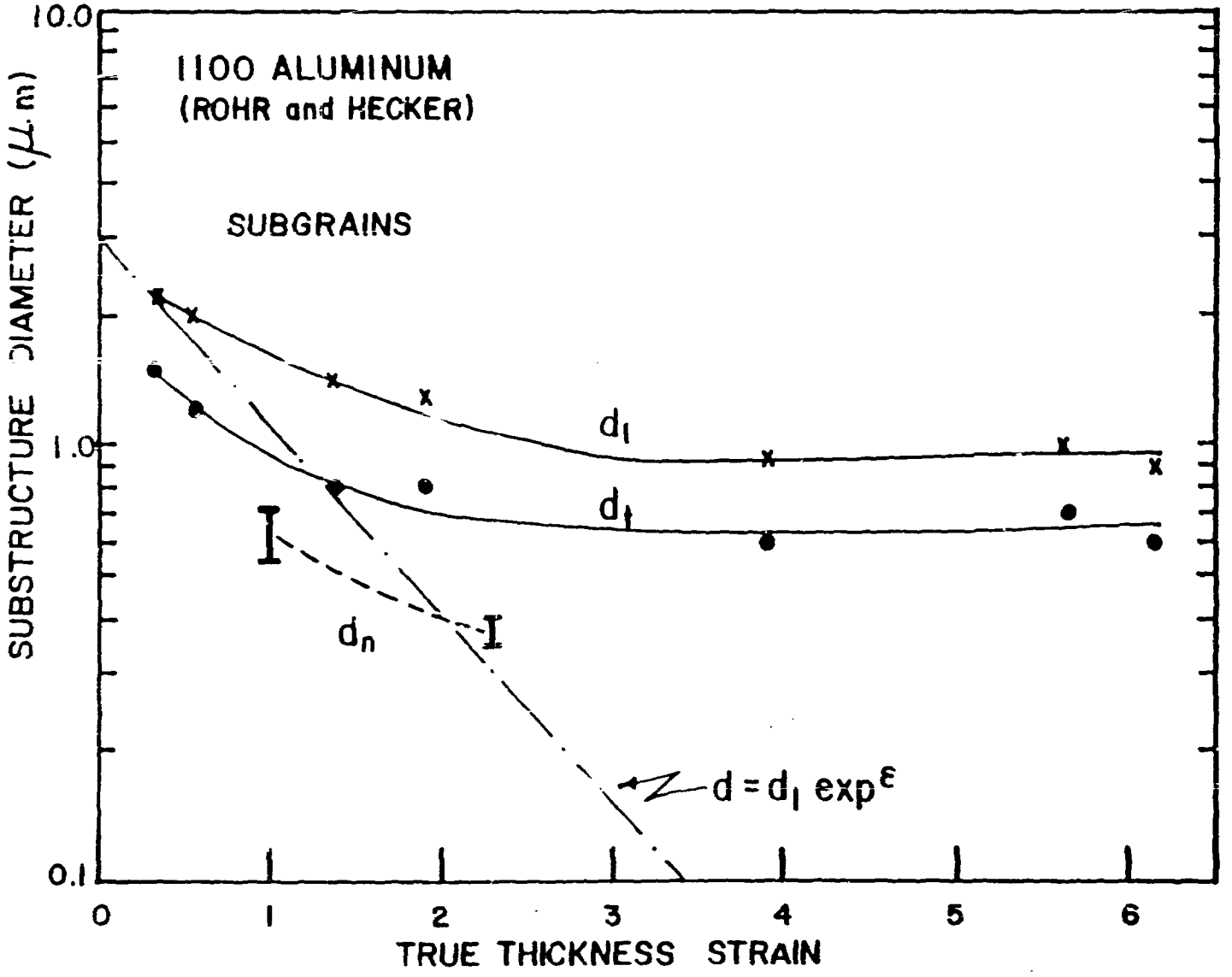
10.0
1.0
0.1
1100 ALUMINUM
(ROHR and HECKER)
SUBGRAINS
SUBSTRUCTURE DIAMETER (μ.m)
d_l
d_l
d_n
$d = d_l \exp^{\varepsilon}$
0
1
2
3
4
5
6
TRUE THICKNESS STRAIN

Figure 29b

Figure 30

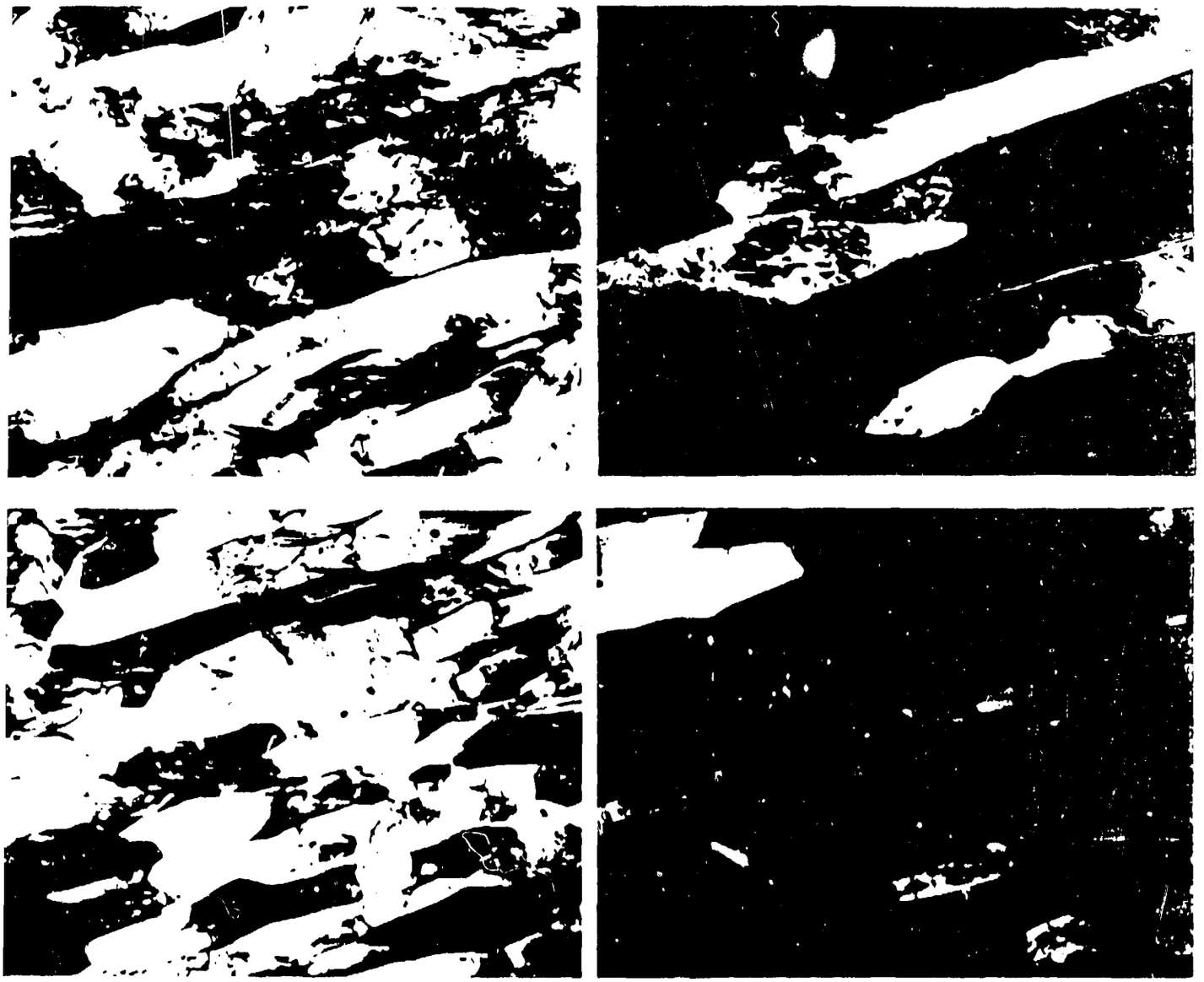

Figure 31

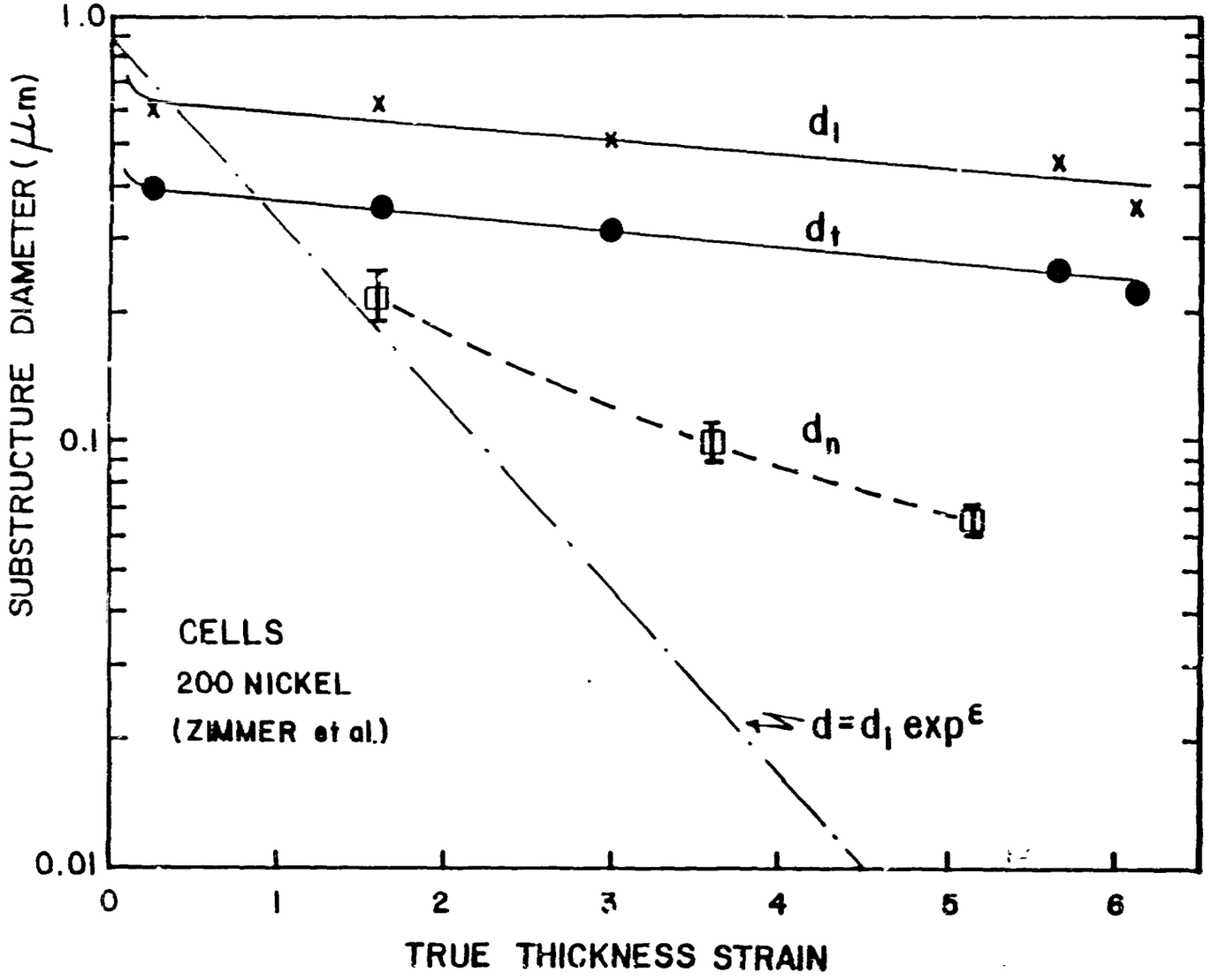
1.0
0.1
0.01
SUBSTRUCTURE DIAMETER (μm)
0
1
2
3
4
5
6
TRUE THICKNESS STRAIN
d_l
d_t
d_n
$d = d_l \exp^{\epsilon}$
CELLS
200 NICKEL
(ZIMMER et al.)

Figure 32a

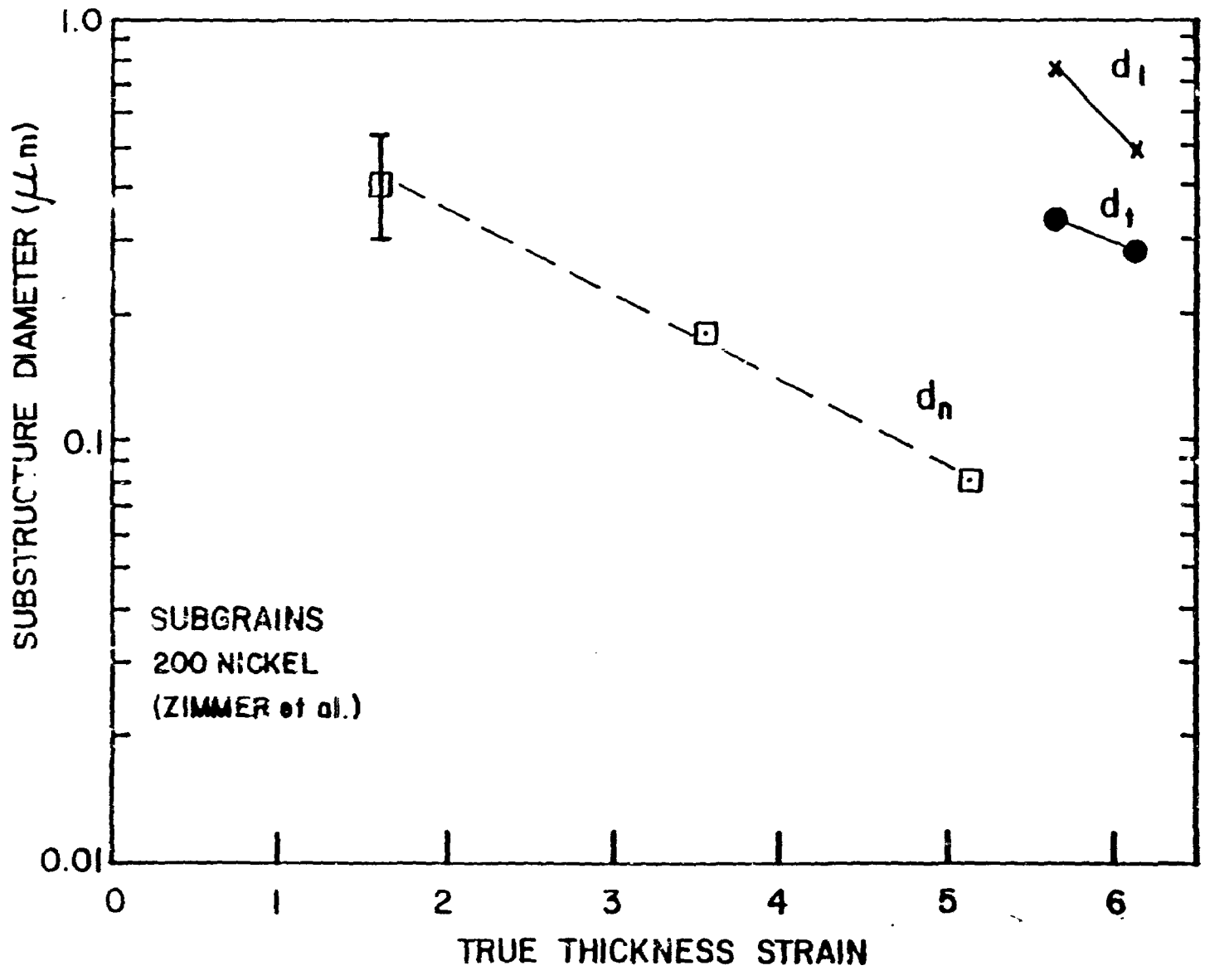
1.0
0.1
0.01
SUBSTRUCTURE DIAMETER (μm)
SUBGRAINS
200 NICKEL
(ZIMMER et al.)
d_n
d_t
d_l
0
1
2
3
4
5
6
TRUE THICKNESS STRAIN

Figure 32b

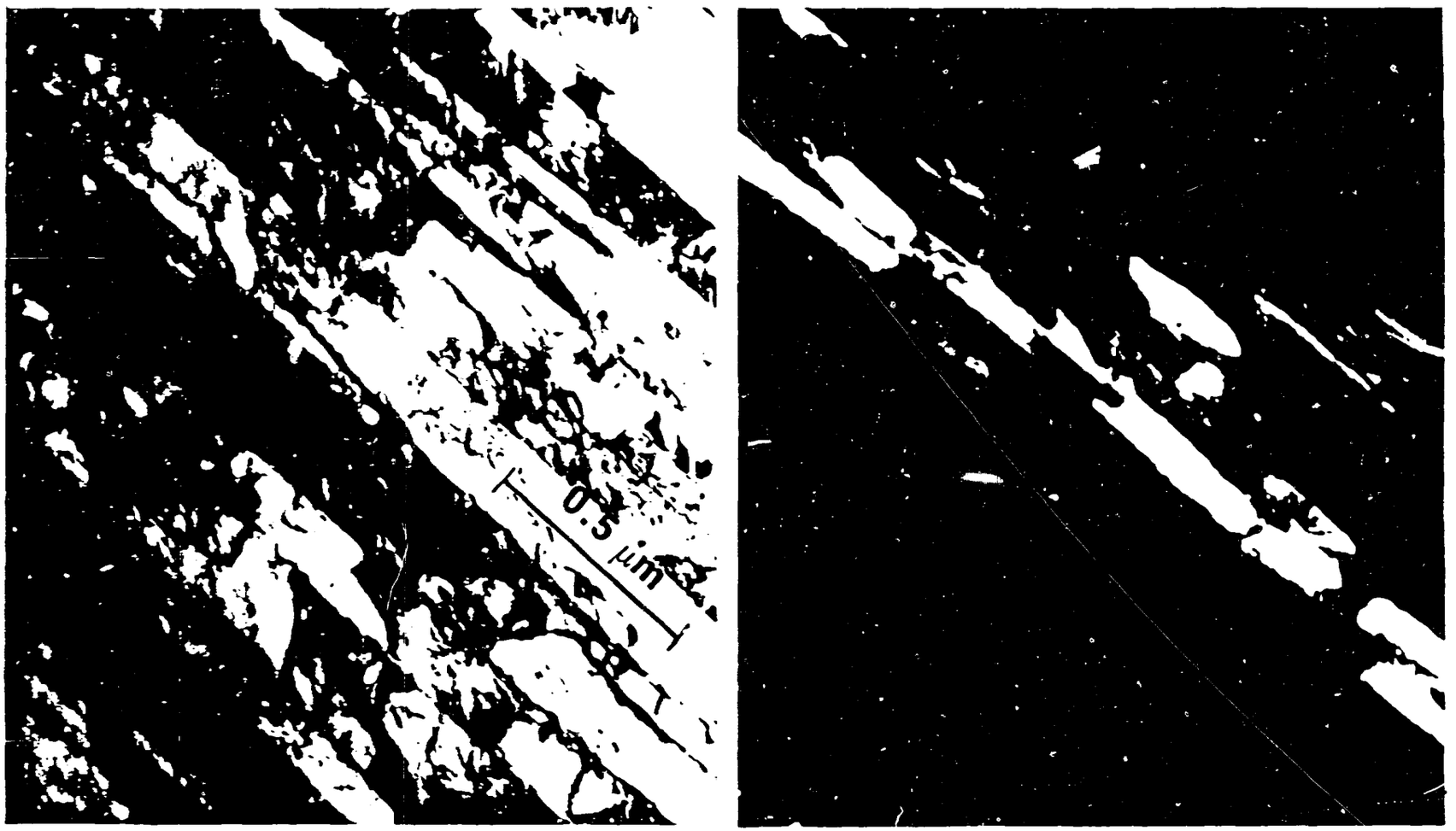

200 NICKEL $\varepsilon_t = 5.14$

Figure 33

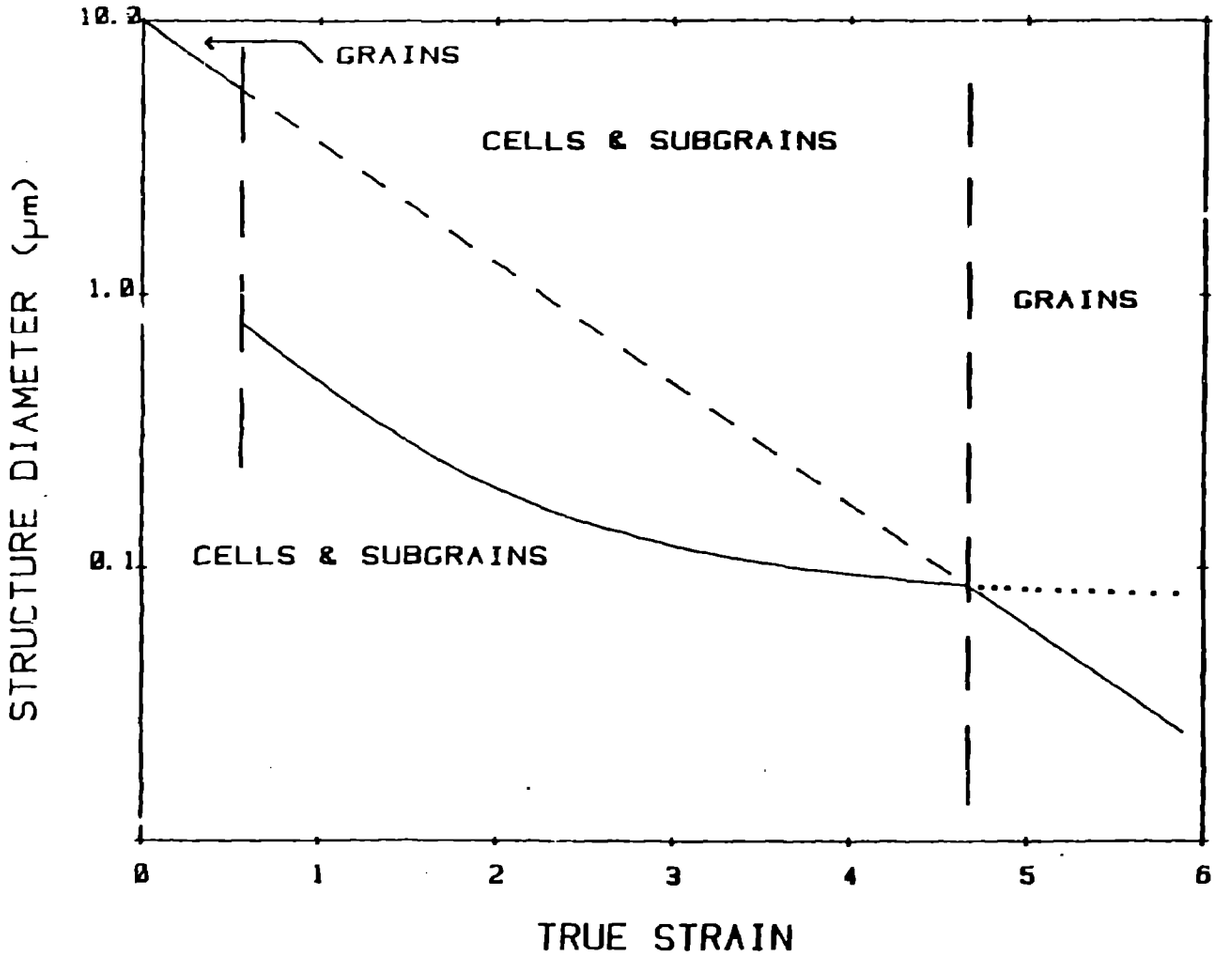
10.0
1.0
0.1
STRUCTURE DIAMETER (μm)
GRAINS
CELLS & SUBGRAINS
GRAINS
CELLS & SUBGRAINS
0
1
2
3
4
5
6
TRUE STRAIN

Figure 34

Figure 35

a)

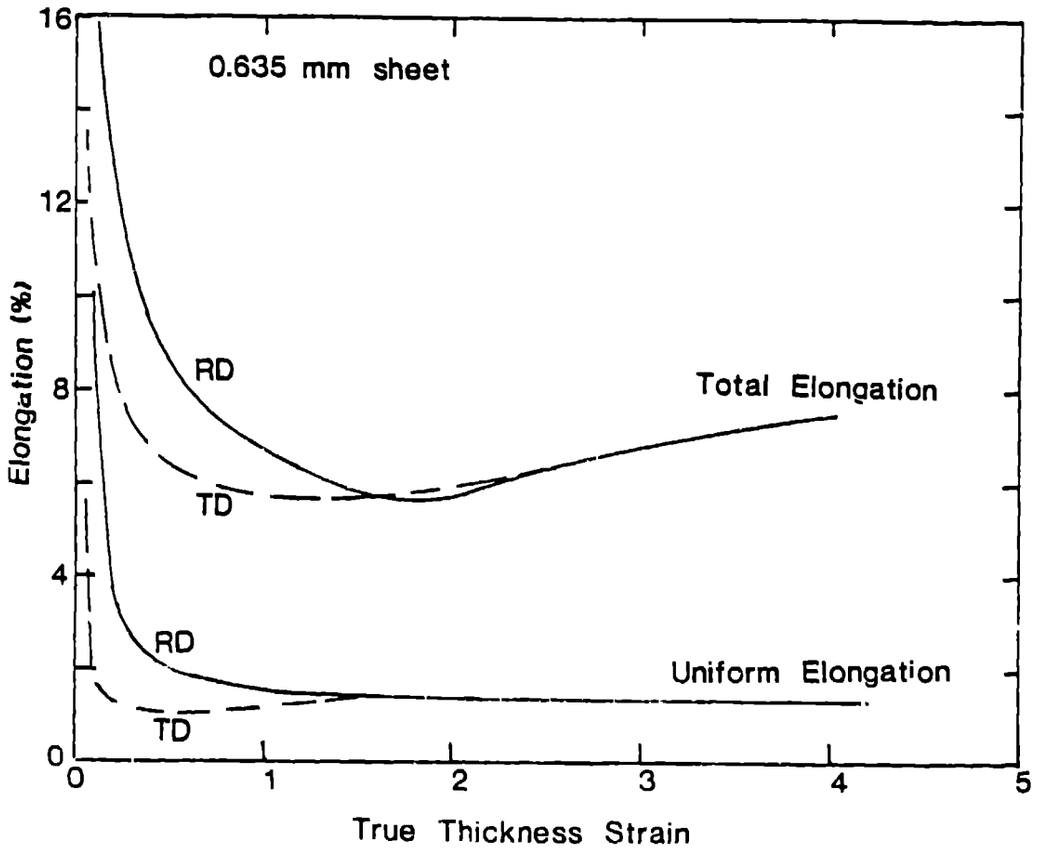
0.635 mm sheet
Elongation (%)
16
12
8
4
0
RD
TD
RD
TD
Total Elongation
Uniform Elongation
0
1
2
3
4
5
True Thickness Strain

b)

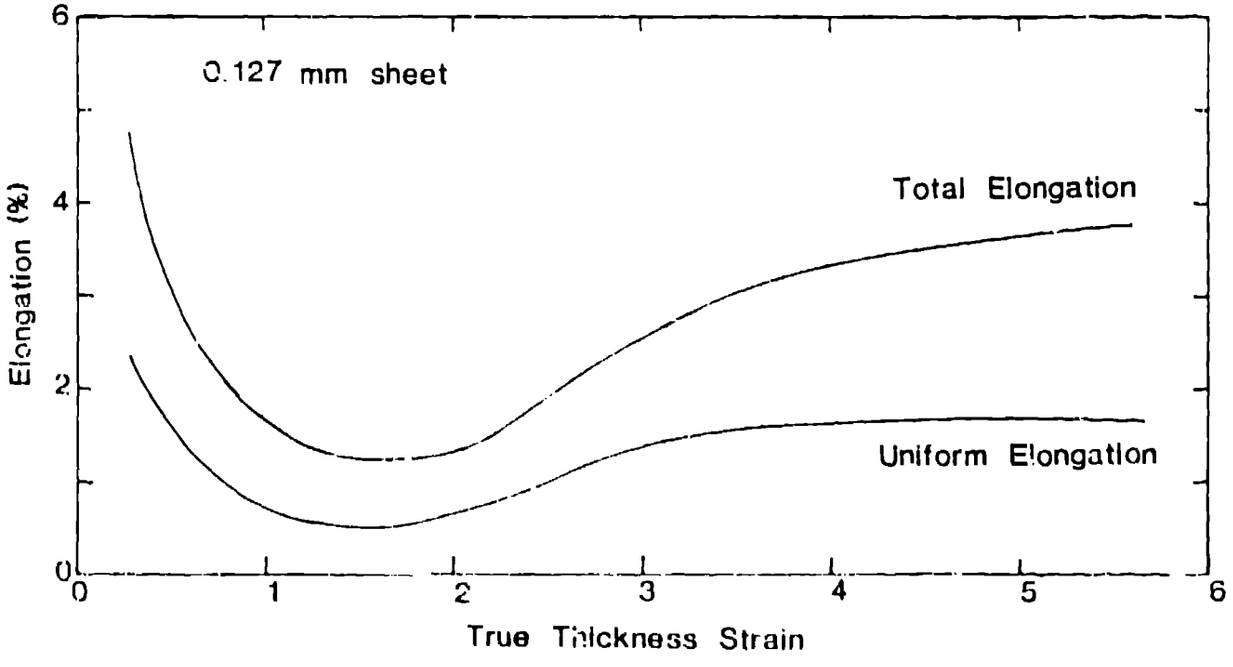
0.127 mm sheet
Elongation (%)
6
4
2
0
Total Elongation
Uniform Elongation
0
1
2
3
4
5
6
True Thickness Strain

Figure 36

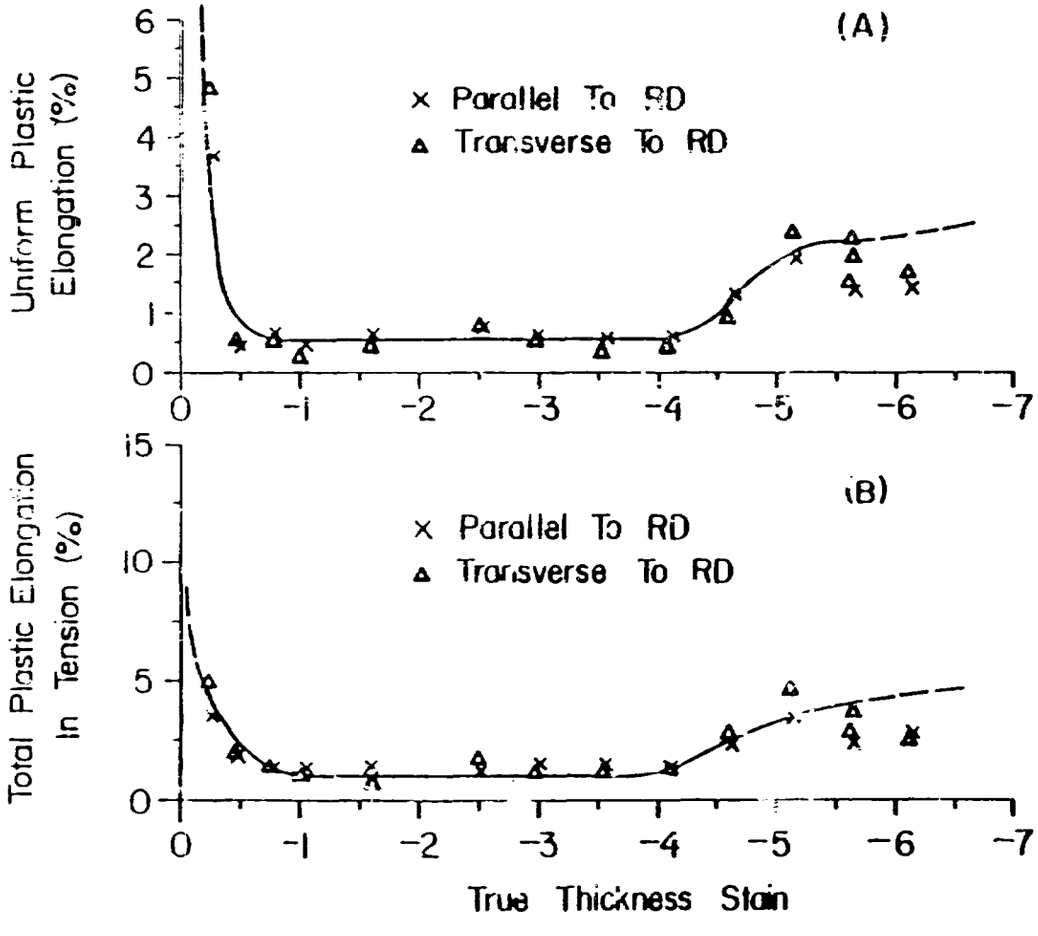
(A)
× Parallel To RD
△ Transverse To RD
Uniform Plastic Elongation (%)
6
5
4
3
2
1
0
0
-1
-2
-3
-4
-5
-6
-7
(B)
× Parallel To RD
△ Transverse To RD
Total Plastic Elongation In Tension (%)
15
10
5
0
True Thickness Stain

Figure 37

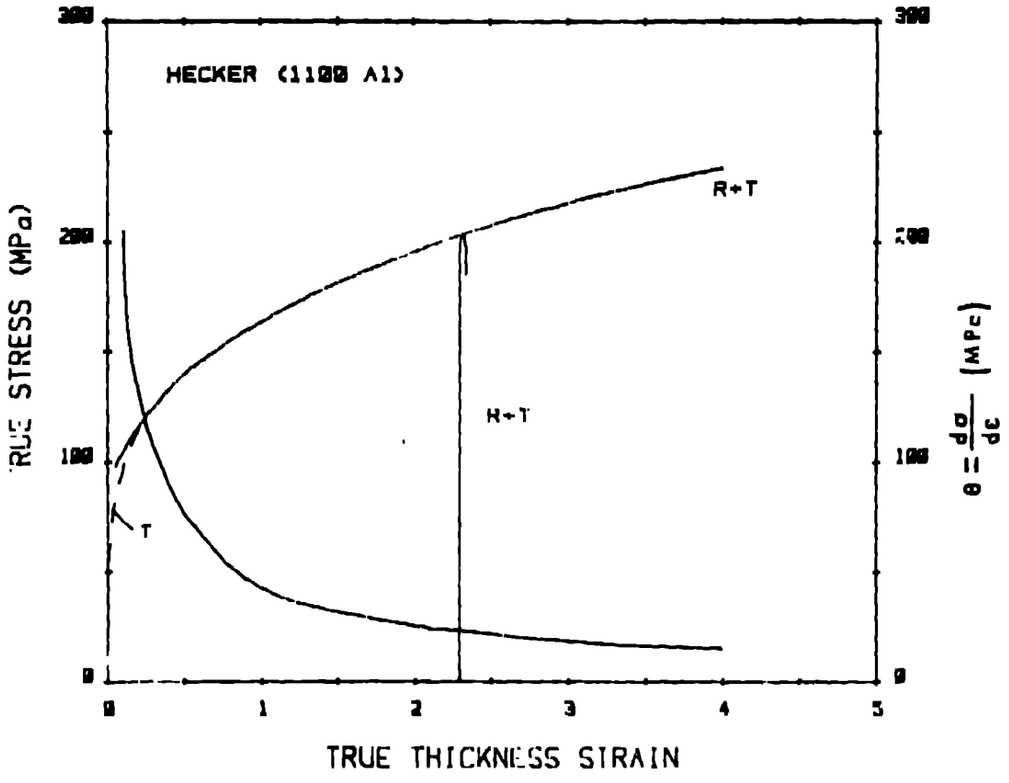
HECKER (1100 A1)
R+T
R+T
T
TRUE STRESS (MPa)
TRUE THICKNESS STRAIN
θ = dσ/dε (MPa)
0
1
2
3
4
5

Figure 38

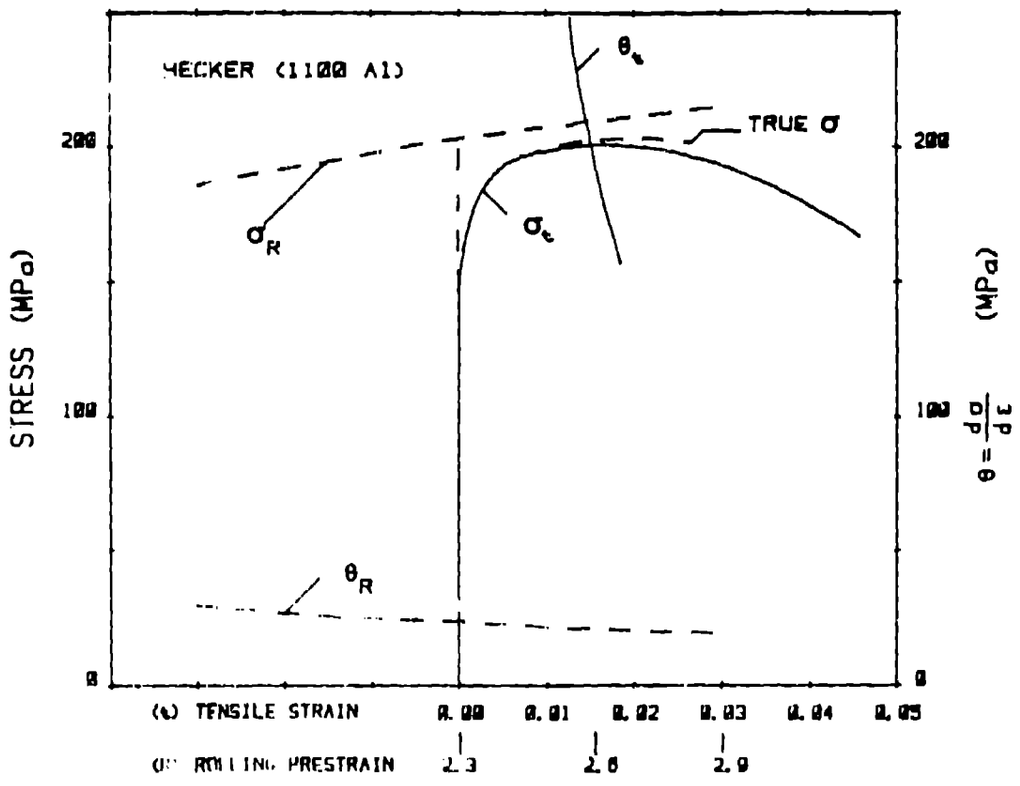
HECKER (1100 A1)
TRUE σ
θ_t
σ_R
σ_t
θ_R
STRESS (MPa)
$\theta = \frac{\partial \sigma}{\partial \varepsilon_p}$ (MPa)
200
100
0
(ε) TENSILE STRAIN
0.00
0.01
0.02
0.03
0.04
0.05
(%) ROLLING PRESTRAIN
2.3
2.6
2.9

Figure 39

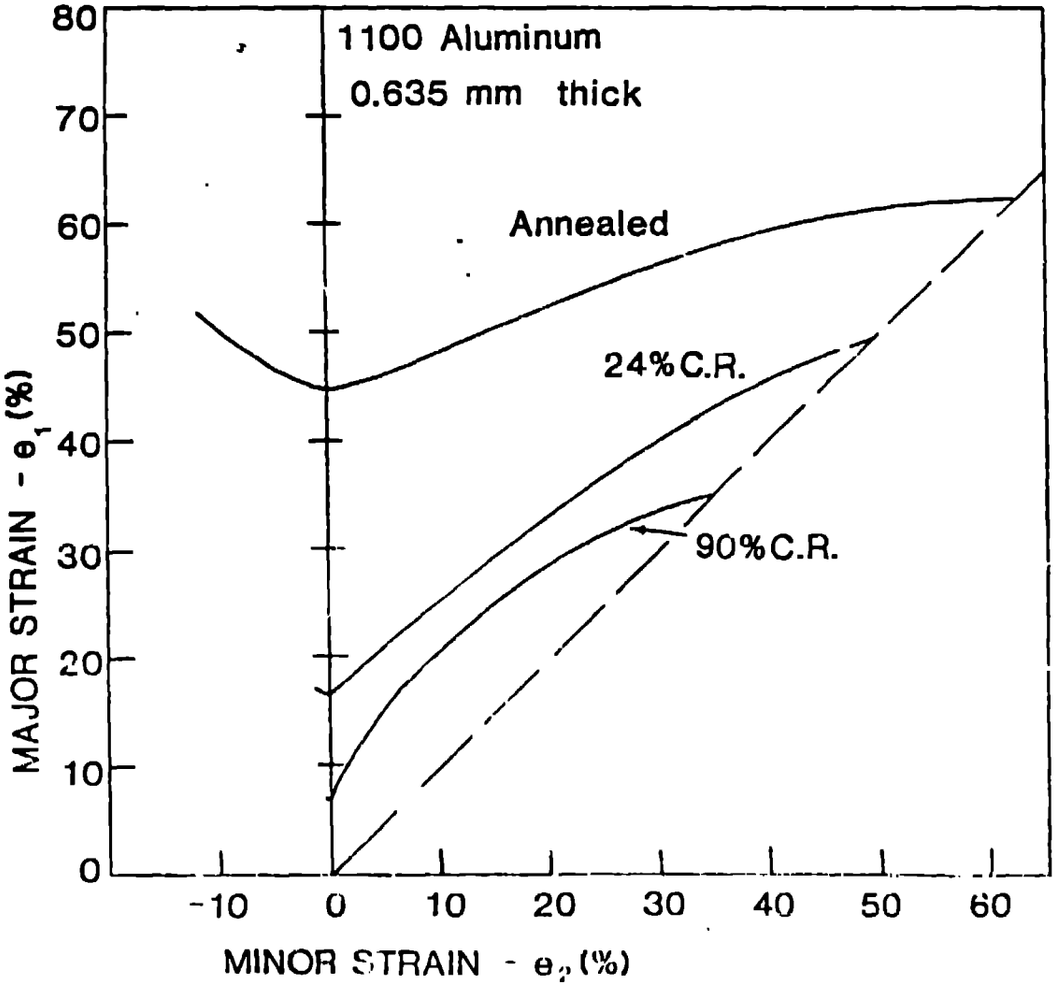
1100 Aluminum
0.635 mm thick
Annealed
24%C.R.
90%C.R.
MAJOR STRAIN - e_1 (%)
MINOR STRAIN - e_2 (%)
80
70
60
50
40
30
20
10
0
-10
0
10
20
30
40
50
60

Figure 40

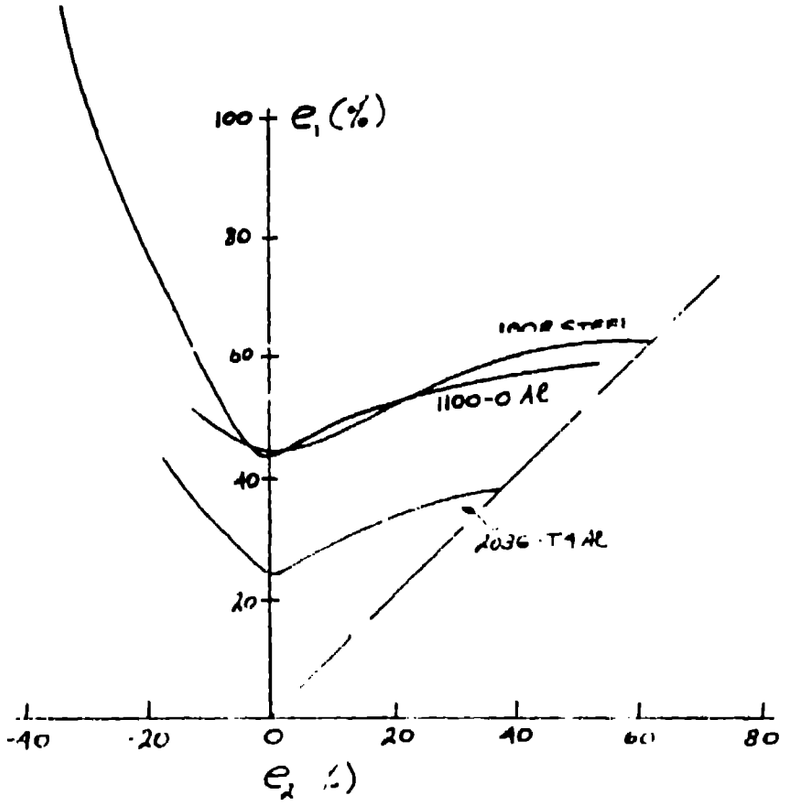

Figure 41

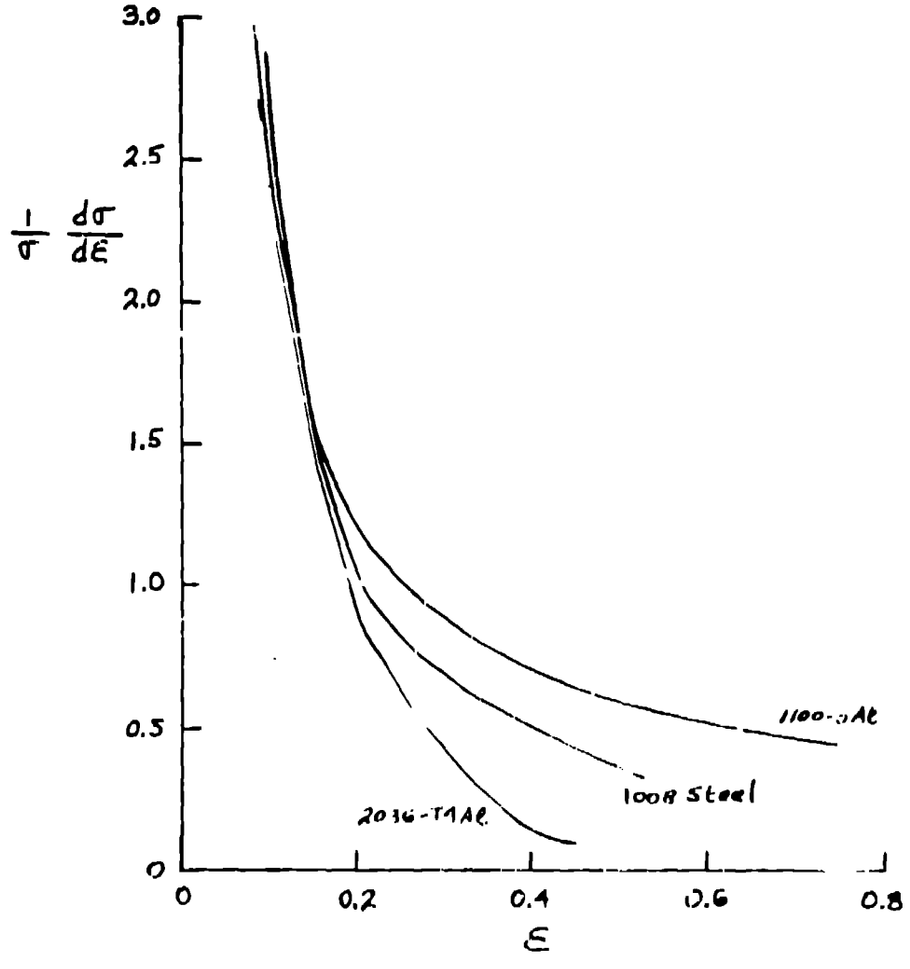
3.0
2.5
2.0
1.5
1.0
0.5
0
$\frac{1}{\sigma}\frac{d\sigma}{d\varepsilon}$
0
0.2
0.4
0.6
0.8
ε
1100-0Al
1008 Steel
2036-T4Al

Figure 42